



National  
Defence

Défense  
nationale



# **DETECTION AND TRACKING OF LOW-ALTITUDE AIRCRAFT USING HF SURFACE-WAVE RADAR**

by

**Hing C. Chan**

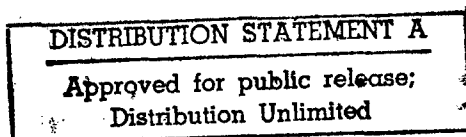
19990126 131

**DEFENCE RESEARCH ESTABLISHMENT OTTAWA**  
REPORT NO. 1334

**THIS QUALITY INSURED**

**Canada**

December 1998  
Ottawa



AQF99-04-0733



National    Défense  
Defence    nationale

# **DETECTION AND TRACKING OF LOW-ALTITUDE AIRCRAFT USING HF SURFACE-WAVE RADAR**

by

**Hing C. Chan**  
*Ground Based Radar Group*  
*Surface Radar Section*

**DEFENCE RESEARCH ESTABLISHMENT OTTAWA**  
REPORT NO. 1334

PROJECT  
05AB11

December 1998  
Ottawa

## ABSTRACT

A series of aircraft-detection trials was conducted using experimental high frequency surface wave radar (HFSWR) facilities located on the east coast of Canada. These trials were part of a research and development project undertaken at DND to demonstrate the HFSWR technology in a wide-area coastal surveillance role. Several aircraft were used in these trials, including a Beechcraft King-Air 200, a Lockheed T-33 and a Canadair Challenger 601 aircraft. Experimental results were in excellent agreement with theoretical predictions. With relatively low averaged power, the King-Air and the Challenger were tracked to beyond 120 km. The ability of the HFSWR to track manoeuvring targets was demonstrated. In addition the radar is also capable of long-range tracking of high-altitude aircraft. Signal-processing algorithms for the HFSWR can be improved by exploiting the characteristics of the signal environment measured in these trials.

## RÉSUMÉ

Une série d'essais de détection d'avions a été exécutée en utilisant des radar décimétrique à ondes de surface (RDOS) situés sur la côte est du Canada. Ces essais faisaient partie d'un projet de recherche et développement entrepris par le Ministère de la Défense Nationale pour démontrer la technologie RDOS dans un rôle de surveillance côtière à grande surface. Quelques types d'avions ont été utilisés dans ces essais: le King-Air 200 de beechcraft, le Lockheed T-33 et le Canadair Challenger 601. Il y a un très bon accord entre les résultats expérimentaux et la théorie. L'avion King-Air et l'avion Challenger ont été traqués à plus de 120 km en utilisant un radar qui transmet une puissance moyenne relativement faible. Ces résultats démontrent la capacité du RDOS de traquer une cible, qui fait des manœuvres. De plus, le RDOS est capable de traquer les avions à grandes distance et à haute altitude. C'est possible d'améliorer l'algorithme pour le traitement du signal du RDOS en exploitant les caractéristiques des signaux mesurés de l'environnement pendant les essais.

## EXECUTIVE SUMMARY

The Surface Radar Section of the Defence Research Establishment has engaged in research and development in high frequency surface wave radar (HFSWR) technology for the past ten years. One of the objectives has been to demonstrate this technology in a wide-area coastal surveillance role. In the development of the demonstrator radar, a series of aircraft-detection trials was conducted using experimental HFSWR facilities located in the east coast of Newfoundland, Canada. Two HFSWR test beds were used in these trials, one at Cape Bonavista, the other at Cape Race.

The Cape Bonavista facility was first developed and operated by Nordco Limited for DND. The HF radar section of Nordco was subsequently taken over by Raytheon Canada Limited (RCL), and RCL has since been under contract to the DND to carry out experimental trials.

The second HFSWR facility, located at Cape Race, is owned and operated by Northern Radar Systems Limited of St. John's, Newfoundland. This company has operated a HFSWR for the past fifteen years, primarily for experimenting with detection and tracking of surface vessels and the monitoring of ocean surface conditions.

In this report, we seek to answer some of the questions pertaining to the performance of HFSWR in low-altitude aircraft detection. These include detection range, transmit power requirements, the signal processing requirements, and to what degree the experimental performance of the HFSWR matches the theoretical predictions. Answers to these questions would enable the determination of hardware and software requirements for a HFSWR system that can meet a given set of performance specifications.

Several aircraft were used in these trials. These included the Beechcraft King-Air 200, a Lockheed T-33 and a Canadair Challenger 601. In addition targets of opportunity, such as regularly scheduled airliners and military aircraft, were utilized. Results obtained from the Cape Bonavista radar indicated that the experimental performance of the radar was very close to the theoretical prediction and that Cape Bonavista may be classified as a very quiet rural site. With an average power of several tens of watts, an aircraft such as the Beechcraft King-Air 200 can be detected and tracked out to 80 km during daylight hours. Results obtained from the Cape Race radar indicated that the performance of that radar had not matched the theoretical prediction. Because the radar at Cape Race had not been properly calibrated, the origin of the performance deficiency could not be determined precisely. Both system and environmental factors may have contributed to the degraded detection performance.

The ability of the HFSWR to track low-altitude manoeuvring aircraft was demonstrated. A King-Air 200 flying at 200 ft in a figure-eight pattern centred at 40 km was detected and tracked throughout the course. Only a few detections were missed when the target Doppler was too close to the sea-clutter dominated region. The ability of the HFSWR to track high-altitude aircraft at very long range was also demonstrated by detecting and tracking commercial airliners to ranges beyond 275 km.

This report examines the signal environment in which the HFSWRs operate and notes the characteristics of interfering signals. Knowledge gained in the analysis of the interference signals will help in the development of interference suppression algorithms. Effective interference-suppression techniques are crucial to the successful operation of the HFSWR at night time.

The radar cross section of the aircraft employed in the trial has been estimated and compared with theoretical calculations, and the results showed good agreement. The results of these trials, together with those from other trials (ship and iceberg detection trials) provided useful information from which a realistic set of system specifications of the demonstration radar can be established. Nevertheless, much work remains to be done. The next phase of the work would be focused on the analysis of noise and interference data and the development of effective calibration and interference suppression techniques.

## TABLE OF CONTENTS

<b>1.</b>	<b>INTRODUCTION. ....</b>	<b>1</b>
<b>2.</b>	<b>THE EXPERIMENTAL HFSWR FACILITIES ....</b>	<b>2</b>
<b>2.1</b>	<b>The Cape Bonavista HFSWR facility. ....</b>	<b>2</b>
<b>2.1.1</b>	<b>Transmit facility ....</b>	<b>2</b>
<b>2.1.2</b>	<b>Receive facility ....</b>	<b>4</b>
<b>2.1.3</b>	<b>Waveforms ....</b>	<b>5</b>
<b>2.1.4</b>	<b>Experimental set-up. ....</b>	<b>5</b>
<b>2.2</b>	<b>The Cape Race HFSWR facility. ....</b>	<b>5</b>
<b>2.2.1</b>	<b>Transmit facility ....</b>	<b>5</b>
<b>2.2.2</b>	<b>Receive facility ....</b>	<b>5</b>
<b>2.2.3</b>	<b>Waveform ....</b>	<b>6</b>
<b>2.2.4</b>	<b>Experimental set-up. ....</b>	<b>9</b>
<b>2.3</b>	<b>Limitations of the experimental facilities. ....</b>	<b>9</b>
<b>2.3.1</b>	<b>Limited data storage capacity for the Cape Bonavista radar. . .</b>	<b>9</b>
<b>2.3.2</b>	<b>Relatively coarse range resolution for the Cape Bonavista data. ....</b>	<b>10</b>
<b>2.3.3</b>	<b>Ambiguous range response in the Cape Race data. ....</b>	<b>11</b>
<b>2.3.4</b>	<b>Ambiguous azimuthal response in the Cape Race HFSWR. ....</b>	<b>11</b>
<b>3.</b>	<b>THE HFSWR SIGNAL ENVIRONMENT, SIGNAL PROCESSING, DETECTION AND TRACKING. ....</b>	<b>14</b>
<b>3.1</b>	<b>The HFSWR signal environment. ....</b>	<b>14</b>
<b>3.1.1</b>	<b>Sea clutter. ....</b>	<b>16</b>
<b>3.1.2</b>	<b>Ionospheric reflection ....</b>	<b>18</b>
<b>3.1.3</b>	<b>Meteor and meteor trails ....</b>	<b>21</b>
<b>3.1.4</b>	<b>Co-channel communications interference ....</b>	<b>22</b>
<b>3.1.5</b>	<b>Noise components ....</b>	<b>24</b>
<b>(a)</b>	<b>Atmospheric noise ....</b>	<b>25</b>
<b>(b)</b>	<b>Galactic noise ....</b>	<b>25</b>
<b>(c)</b>	<b>Man-made noise ....</b>	<b>25</b>
<b>(d)</b>	<b>CCIR estimates of the median noise levels at Cape Bonavista and Cape Race. ....</b>	<b>25</b>

3.1.6	Targets .....	27
(a)	Constant velocity targets .....	29
(b)	Manoeuvring targets .....	29
3.2	Signal processing. ....	30
3.2.1	The surface-wave radar equation .....	31
3.2.2	Doppler processing .....	35
3.2.3	Digital beam forming with a multi-element receive array. ....	37
3.3	Detection and tracking. ....	37
3.3.1	Detection algorithm. ....	38
3.3.2	Tracking Algorithm. ....	42
4.	TRIAL RESULTS. ....	44
4.1	Data quality. ....	46
4.1.1	Cape Bonavista Data. ....	46
4.1.2	Cape Race Data. ....	47
4.2	Maximum detection range .....	48
4.2.1	Cape Bonavista results .....	48
(a)	16 MHz trial. ....	48
(b)	4 MHz trial. ....	49
(c)	7 MHz trial. ....	51
(d)	Summary of Cape Bonavista results. ....	52
4.2.2	Cape Race results. ....	53
4.3	Tracking of manoeuvring targets .....	56
4.3.1	King-Air 200 in figure-eight manoeuvre .....	56
4.3.2	T-33 in banking manoeuvre .....	61
4.4	Targets of opportunity .....	63
4.4.1	Commercial airliners and military aircraft .....	63
4.4.2	Unknown target .....	69
4.5	Estimation of target radar cross section .....	71
4.6	Probable causes for the Cape Race radar's performance deficiency. . .	80

5.	<b>CONCLUSIONS.</b>	82
6.	<b>REFERENCES.</b>	84
7.	<b>ACKNOWLEDGEMENT.</b>	85
8.	<b>APPENDICES.</b>	86
	<b>Appendix A. NEC modelling of the RCS of the Beechcraft King-Air 200.</b>	86
	<b>Appendix B. Cape Bonavista Radar Log</b>	88
	<b>Appendix C. Cape Race experimental data log.</b>	91



## LIST OF FIGURES

Figure 1.	Geographical locations of the two HFSWR testbeds. . . . .	2
Figure 2.	The Cape Bonavista HFSWR facility . . . . .	3
Figure 3.	Layout of the receive array at Cape Bonavista. . . . .	4
Figure 4.	The Cape Race HFSWR facility. . . . .	7
Figure 5.	Layout of the antenna arrays at Cape Race. . . . .	8
Figure 6.	Range profile of the Doppler component corresponding to the velocity of an aircraft target. . . . .	11
Figure 7.	Range profile of a Doppler component showing ambiguous range response. . . . .	12
Figure 8a.	Elemental and array patterns with the same pointing direction. . . . .	13
Figure 8b.	Elemental and array patterns with different pointing directions . . . . .	13
Figure 9.	3-D view of the HFSWR environment. . . . .	15
Figure 10.	Typical sea-clutter spectrum from the Cape Bonavista HFSWR. . . . .	17
Figure 11a.	Range profile of a Doppler component showing strong ionospheric reflection. . . . .	19
Figure 11b.	Doppler spectrum of the time series from a range with strong ionospheric reflection. . . . .	19
Figure 12.	Waveform of the time series for a range with strong ionospheric reflection. . . . .	20
Figure 13.	Observed ionospheric clutter strength as a function of azimuth. . . . .	21
Figure 14.	Waveform of the time series for a range with echoes from meteor trails.. . . .	23
Figure 15.	Spectrum of the time series containing echoes from meteor trails. . . . .	24
Figure 16.	Comparison between CCIR predicted and measured noise levels as a function of time. . . . .	28
Figure 17.	Typical spectrum of a range cell with a constant velocity target. . . . .	29

## LIST OF FIGURES (Continue)

Figure 18.	Spectrum of the returns from a T-33 in banking manoeuvre. . . . .	30
Figure 19.	Regions for determining the threshold in a Doppler-averaging CFAR. . .	40
Figure 20.	Range-Doppler profile of a manoeuvring aircraft. . . . .	41
Figure 21.	Range profile of the manoeuvring aircraft in Figure 19. . . . .	42
Figure 22.	A Lockheed T-33 training jet aircraft. . . . .	44
Figure 23.	A Beechcraft King-Air 200 aircraft . . . . .	45
Figure 24.	A Canadair Challenger 601-3A aircraft. . . . .	45
Figure 25.	Array pattern of the Cape Bonavista receive antenna at 15.77 MHz.. . . .	49
Figure 26.	Doppler spectrum of a range where the King-Air was detected. . . . .	50
Figure 27.	Target energy of the King-Air as a function of range at 15.77 MHz. . . .	50
Figure 28.	Target energy of the King-Air as a function of range at 4.1 MHz. . . . .	51
Figure 29.	Target energy of the King-Air as a function of range at 6.9 MHz. . . . .	52
Figure 30.	Target energy of the King-Air as a function of range at 5.81 MHz. . . . .	53
Figure 31.	Target energy of the King-Air as a function of range at 5.81 MHz. . . . .	54
Figure 32.	Target energy of the King-Air as a function of range at 5.81 MHz. . . . .	54
Figure 33.	Target energy of the King-Air as a function of range at 5.81 MHz. . . . .	55
Figure 34.	Target energy of the King-Air as a function of range at 5.67 MHz. . . . .	55
Figure 35.	Target energy of the Challenger as a function of range at 5.81 MHz. . . .	57
Figure 36.	Target energy of the Challenger as a function of range at 5.81 MHz. . . .	57
Figure 37.	Radial velocity of the Challenger as a function of range.. . . .	58
Figure 38.	Radial velocity of the Challenger as a function of range.. . . .	58
Figure 39.	Degradation of detection performance due to co-channel interference. . . .	59

## LIST OF FIGURES (Continue)

Figure 40.	Track of the King-Air 200 in figure-eight manoeuvre. . . . .	60
Figure 41.	Spectra of a manoeuvring aircraft near tangential heading. . . . .	62
Figure 42.	Comparison of peak energy and total energy of the King-Air in figure-eight manoeuvre. . . . .	63
Figure 43.	Track of the T-33 in an experiment with banking manoeuvre. . . . .	64
Figure 44.	Comparison of peak and total target energies for a T-33 in banking manoeuvre. . . . .	65
Figure 45.	Accumulated tracks derived from data file AIR_SIX. . . . .	66
Figure 46.	Radial velocity of an unidentified aircraft as a function of range. . . . .	68
Figure 47.	Target energy as a function of bearing for an unidentified aircraft. . . . .	68
Figure 48.	Target energy as a function of range for a probable airliner. . . . .	69
Figure 49.	Accumulated tracks derived from data file AIR_SEVEN. . . . .	70
Figure 50.	Radial velocity of an unidentified aircraft as a function of range. . . . .	71
Figure 51.	Accumulated tracks derived from data file AIR_TEN. . . . .	72
Figure 52.	Echo energy as a function of bearing for an unidentified target. . . . .	73
Figure 53.	I-channel waveform for a number of range bins containing an unidentified target. . . . .	74
Figure 54.	Comparison of the target energy between a King-Air and a Challenger. . . . .	76
Figure 55.	Compares of the target energy between a King-Air and a T-33. . . . .	76
Figure 56.	Comparison of Bragg energy and target energy of the King-Air at 4 MHz. . . . .	78
Figure 57.	Comparison of Bragg energy and target energy of the King-Air at 5.8 MHz. . . . .	79

## LIST OF FIGURES (Continue)

Figure 58.	Comparison of Bragg energy and target energy of the King-Air at 15.8 MHz. ....	80
Figure A1.	NEC RCS estimates for a King-Air at level flight. ....	84
Figure A2.	NEC RCS estimates for a King-Air at nose-on incidence. ....	85
Figure A3.	NEC RCS estimates for a King-Air rolled 45° to port. ....	85

## List of Tables

Table 1:	Cape Bonavista HFSWR parameters for aircraft detection trials. ....	6
Table 2:	Cape Race HFSWR parameters for aircraft detection trial. ....	10
Table 3:	Median values of the total external noise density at Cape Bonavista assuming a quiet rural site. ....	26
Table 4:	Median values of the overall noise densities at Cape Race assuming a rural and a quiet rural site at 6 MHz. ....	27
Table 5:	Summary of Cape Bonavista Aircraft-Trial data. ....	46
Table 6:	Summary of Cape Race Aircraft-Trial data. ....	47
Table 7:	Comparison of RCS estimates for the King-Air 200 between NEC modelling and experiment. ....	79

## 1. INTRODUCTION.

A series of aircraft-detection trials [1-3] was conducted using experimental high-frequency surface-wave radars (HFSWR) located on the east coast of Newfoundland, Canada. Two HFSWR testbeds were used in these trials, one at Cape Bonavista, the other at Cape Race.

The Cape Bonavista facility was first developed and operated by Nordco Limited for DND. The HF radar section of Nordco was subsequently taken over by Raytheon Canada Limited (RCL), and RCL has since been under contract to the DND to carry out experimental trials. Initially, the Cape Bonavista HFSWR facility operated at a relatively low frequency of 1.95 MHz [4], utilizing the existing LORAN A transmitter. The facility was upgraded in 1991 [5] to permit operation at frequencies above 4 MHz. Because of the low average power available from the Cape Bonavista radar, aircraft detection trials had been limited to fixed beam experiments in which the antenna array formed a single beam (in the boresight direction), and the radar operated at a relatively high pulse repetition frequency (PRF) to yield a reasonable level (a few tens of watts) of average power.

The Cape Race facility is owned and operated by Northern Radar Systems Limited (NR) of St. John's, Newfoundland. This company has operated a HFSWR for the past fifteen years, primarily for experimenting with detection and tracking of surface vessels and the monitoring of ocean surface conditions. The Cape Race facility operates at a nominal frequency of 5.8 MHz and utilizes the Frequency Modulation Interrupted Continuous Wave (FMICW) waveform. The FMICW is a relatively wide-band waveform and yields a reasonably high range resolution.

By utilizing both HFSWR facilities in aircraft detection trials, it was hoped that some first-hand experience in over-the-horizon (OTH) detection of low-altitude aircraft could be gained. In the process of analyzing the trial data, some useful insights into a number of parameters in the HFSWR signal environments have been obtained. These insights are crucial to the development of signal processing strategies that ensure the successful operation of HFSWR in long range coastal surveillance applications.

In this report, we seek to answer some of the questions pertaining to the performance of HFSWR in detection of low-altitude aircraft. These are: (i) what is the maximum detection range for a given target, (ii) at what transmit power is this performance obtained, (iii) how do the experimental results compare with the predictions from theory and (iv) what is the typical signal environment that the HFSWR is operating in? Answers to these questions would facilitate the determination of the required transmit power, optimum frequency and waveform.

Section 2 of this report describes the technical aspects of the two HFSWR test beds. Section 3 presents the HFSWR signal environment as observed by the two test beds. These include a catalog of interference sources and their behaviour in the time, frequency and spatial domains. The signal processing techniques employed for target detection and tracking are also described. Section 4 presents the results of the analysis of the trial data. Section 5 presents the conclusions and a discussion of future work.

## 2. THE EXPERIMENTAL HFSWR FACILITIES

The geographical locations of the two radar sites are shown in Figure 1. The latitude-longitude positions for the Cape Bonavista facility are (48:41:14N, 53:05:24W), and those for Cape Race are (46:39:08N, 53:06:20W). The coverage of both radars is a fan-shape area. A brief description of the two facilities and the radar parameters employed in the aircraft-detection trials are presented in the following two sub-sections.

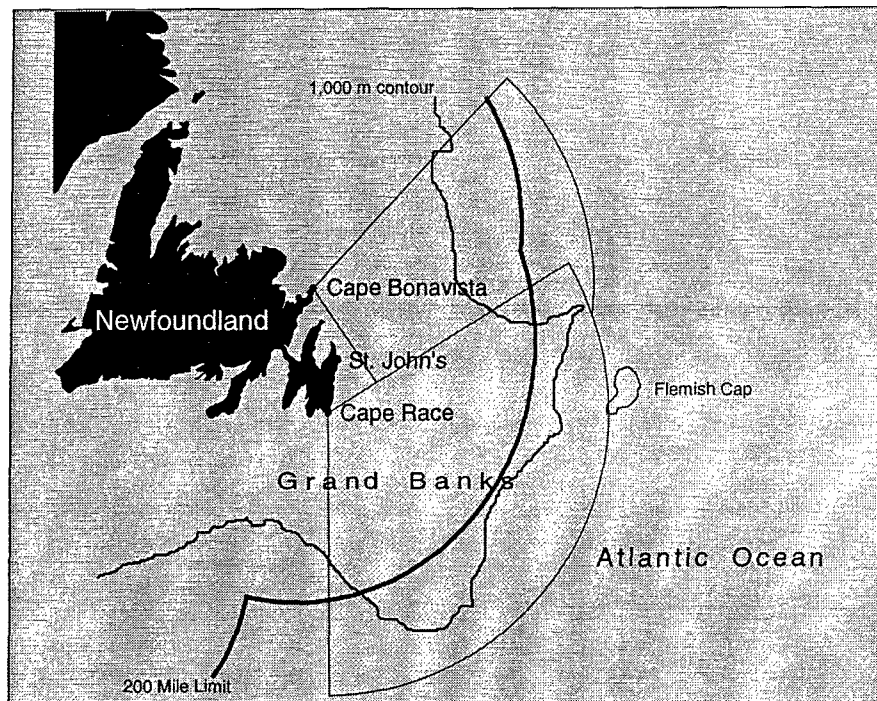
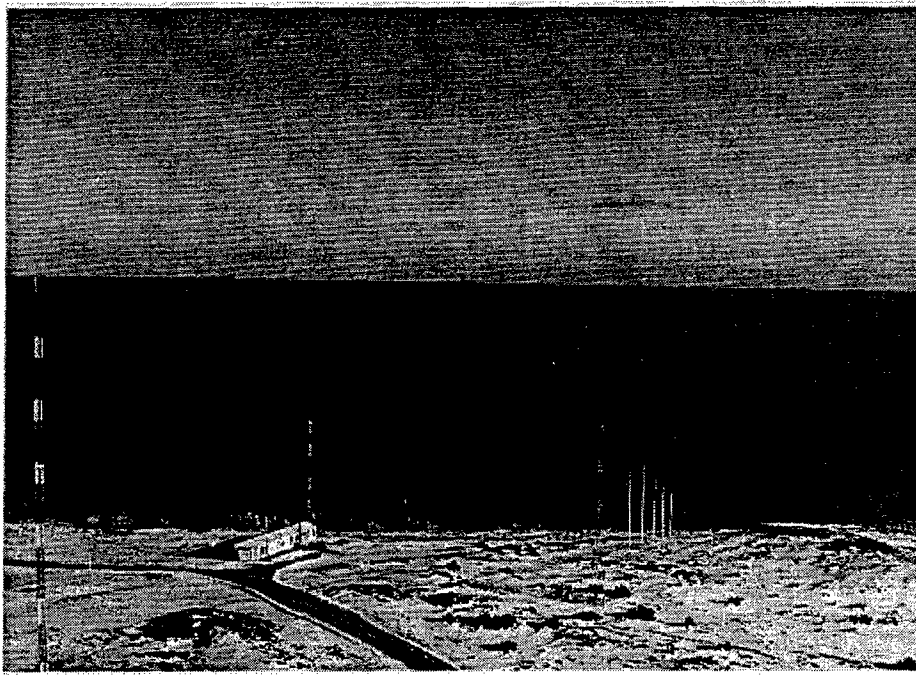


Figure 1. Geographical locations of the two HFSWR testbeds.

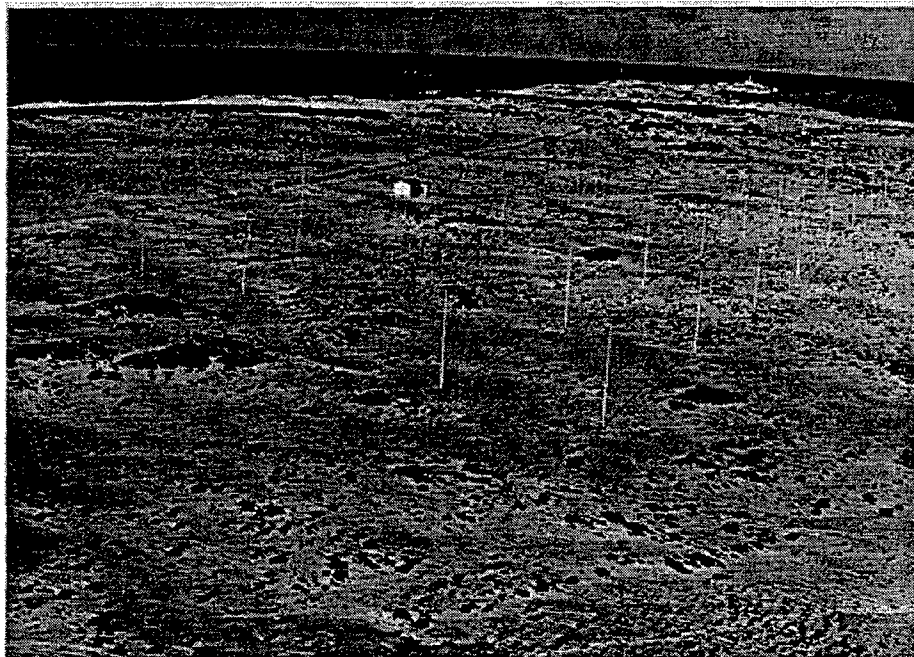
### 2.1 The Cape Bonavista HFSWR facility.

#### 2.1.1 Transmit facility

The HFSWR facility at Cape Bonavista is shown in Figure 2. The transmitter was housed in a decommissioned Coast Guard building used for the Loran A transmitter. The transmitter was the Analogic Model AN8069 power amplifier comprising four 2-kW AN8062 RF modules. This transmitter could operate at a maximum duty cycle of 10 percent. The transmit antennas comprised two log-periodic monopole arrays. One, modified from a number of monopoles manufactured by Valcom, was for frequencies below 6 MHz, the other, manufactured by Andrews, was for frequencies above 6 MHz. The Valcom and Andrews antennas yielded theoretical gains of approximately 10 dBi and 3-dB beamwidths of about 100° at a nominal frequencies of 4 MHz and 15 MHz, respectively.



(a) Transmit facility.



(b) Receive facility.

Figure 2. The Cape Bonavista HFSWR facility.

### 2.1.2 Receive facility

The receive facility employed two receive arrays for operations below and above 10 MHz, respectively. The receive array for below 10 MHz operations was composed of eight doublets of monopoles supplied by VALCOM. The two monopoles in a doublet were spaced 19.23 metres apart, which represented a quarter wavelength at 3.9 MHz. The outputs of the two monopole antennas in a doublet were combined with the proper phasing so that signals coming from the rear of the antenna array would be suppressed. This yielded a front-to-back ratio of about 10 dB. The separation between two doublets was 38.46 metres, equivalent to half wavelength at 3.9 MHz. The receive array for operations above 10 MHz comprised eight singlet monopoles fabricated at DREO. The elements in the array were made of solid brass rods with adjustable length. The monopoles were separated by a distance of 10 metres (one half wavelength at 15 MHz). Figure 3 shows the configuration of the receive facility at Cape Bonavista.

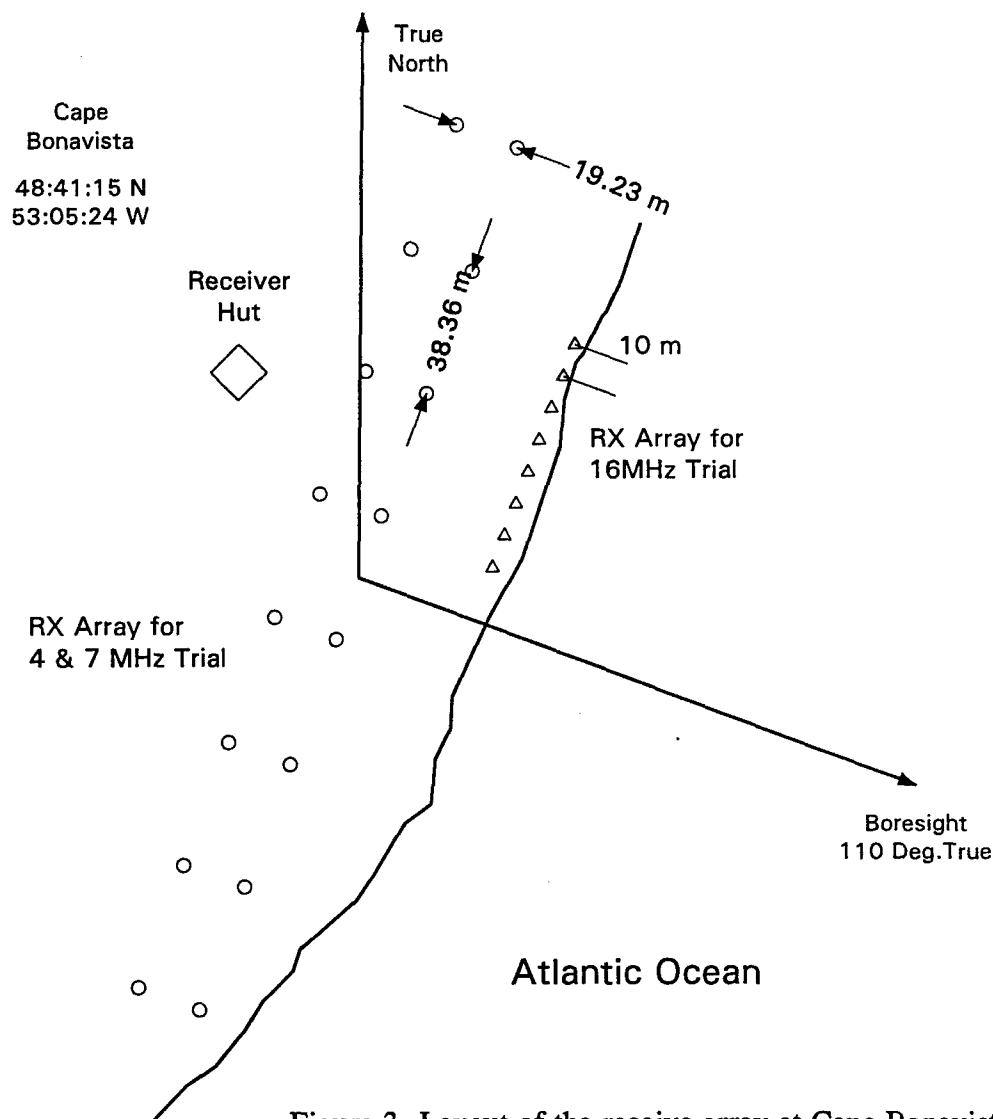


Figure 3. Layout of the receive array at Cape Bonavista.



Four Raytheon TT254 Digital Receivers were coupled to the receive antennas via a multiplexing unit. These receivers performed all the demodulation, digitization, and filtering functions. The receivers had a bandwidth of about 100 kHz although most of the waveforms used had bandwidths less than 30 kHz. The radar signal was sampled after the intermediate frequency (i.f. 25 kHz) stage at a rate of 125 kHz and digitally demodulated down to complex (in-phase and quadrature phase) baseband. At a rate of 125 kHz the radar signal was sampled once every 8  $\mu$ sec which corresponded to a spatial separation of 1.2 km. A SUN SPARC 20 work station served as the control console.

### **2.1.3 Waveforms**

The Cape Bonavista HFSWR facility supports two types of waveforms. The first uses a simple raised cosine pulse, with a nominal pulse length of 50  $\mu$ sec. The other type uses bi-phase codes, including the Barker pulse-compression waveforms. For the aircraft detection trial, a 50  $\mu$ sec raised cosine pulse waveform was used. The system PRF was programmable and the value was determined from consideration of the duty-cycle limitation, the transmit pulse length, the maximum unambiguous range and the maximum expected target speed. For the Cape Bonavista radar, the unambiguous Doppler domain was equal to the PRF.

### **2.1.4 Experimental set-up.**

For the aircraft-detection trial, the outputs of the eight receive elements were connected together before being fed to a single receiver. This arrangement provided a slightly higher average power because the receivers did not need to be multiplexed between two antennas (there were eight antennas but only four receivers), and a high PRF could be employed. It also yielded a longer data-recording time because, instead of having to record data from all eight channels, only data from one channel needed to be recorded. A limitation was that only single-beam experiments could be carried out at Cape Bonavista, with the aircraft's flight path confined to the boresight direction. Table 1 summarizes the experimental parameters employed in the Cape Bonavista Radar during the aircraft detection trial.

## **2.2 The Cape Race HFSWR facility.**

### **2.2.1 Transmit facility**

The HFSWR facility at Cape Race is shown in Figures 4. The radar operated in a monostatic mode. The transmitter comprised four Kalmus LP4000HV/2 power-amplifier modules, with 4 kW peak power each. Northern Radar's engineers estimated that the effective peak radiated power was about 8 kW. The transmit antenna was a log-periodic dipole array having a wide bandwidth (5.4 to 32 MHz). The front-to-back ratio was 15 dB, and the half power beamwidth was 126°.

### **2.2.2 Receive facility**

The receive facility of the Cape Race HFSWR consists of an array of 40 folded monopole antennas. Figure 5 depicts the lay-out of the receive array. Ten Steinbrecher Model 16030A

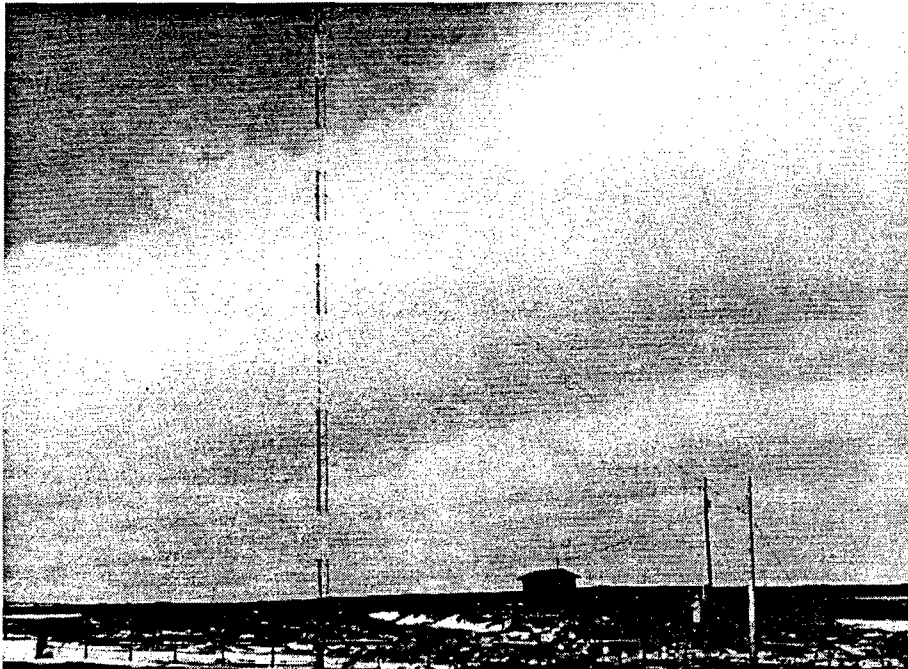
**Table 1: Cape Bonavista HFSWR parameters for aircraft detection trials.**

Transmit	
Nominal Frequency:	4 MHz 7 MHz 16 MHz
Antenna:	4 MHz: 5-element Log-periodic monopole array, 10 dBi. 7,16 MHz: Log-periodic dipole array; 11 dBi
Waveform:	50 $\mu$ sec raised cosine pulse.
Peak power:	5 kW @ 4 MHz; 8 kW above 5 MHz
Duty cycle:	0.5%
Waveform repetition frequency	100 Hz
Receive	
Antenna: $f < 10$ MHz	eight-element doublet monopole array
$f > 10$ MHz	eight-element singlet array
Receiver	effective bandwidth = 20 kHz.
Signal Processing:	Demodulation; Data recording

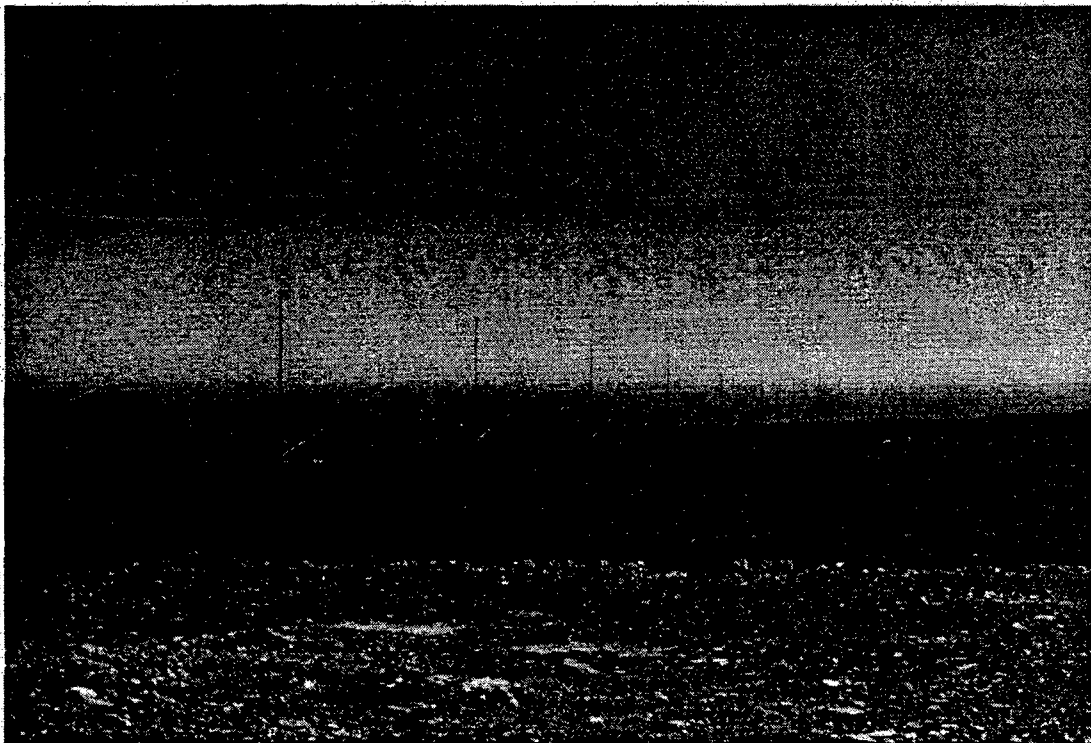
receivers were coupled to the antennas. With only ten receivers and forty antennas, the outputs of four adjacent receive antennas were first combined via a hardware beamformer and fed into one of the ten receivers. The combined antenna pattern of four adjacent antennas could be made to point to a number of angles with a 33-degree sector by selecting the appropriate element phasing in the hardware beamformer. This permitted the radar to monitor four different sectors. However, this arrangement resulted in grating lobes that gave rise to azimuthal ambiguities for the targets. This did not affect the tracking of controlled targets since the bearing of the aircraft was known.

### 2.2.3 Waveform

The frequency modulated, interrupted continuous wave (FMICW) waveform was used exclusively in the Cape Race radar. The FMICW is a pulse-compression waveform. The transmitter emits a sequence of coherent pulses whose carrier frequency varies linearly with time. The instantaneous bandwidth is not very large, in the order of several kHz. However, the carrier frequency is swept over a relatively wide bandwidth (over 100 kHz). Pulse compression takes place over a number of contiguous pulses. The duration of the sequence of transmitted pulses is

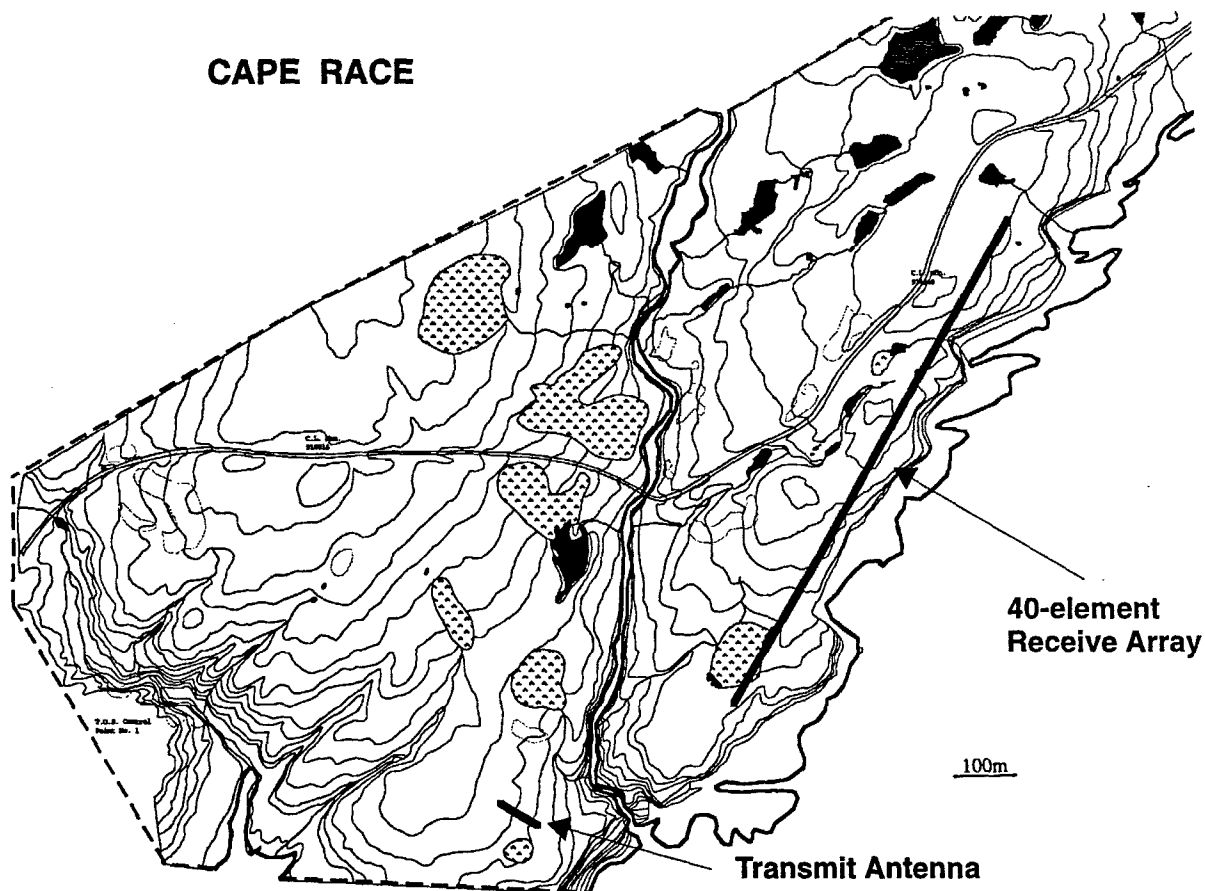


(a) Transmit antenna.



(b) Receive antenna array.

Figure 4. Cape Race HF/SWR facility.



courtesy of Northern Radar Systems Limited

Figure 5. Layout of the antenna arrays at Cape Race.

called the FM sweep period, and the frequency range in which the carrier varies over one FM sweep period is called the FM sweep bandwidth. Between pulses, the transmitter is turned off, and the echoes are received.

The received signal is mixed with the transmitted signal and translated down to an intermediate frequency (i.f.) of 25 kHz and then low-pass filtered and sampled. Since the echo signals are basically delayed version of the mixer signal (in this case, linear FM), the mixer output is a superposition of many sinusoidal waveforms whose frequency is directly proportional to the range of the scatterer that produces the echo. After the entire sequence of pulses is transmitted and the echoes received, digital pulse compression is performed on the received signal that yields one sample of the time series for each range. The above sequence of operations is repeated in subsequent FM sweep periods, and time series for all compressed range cells are collected. The detailed operation of the FMICW may be found in [6].

For the Cape Race radar, the Doppler domain was equal to the waveform repetition frequency (WRF). For simple uncoded waveforms, the PRF is equal to the WRF. The distinction between PRF and WRF comes about in radars employing pulse-compression waveforms that require a number of contiguous pulses to complete the compression. In this case, the WRF is equal to the reciprocal of the time spanned by the sequence of pulses.

#### **2.2.4 Experimental set-up.**

Up until the time of the aircraft-detection trial, the Cape Race radar had been optimized for surface-ship detection, which emphasized high range and Doppler resolutions. The nominal parameters for the FMICW waveform were (i) FM sweep bandwidth = 375 kHz, (ii) FM sweep period 0.5 second and (iii) transmit pulse length = 240  $\mu$ sec. These yielded a range resolution of about 400 m and a Doppler domain of only 2 Hz. For aircraft detection, the above values are inappropriate. First, the Doppler domain spanned by aircraft targets is substantially wider than 2 Hz. This gives rise to blind-speed regions where high speed targets are aliased into low-Doppler region where they would be submerged in sea clutter. Second, a range resolution of 400 m would severely limit the coherent integration time that can be employed. For example, a Mach 1 target remains in a 400 m range cell for only 1.2 seconds. For this trial, the system was modified so that it would have a Doppler domain of about 10 Hz and a range resolution of 1.2 km. The resulting system parameters are listed in Table 2.

### **2.3 Limitations of the experimental facilities.**

Because the two HFSWR facilities were experimental, there were limitations that degraded the trial results. In evaluating the present set of trial results, these limitations must be kept in mind.

#### **2.3.1 Limited data storage capacity for the Cape Bonavista radar.**

The nominal speed of the aircraft used in the trial was about 200 knots ( $\sim 103$  m/sec). The trial plan called for the aircraft to fly out beyond 100 km range and then turn back. Hence, the total time for a run was about thirty minutes. Because the radar cross section (RCS) of the aircraft is rather low, the average power of the radar must be maximized by employing a high PRF ( $\geq 100$  Hz). The sampling rate of the radar was 125 kHz. This meant that the returned waveform was sampled every 8  $\mu$ sec. If the returns for a maximum of 160 range samples (about 192 km) were to be retained, 16000 complex samples must be stored in each second for each receiver channel. Since there were eight receiver channels, 920 Megabytes (Mb) of random access memory (RAM) would be needed if a full sampled-aperture-data set was to be acquired. This far exceeded the RAM capacity of the Cape Bonavista radar. As a result, it was decided that the trials at Cape Bonavista would be confined to fixed-beam experiments. The eight receiver antenna elements were combined at RF and fed to a single receiver. This meant that the radar was not able to track manoeuvring targets since it could not determine their bearings, but the data storage requirement was reduced to about 115 Mbytes.

**Table 2: Cape Race HFSWR parameters for aircraft detection trial.**

Transmit	
Frequency:	5.811 MHz.
Antenna:	Log-periodic dipole array (Gain $\approx$ 10 dBi).
Waveform:	Frequency modulated, interrupted continuous wave (FMICW), BW = 125 kHz; transmit pulse length = 240 $\mu$ sec.
Peak power:	8 kW
Duty cycle	8 %
WRF:	9.01 Hz
Receive	
Antenna:	40-element array.
Receiver	effective bandwidth = 125 kHz.
Signal Processing:	Demodulation; Digital pulse compression; and Data recording

### 2.3.2 Relatively coarse range resolution for the Cape Bonavista data.

The range resolution of a radar is a function of the signal bandwidth which is nominally equal to the reciprocal of the pulse length. For the Cape Bonavista radar, the signal bandwidth was 20 kHz (i.e., the reciprocal of 50  $\mu$ sec), yielding a range resolution of about 7.5 km. This presented some complications in the constant false alarm operation because of the large range extent of the target main lobe and its range sidelobes. Figure 6 shows the range profile of the Doppler component corresponding to the velocity of an aircraft target. The range of the aircraft was obtained by locating the maximum which was at 42 km. It can be seen that the main lobe of the target echo (within which the echo magnitude was more than 10 dB above the noise floor) occupied a range extent in excess of 25 km, and the range sidelobe was fairly high. This means that when range-averaging constant-false-alarm-rate (CFAR) algorithms are employed, the guard zone must be sufficiently large to prevent the threshold setting from being corrupted by the target response. This could present complications when the target Doppler is low, and the range response may contain residual sea-clutter components. In addition another target having the same radial velocity as this target cannot be resolved by the radar. In a practical operating environment, however, the probability of finding two air targets having exactly the same radial velocity in the same resolution cell is rather remote.

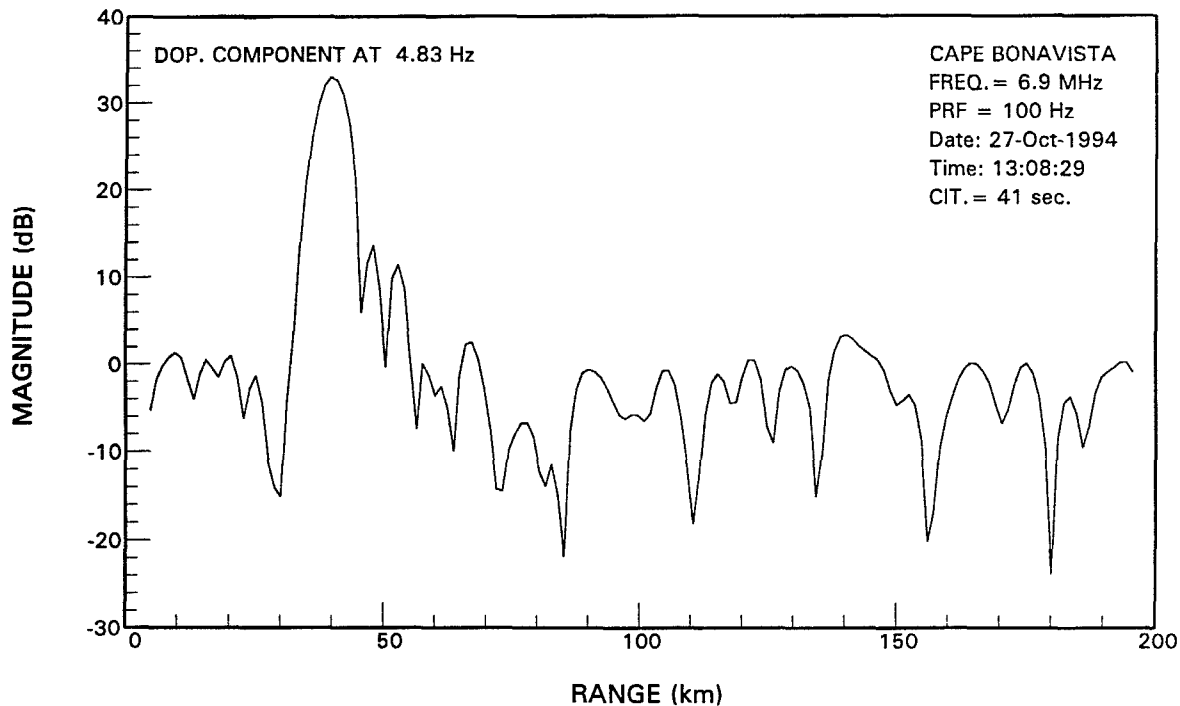


Figure 6. Range profile of the Doppler component corresponding to the velocity of an aircraft target.

### 2.3.3 Ambiguous-range response in the Cape Race data.

In analyzing the Cape Race data, it was found that there existed an anomalous response that was periodic in range. This anomalous behaviour was observed most frequently in a few Doppler bins around zero. Occasionally, however, it can also be seen at higher Doppler frequencies. Figure 7 shows the range profile of a particular Doppler bin for the Cape Race radar over a time interval. It can be seen that periodic spikes appear in range, with a period of 32 range cells (or about 38.4 km). In consultation with the NR engineers, it was found that this anomalous response was the result of the sub-optimal implementation of the pulse-compression scheme for the FMICW waveform. These ambiguous-range responses gave rise to false detections; however, these can be eliminated by the tracking algorithm because these false targets do not migrate to other ranges.

### 2.3.4 Ambiguous azimuthal response in the Cape Race HFSWR.

The Cape Race radar had a further complication in regard to the bearing estimate. This was the result of the sub-array configuration used in that radar. The Cape Race radar had only ten receiver channels. With forty antenna elements, groups of four adjacent antennas were first combined, in a sub-array configuration, to form a composite element. These composite elements could be electronically phased to point in a specific direction. The resulting ten composite elements were then fed to the ten receiver channels. The effective separation of the composite elements was about  $1.7\lambda$  at a frequency of 5.75 MHz. This produced an antenna pattern that was periodic in angle (grating lobes).

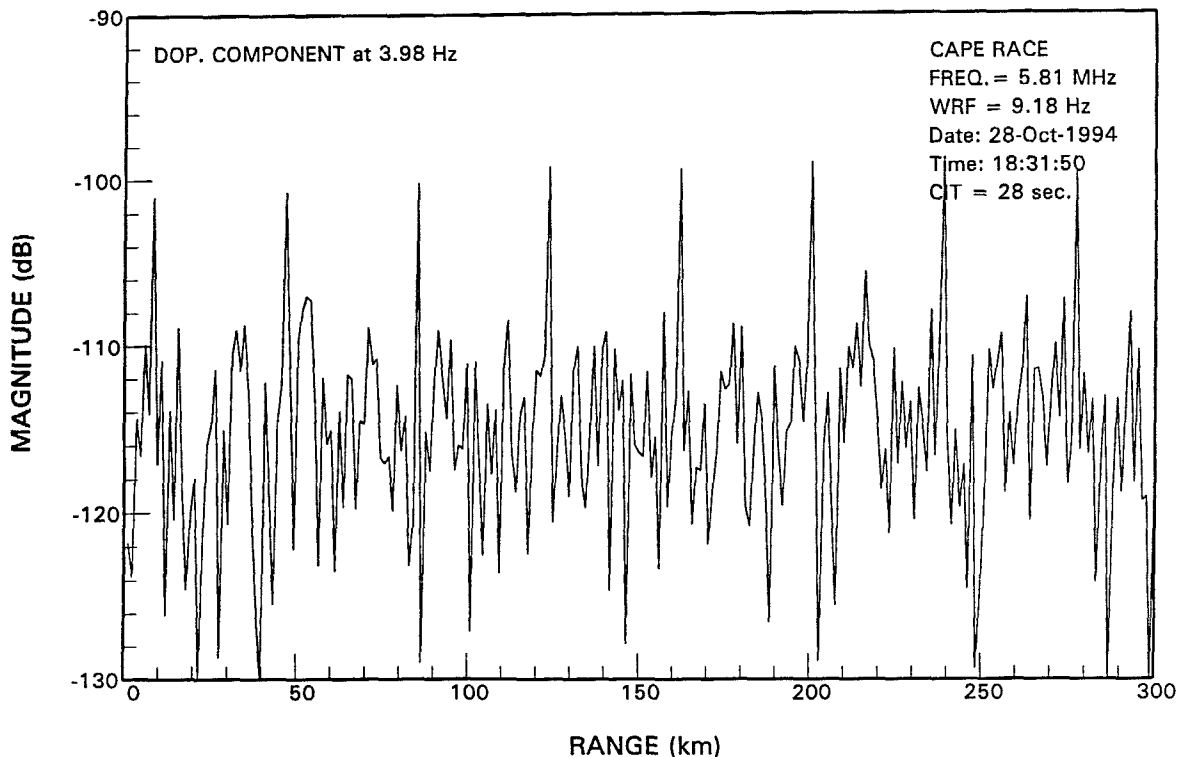


Figure 7. Range profile of a Doppler component showing ambiguous range response.

The grating lobes of the synthesized array patterns, except those of the one pointing at the same direction as that of the composite elements, will not coincide with the nulls of the elemental pattern. Figure 8a shows the antenna pattern (in dashed line) of the composite element pointing at the boresight ( $121^\circ$  true) of the receive array. This pattern was obtained from measurements carried out at 5.75 MHz. The 3 dB beamwidth was about  $33^\circ$ . With ten receiver channels, array patterns can be synthesized from the signals such that the main lobe points to any direction in a sector covered by the pattern of the composite element. The total antenna pattern of this array is the product (or the sum in dB scale) of the array pattern and the elemental pattern, assuming all the elements are identical. The total pattern pointing in the boresight direction is shown as the solid curve in Figure 8a. The beamwidth of the array pattern was about  $2.5^\circ$ . One of the grating lobes is seen to be at an angle about  $36^\circ$  off the main lobe, and it coincides with the first null of the elemental pattern. Consequently, when both the array and the elemental patterns are pointing in the same direction, the effects of the grating lobes are negligible.

The combined pattern (both array and elemental patterns) of the Cape Race receiving array pointing in a direction  $-17^\circ$  off boresight is shown as the solid curve in Figure 8b. It can be seen that, in addition to the main beam pointing at  $104^\circ$  ( $121^\circ - 17^\circ$ ), there is another beam (a grating lobe) pointing at about  $139.5^\circ$ . Ambiguity will arise when there is a target at the  $139.5^\circ$  azimuth, and the radar may indicate its azimuth as  $104^\circ$ . Consequently, the tracking algorithm must be designed to resolve this ambiguity.



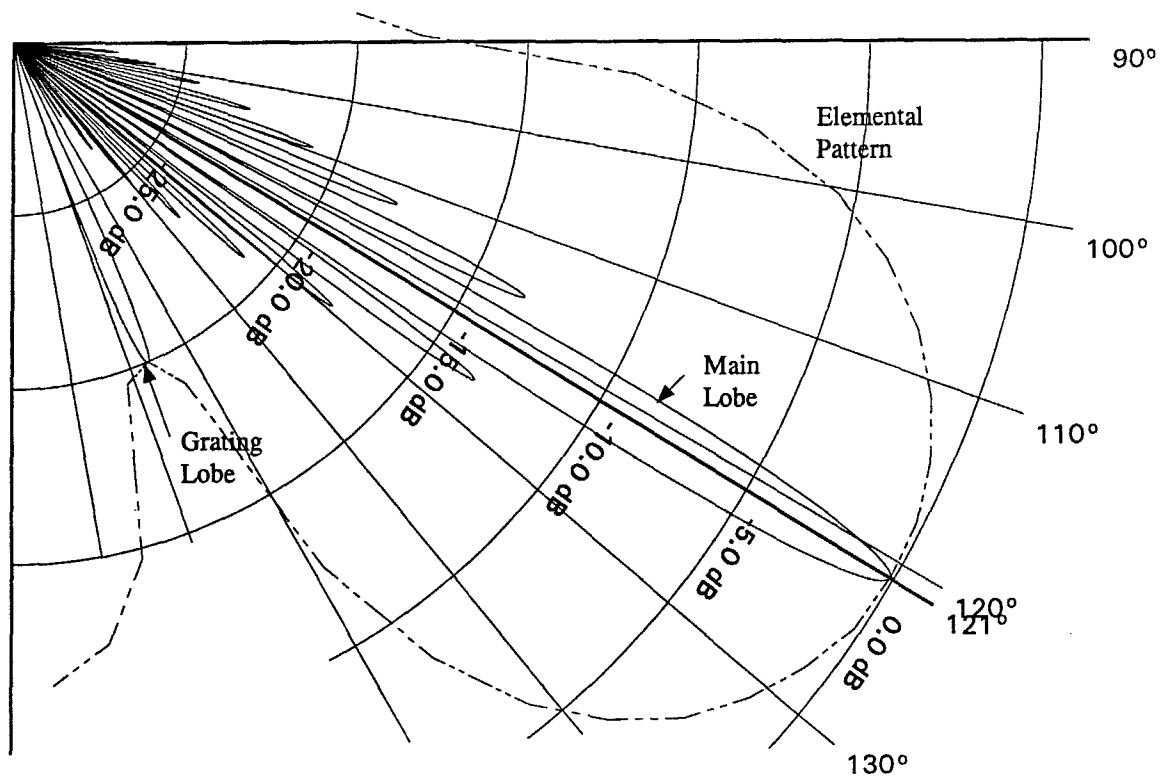


Figure 8a. Elemental and array patterns with the same pointing direction.

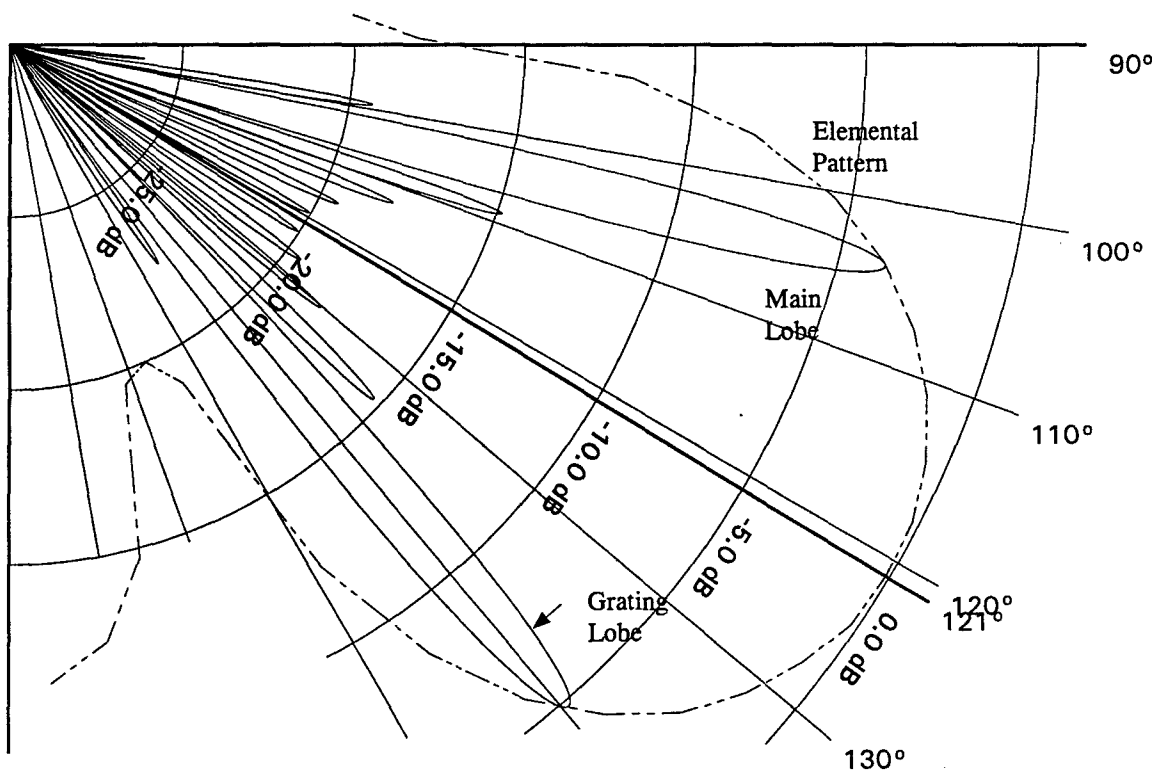


Figure 8b. Elemental and array patterns with different pointing directions.

### 3. THE HFSWR SIGNAL ENVIRONMENT, SIGNAL PROCESSING, DETECTION AND TRACKING.

#### 3.1 The HFSWR signal environment.

The signal environment in which an HFSWR operates differs from that of microwave radars in several aspects. First, a well designed HFSWR is generally external-noise limited, except during a brief period at mid-day at quiet rural sites. This means that sub-optimal antenna elements and receivers with moderate gains may be used (e.g. monopoles with length less than a quarter wavelength) in the receive array without degrading the signal-to-noise ratio (SNR). The reason is that the receive antenna elements in the array should have a broad gain pattern, with the peak element gain near the horizon at low elevation. The major contributor to the noise is external noise sources. Hence, high element and receiver gains will not alter the SNR as long as the external noise is greater than the receiver noise. However, the array gain is important because a longer array corresponds to a smaller beamwidth, which reduces the azimuthal extent from which external noise is received.

Second, there are few natural external interference sources for microwave radars. Hence, the main concerns for microwave radars are receiver noise, clutter and intentional jamming. There are many sources of interference within the HF band that have very different characteristics. Insights into the characteristics and origins of HF interference would enable a radar engineer to develop mitigating techniques and optimal signal and data processing schemes for detection and tracking.

Third, the detection of targets at long range or in sea clutter by HF radars requires relatively long (in the order of minutes) coherent integration. Targets could change speed significantly during a coherent integration interval. Some insight into the spectral behaviour of manoeuvring targets would help in the design of detection algorithms that can handle such conditions.

Figure 9 provides a graphical representation of the HFSWR signal environment from which various components may be identified. This figure was obtained by displaying the Doppler spectra of the radar returns from all ranges, for a fixed look direction, in 3-D format. The data for this figure were obtained from the Cape Race HFSWR. The spectra were calculated over a time interval of approximately 28 seconds. The x-axis represents the Doppler or velocity, and the y-axis represents the range. The z-axis is the magnitude of the Doppler component in dB (relative to unity). The radar parameters are presented in the figure. The Doppler domain of a radar is equal to the system waveform repetition frequency (WRF) which for this experiment was 9.18 Hz ( $\pm 230$  knots at 5.81 MHz). For display purposes, the magnitudes are hard limited to -115 dB which is slightly above the average noise floor observed in the data. In addition, the components corresponding to the first order sea-clutter return (as will be discussed in Section 3.1.1) have been suppressed in the figure by replacing the values of a few Doppler bins around  $f_B$ , the Bragg-line Doppler frequency (see (1) below), with the average values of a small number of neighbouring bins. This is done so as not to obscure other spectral details of interest.

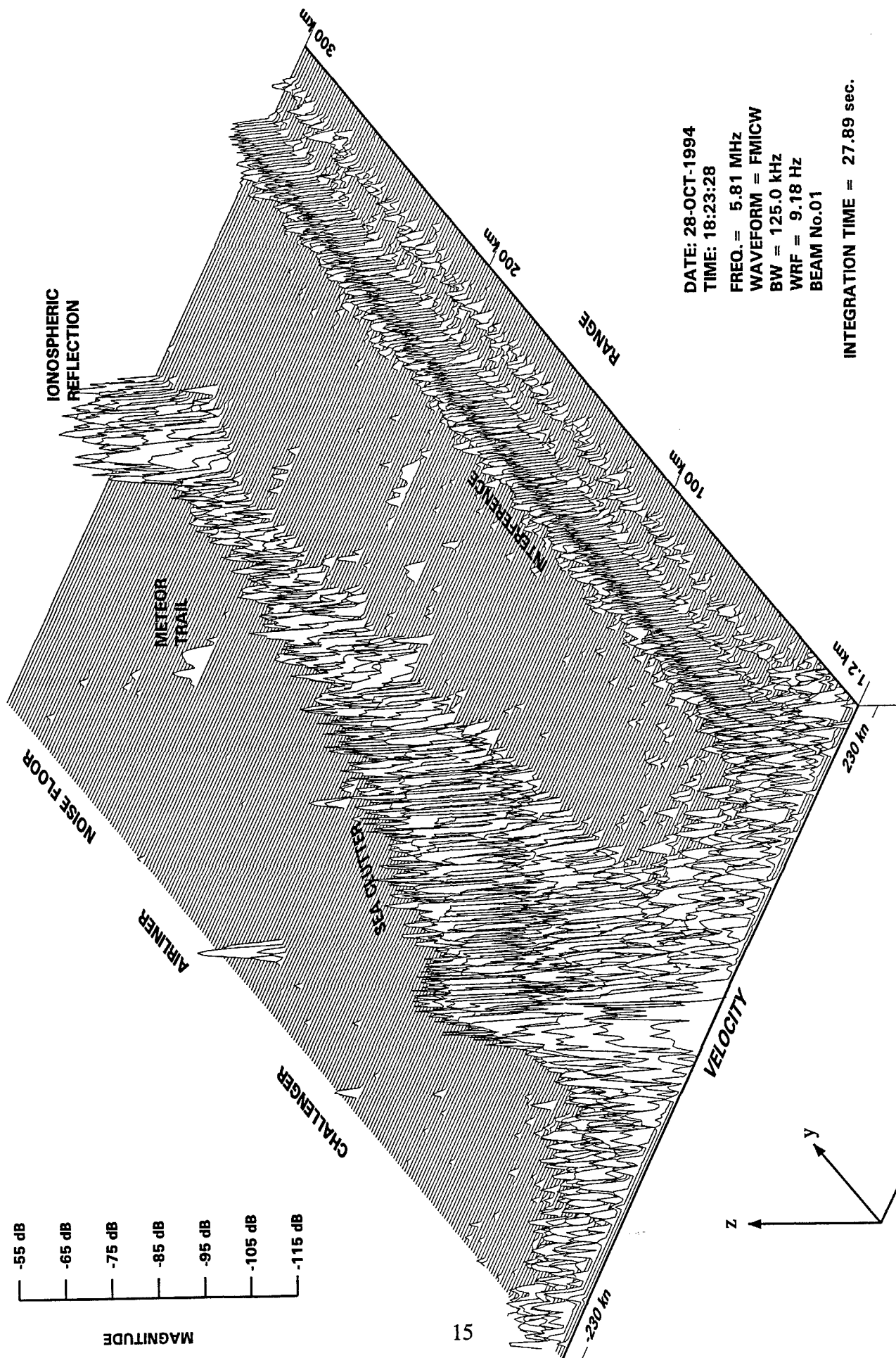


Figure 9. 3-D view of the HF/SWR signal environment.

Most of the signal components pertinent to the radar's operation are labelled in the figure. These include sea clutter, ionospheric reflection, meteor clutter, co-channel communications interference, noise and targets. These components will be illustrated in more detail in subsequent sub-sections.

### 3.1.1 Sea clutter.

The central portion of the spectrum comprises the background signal components against which low speed targets are detected. For ranges less than 100 km, this part of the Doppler spectrum is normally occupied by the sea clutter. Sea clutter is a self-generated interference that results from the reflection of the radar signal off ocean waves. Ocean waves are a result of the interaction of the wind and the gravitational force on the water surface. The dominant component of HF radar sea clutter are the Bragg lines whose apparent Doppler frequency is given by [7]:

$$f_B = \left[ \frac{g}{\pi \lambda} \right]^{\frac{1}{2}} \quad (1)$$

where  $g = 9.81 \text{ m/sec}^2$  is the gravitational acceleration, and  $\lambda$  is the radar wavelength.

Second and higher order peaks observed in the spectrum result from constructive interference of the radar signal after scattering more than once off the wave facets. There are two mechanisms that give rise to the second order sea clutter at HF. The first is a consequence of the fact that gravity waves are not purely sinusoidal. They have relatively sharp crests and broad troughs and are more appropriately represented by trochoidal waves [8]. One can approximate a trochoidal wave by a superposition of the harmonics of the fundamental sinusoidal gravity wave that gives rise to the Bragg lines. A constraint is that these harmonic waves also have the same phase velocity as the fundamental wave. A consequence of these harmonic waves is that sharp spectral lines may occur in the sea-clutter spectrum at discrete frequencies of  $n^{1/2}$ , where  $n$  is the order of the harmonic.

The second mechanism is a consequence of scattering of the radar signal from pairs of crossing ocean waves at right angles with respect to each other. The radar signal bounces off a wave facet from an ocean wave having a suitable wavelength. The reflected signal then bounces off a wave facet of a second ocean wave that travels at right angle with respect to the first wave before returning to the radar. This produces the so-called corner-reflector effect. Only the signal component that returns specularly toward the radar would have significant energy. The corner-reflector effect produces a characteristic spectral line that has an apparent Doppler frequency equal to  $2^{3/4}$  times the Bragg frequency ( $2^{3/4} f_B$ ). Second and higher order scattering of the radar signal by ocean waves gives rise to the sea-clutter continuum.

Second order sea-clutter spectral peaks are observed more often at the upper HF band because, at higher frequencies the wavelength is shorter, and it is easier to have a fully developed sea. Figure 10 shows a Doppler spectrum of the radar returns at a range of 24 km, as observed by the Cape Bonavista HFSWR at 15.77 MHz on the day of 6 October, 1994. This spectrum was computed using a 8192-point time series which yielded a Doppler resolution of about 0.012 Hz. The magnitudes of the receding and advancing Bragg lines were 64.6 dB and 49.6 dB,

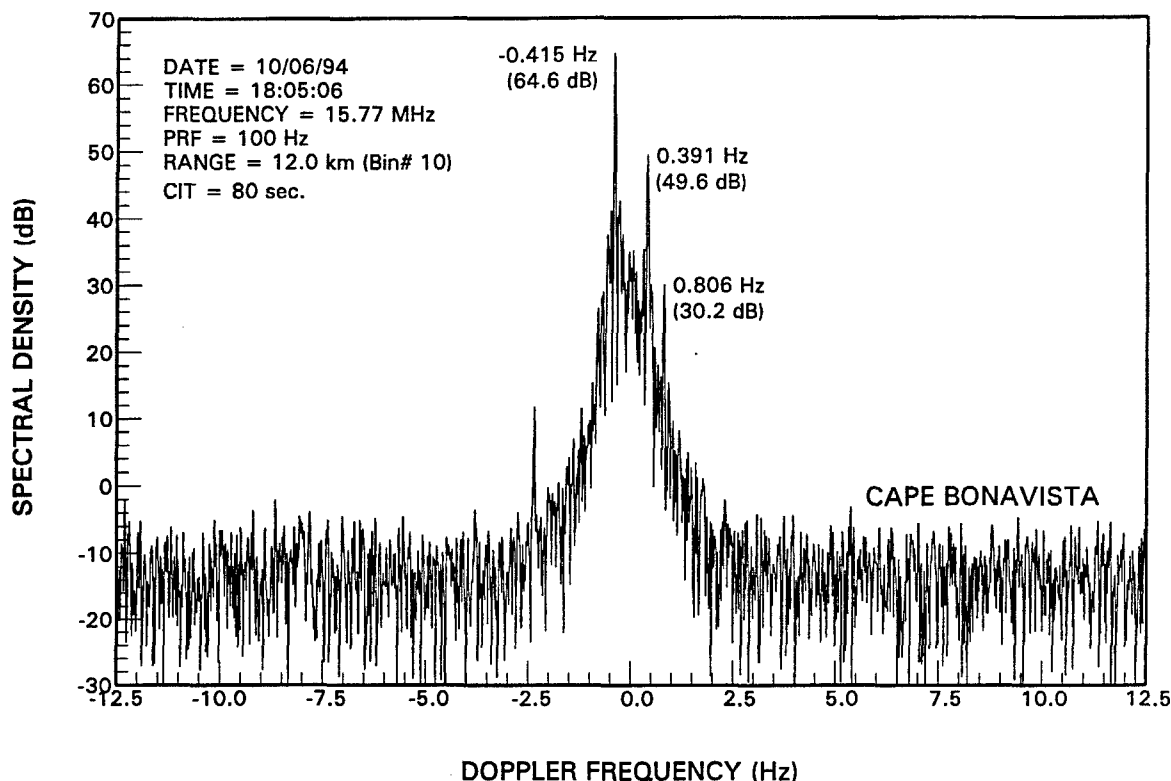


Figure 10. Typical sea-clutter spectrum from the Cape Bonavista HFSWR.

respectively. The spectrum is not smoothed because the Bragg lines are very narrow and they only occupy a few Doppler bins of the spectrum. The observed noise density was about -10 dB. This gives a Bragg-to-noise ratio of well over 75 dB. The Doppler frequency of the advancing and receding Bragg lines were 0.391 Hz and -0.415 Hz, respectively. From (1), the Bragg frequency is  $\pm 0.405$  Hz. Thus there was a Doppler offset of -0.012 Hz, or a radial velocity offset of 0.22 knots. According to the weather log, the wind on 6 October, 1994 was 16 knots @ 280° true. Hence, the wind was blowing along the boresight of the radar, and the velocity of the ocean surface current was about 0.22 knots.

Also observed in the spectrum of Figure 10 is a spectral line at 0.806 Hz. This corresponded (after correcting for the Doppler offset) to spectral line resulting from the fourth ( $2 f_B$ ) harmonic of the trochoidal gravity wave as described in theory. The spectral line at -2.356 Hz was determined to be caused by system artifacts. The spectral lines corresponding to the second harmonic and the corner-reflector effect (i.e., at  $f=2^{1/2}f_B$  and  $2^{3/4}f_B$ ) are often obscured because, in most cases, the Doppler resolution is insufficient to resolve them. These second order spectral lines have fairly large temporal fluctuation (over 10 dB).

The presence of sea clutter in the radar echoes reduces the probability of detection of aircraft with very low radial velocity significantly because of the requirement of a constant false alarm rate. Since the spectral extent of the sea clutter is small compared with that of the total Doppler domain of the radar, the effects of sea clutter on detection and tracking of aircraft is relatively minor. For example, in the spectrum of Figure 10, the sea-clutter energy has decreased to about the same level as the noise floor at Doppler frequencies greater than 2 Hz, which

corresponds to a radial velocity of 40 knots. This is at a relatively close range where the echo magnitude should be very large. At moderate ranges, the magnitude of the sea-clutter continuum should fall below the noise density at Doppler frequencies greater than 3 or 4 times the Bragg frequency.

### 3.1.2 Ionospheric reflection

At ranges greater than 60 or 70 km (depending on the radar frequency), the spectrum could also include components due to reflections from the ionosphere (ionospheric clutter). The ionospheric clutter can be seen in Figure 9 as the low-Doppler region between the ranges of 250 km and 300 km.

At low frequencies (below 100 kHz), the change in electron and ion densities within one wavelength is so great that the ionized gas region presents virtually an abrupt discontinuity in the medium. Under these circumstances, the reflection may be treated as in the case of the propagation of a wave across a dielectric interface.

At the high end of the high-frequency band, the wavelength is short compared with the thickness of the ionized-gas region and the ionization density changes only slightly in one wavelength. Under such conditions, the ionosphere may be treated as a dielectric with a continuously variable refractive index.

The ionospheric conditions for most HF radars fall between these two extremes. The ionosphere may be considered to comprise a number of thin but discrete layers, namely, the D, E, and F layers, in ascending order of altitude. These layers correspond to altitudes where the ionization density reaches a local maximum. For simplicity, it is customary to consider that each layer has a constant ionization density that differs from that of the adjacent layer. The incident wave will be partially refracted. The refracted wave penetrates to the second layer where it is partially reflected and partially refracted, and so on. In this case, the resultant reflected signal may be considered as the sum of reflections from various parts of the ionized layer. The propagation of radio waves via the ionosphere remains a very complicated process. As far as the HF surface-wave radar is concerned, echoes from the ionosphere are unwanted signals. It is important that these can be distinguished from legitimate targets. Hence, the important question is "What are the temporal, spectral and spatial behaviours of the echoes from the ionosphere?"

Figure 11a shows the range profile of the magnitude of the 0.15-Hz Doppler component from one of the receiver channels of the Cape Bonavista HFSWR. It can be seen that there was a sharp peak at about 316 km. Figure 11b shows the Doppler spectrum of the time series corresponding to that range. The main constituent of this spectrum was that of the ionospheric reflection. The multiple peaks in this spectrum was due to the time varying nature of the Doppler shift in the ionospheric reflection as can be seen in Figure 12.

Figure 12 shows the time series for the range bin corresponding to 316 km. The length of the time series was 1200 seconds. It can be seen that both the amplitude and Doppler frequency of the ionospheric echo varies slowly with time. The spectrum in Figure 11b was that of a nonlinear FM waveform, where the instantaneous Doppler extent was not very broad.

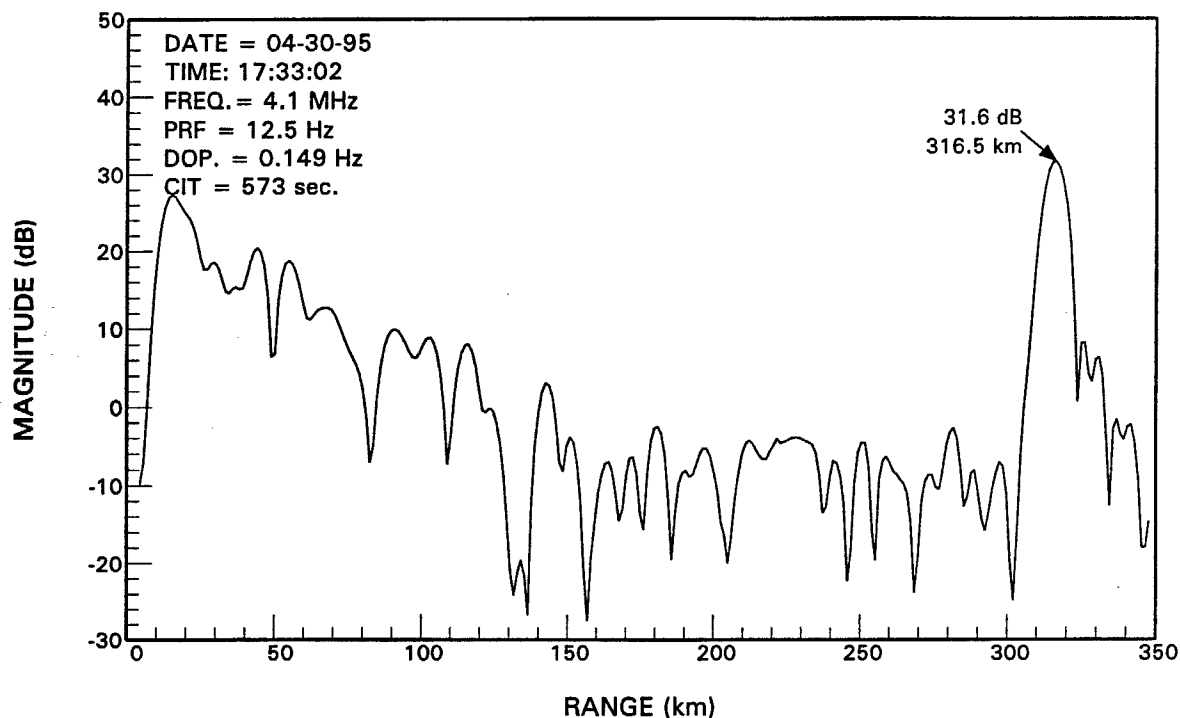


Figure 11a. Range profile of a Doppler component showing strong ionospheric reflection.

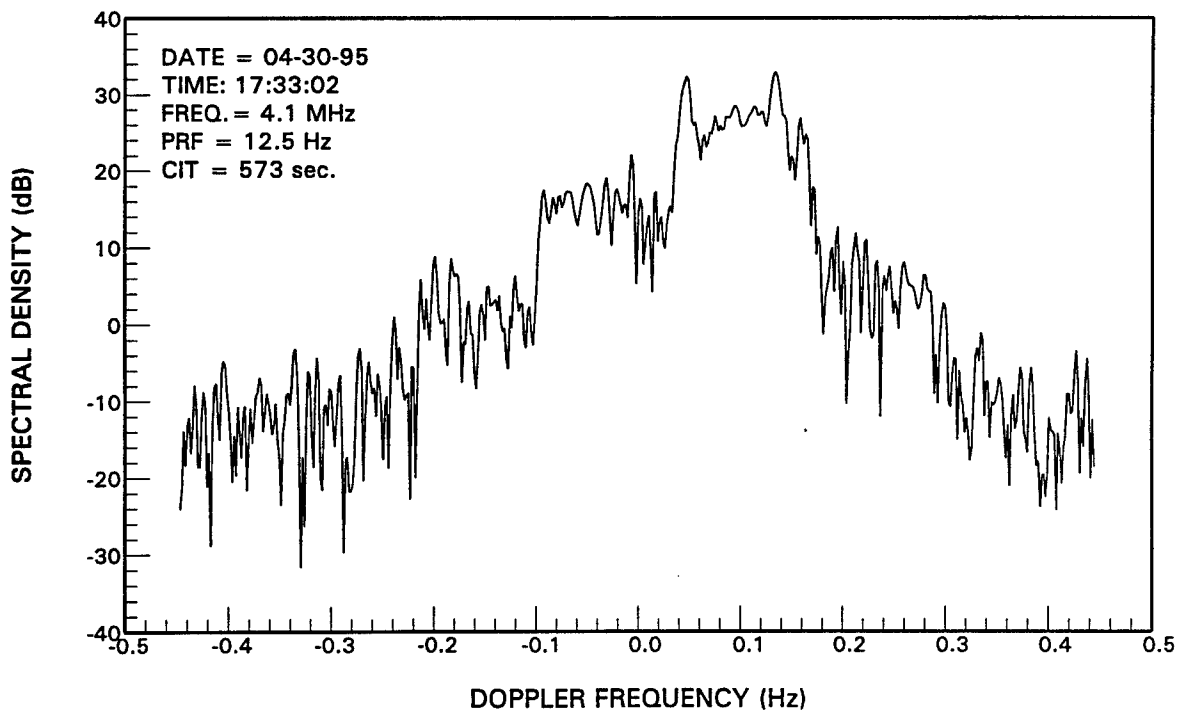


Figure 11b. Doppler spectrum of the time series from a range bin with strong ionospheric reflection.

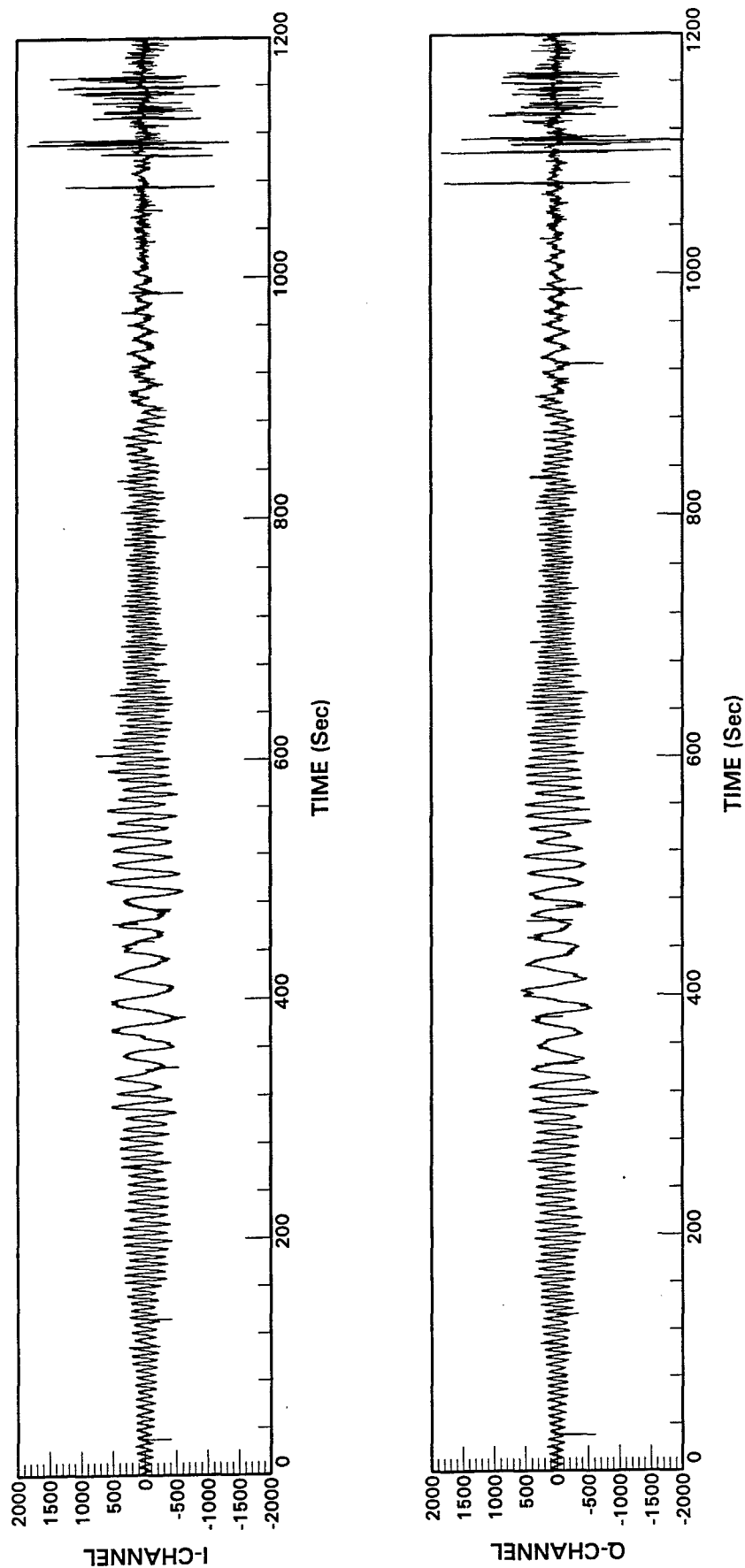


Figure 12. Waveform of the time series for a range with strong ionospheric reflection.



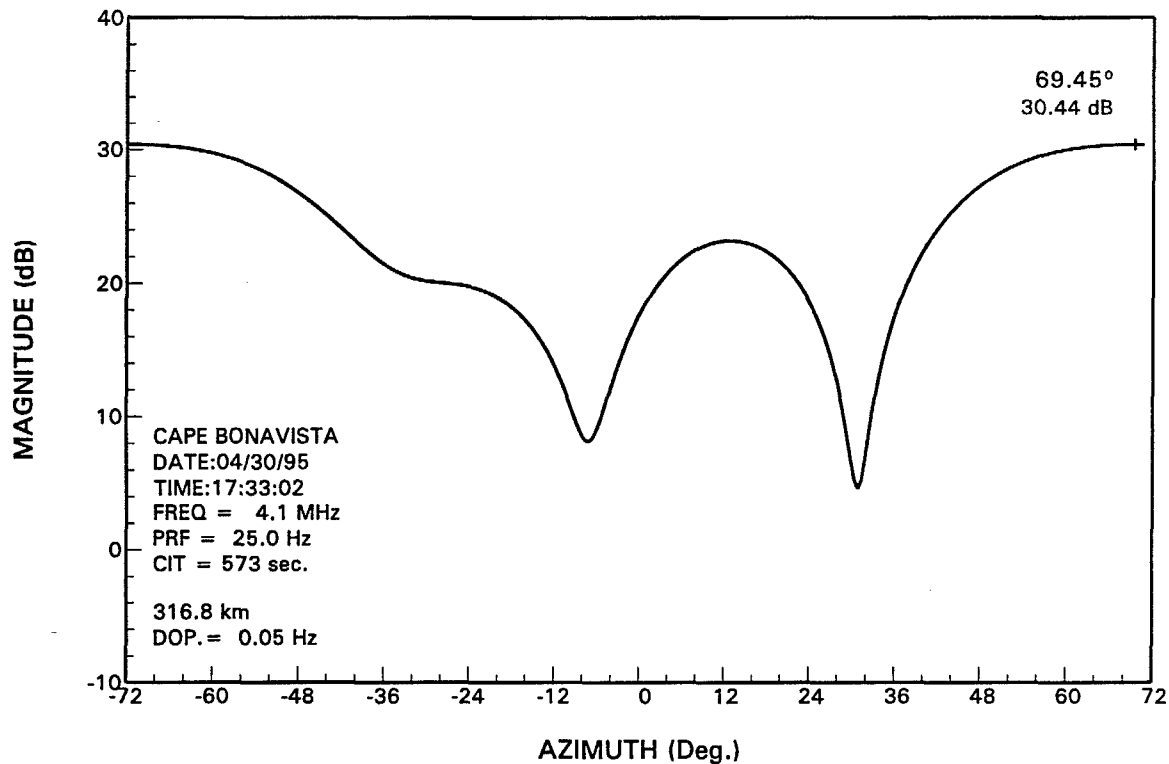


Figure 13. Ionospheric clutter strength as a function of bearing.

Some insights into the spatial aspect of the ionospheric reflection may be gained by examining the relative magnitude of its components at different azimuthal angles. Figure 13 shows the magnitude of the Doppler component from a range of approximately 312 km as a function of azimuthal angle. This experiment was carried out in May, 1995 using all 8 channels of the Cape Bonavista radar. It can be seen that the magnitude was the highest at about 69.45° off boresight. Another local maximum was located at approximately 12°.

The ionospheric reflection occupies a fairly broad Doppler extent around 0 Hz and would degrade ship detection at ranges affected. It is less of a problem in aircraft detection because of the much higher Doppler shift of a typical aircraft target.

### 3.1.3 Meteor and meteor trails.

Another type of ionospheric clutter arises from echoes of the radar signal off meteor trails. Meteoroids are small particles that orbit the sun whose trajectories intersect the earth's orbit. The radar cross section of the particles themselves are generally not large enough to be detected directly by HF radars. However, the ionized gas trail produced by particles entering the earth's atmosphere can produce large echoes that could degrade the radar's detection performance. An example of clutter arising from meteor trails may be seen in Figure 9 at ranges greater than 150 km. These echoes are characterized by a wide Doppler spread of relatively short duration.

This phenomenon occurs at height ranges of 80 to 140 km, with a typical trail being 25 km long. But, because the radar signal propagates at all elevation angles, meteor echoes could appear at any range between 100 km and 500 km. Generally, there are more meteor trails observed during the period between midnight and noon and substantially less during the afternoon hours. There is also a noticeable seasonal variation, with the summer meteor rate being approximately four times the winter rate. Meteoroid returns are characterized by a pulse like echo that rises rapidly to a maximum amplitude and decays over a few seconds.

Figure 14 shows the in-phase waveform of a time series corresponding to a range of about 188 km from Cape Race. The numbers appearing at the top of the plots denotes the index of the coherent integration time (CIT), the duration of which was about 27.8 seconds. The waveform consisted of the Bragg components (the sinusoidal waveform), and occasionally rapidly fluctuating waveforms of relatively short duration. For example, the signals in CIT Nos. 30, 79, 83 and 91 were probably those of meteor trails.

Figure 15 shows the spectrum of the time series for CIT No. 31. The echo from this meteor trail had a very broad Doppler extent, from about -2.5 Hz to over +0.6 Hz. This corresponded to velocities ranging from -125 knots to +30 knots. Its magnitude was more than 40 dB above the noise floor.

Meteor echoes will degrade the HFSWR's aircraft-detection performance by masking the echoes of aircraft targets having similar Doppler shifts. In addition, they could cause excessive false alarms because their spectral characteristics are very similar to those of a manoeuvring target. There are, however, some subtle differences that can be exploited to differentiate between echoes from meteor trails and legitimate aircraft targets. The first is that the magnitude of the echo from a meteor trail is usually very large compared with that of an aircraft at long ranges. Secondly, echoes from meteor trails generally do not form tracks that are consistent with the Doppler shift. That is, if the echo from a meteor trail has a certain dominant Doppler shift, echoes do not usually appear in the range bin that is consistent with a moving object with that Doppler shift in the next detection interval. These characteristics may be exploited by a tracker to eliminate meteor-trail echoes as legitimate targets.

#### **3.1.4 Co-channel communications interference**

Co-channel communications interference may come from local or remote sources. Local interfering signals are generally from known sources and interference can be avoided by choosing alternate frequencies. Interference from distant sources poses a more serious problem in that it is more random in time and frequency. At night, HF users tend to use the lower end (3 to 6 MHz) of the HF band, since the skip distance at these frequencies increases, thus enabling the signals to propagate over much greater distances. Consequently, the number of interfering signals increases at night and it may be very difficult to locate a clear channel at the lower end of the HF spectrum.

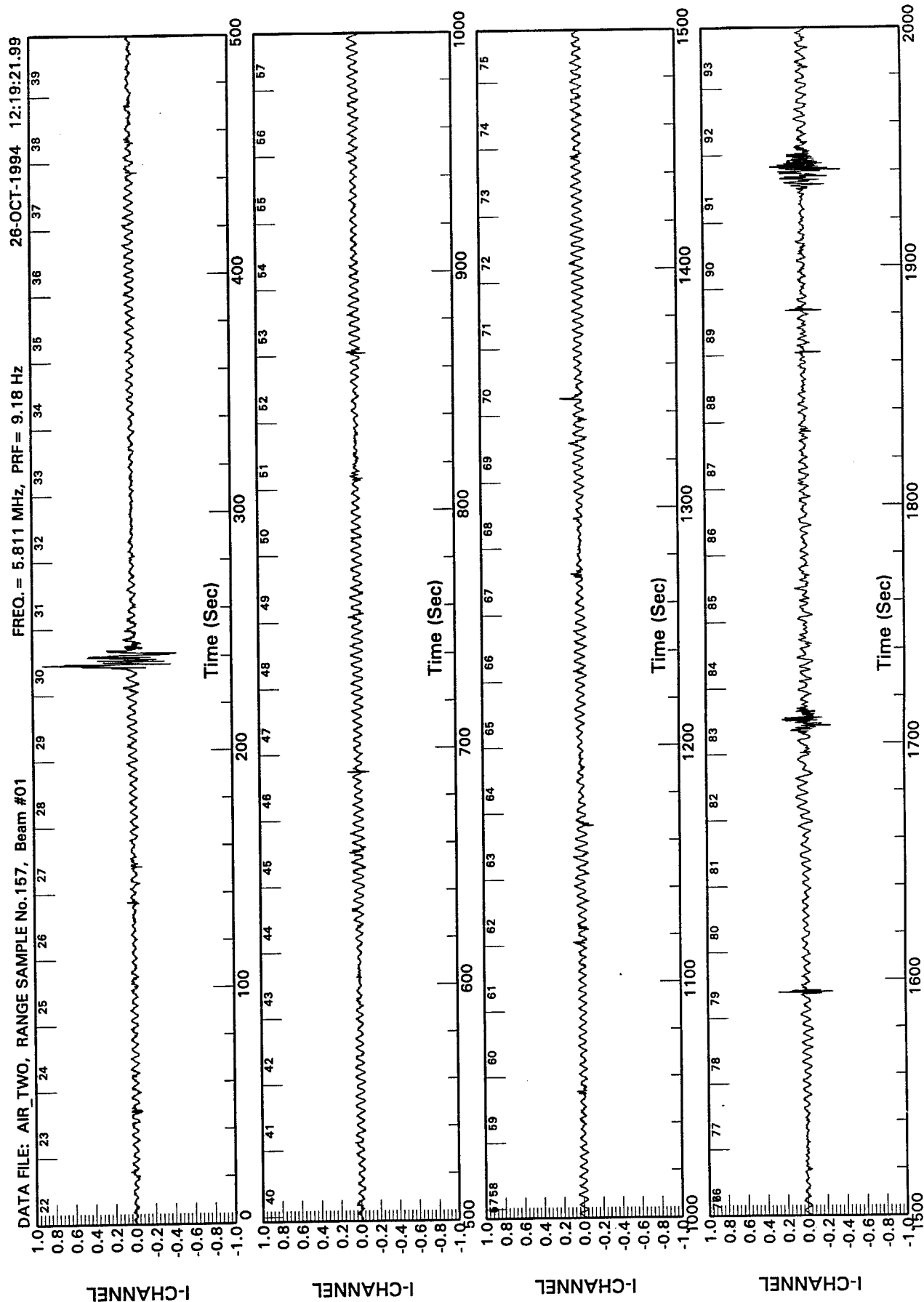


Figure 14. Waveform of the time series for a range with echoes from meteor trails.

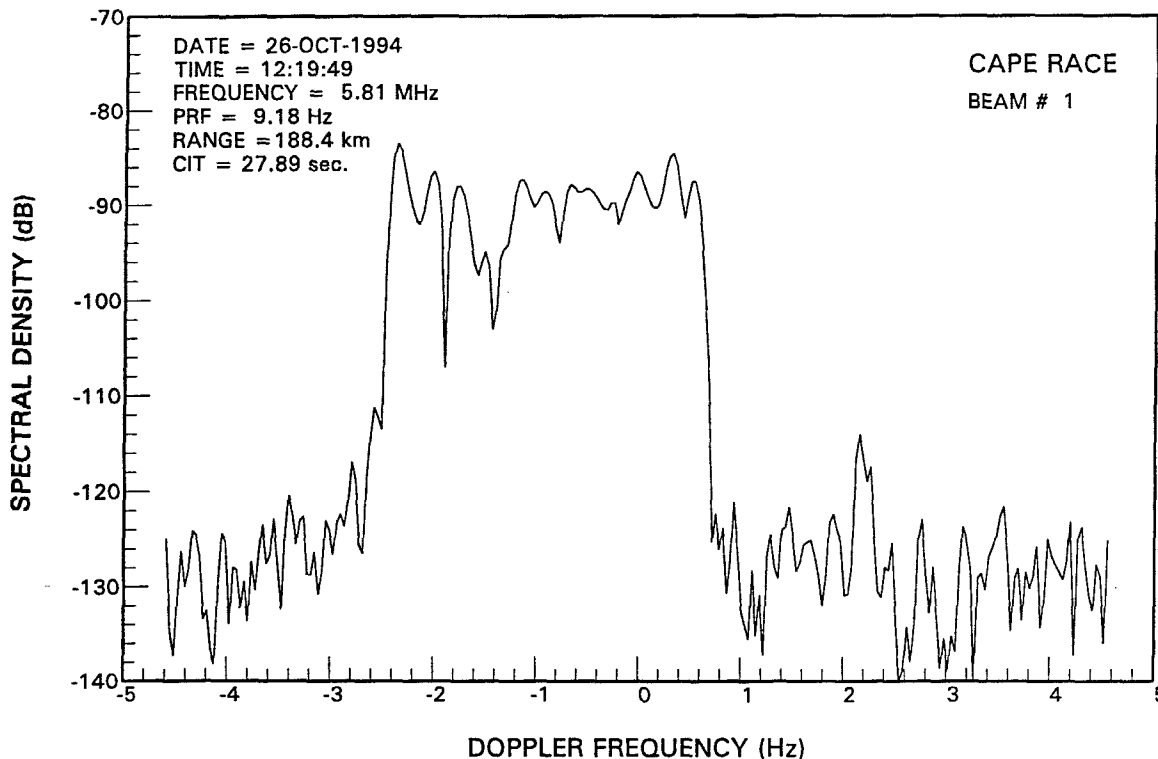


Figure 15. Spectrum of the time series containing echoes from meteor trails.

Some co-channel communications interference can be seen in Figure 9. This is the Doppler component that corresponds to a velocity around +200 knots. The important characteristics of co-channel communications interference is that it is generally range independent and highly directive, because communications signals originate from point sources. Since these interference signals are external to the radar and their duration is generally much longer than the radar's waveform, they will appear at all range cells.

Detection performance against targets with a Doppler that coincides with those of the interference would be degraded. Signal processing techniques [9-11] are available to mitigate the effects of these interferences.

### 3.1.5 Noise components

At higher Doppler frequencies, the main constituent of the HF radar spectrum is the noise component. Depending on various factors, the noise could be dominated by one or more of the following three sources: (a) galactic (b) atmospheric and (c) man-made. The International Radio Consultative Committee (CCIR) has compiled extensive data regarding these noise sources. These have been presented in two reports [12,13] the data of which are widely used in the HF community.

**(a) Atmospheric noise**

Atmospheric noise is the most complicated component to model because it is a function of frequency, location, season and time-of-day. The atmospheric radio noise is modeled by CCIR by means of Fourier series expansion whose coefficients were derived from measured data. The coefficients are keyed by geographic locations (latitude and longitude), season and time.

**(b) Galactic noise**

Galactic noise is dependent on frequency only, and its level may be approximated by the following relationship

$$N_o^G = 52 - 23 \log_{10}(f) \quad (2)$$

where  $N_o^G$  = galactic noise density in dB above kT;  
f = frequency in MHz.

At frequencies below 10 MHz, measurements indicated that the galactic noise is generally lower than the atmospheric and man-made components. Consequently, it is sufficient to consider atmospheric and man-made noise only for frequencies below 10 MHz.

**(c) Man-made noise**

Man-made noise is both frequency dependent and site-specific. The level of man-made noise is considerably lower in sparsely populated regions than in urban areas of the world. CCIR models man-made noise with a formula similar to that used to model galactic noise

$$N_o^M = \alpha_i - \beta_i \log_{10}(f) \quad (3)$$

where  $N_o^M$  = man-made noise density in dB above kT;  
 $\alpha_i$  and  $\beta_i$  are coefficients with index i designating the type of the site:

i = 1	for business locations
i = 2	for highways
i = 3	for residential areas
i = 4	for parks
i = 5	for rural areas
i = 6	for quiet rural areas.

**(d) CCIR estimates of the median noise levels at Cape Bonavista and Cape Race.**

Using the CCIR noise model, the median noise densities of the three types of external noise were calculated. Table 3 tabulates the overall (i.e. the combined galactic, atmospheric and man-made) noise densities for Cape Bonavista as a quiet rural site for frequencies of 4, 7 and 16 MHz.

**Table 3: Median values of the total external noise density at Cape Bonavista assuming a quiet rural site.**

	Winter			Summer		
Time Block	4 MHz	7 MHz	16 MHz	4 MHz	7 MHz	16 MHz
0000-0400	48.3	40.9	24.0	53.4	47.1	25.9
0400-0800	46.8	41.4	24.5	38.7	37.8	25.7
0800-1200	36.3	32.9	31.0	36.3	31.5	27.5
1200-1600	36.5	33.6	35.8	35.1	30.4	26.6
1600-2000	42.6	39.8	28.5	35.6	36.2	29.2
2000-2400	48.4	42.8	24.6	48.4	44.5	27.1
	Spring			Autumn		
	4 MHz	7 MHz	16 MHz	4 MHz	7 MHz	16 MHz
0000-0400	53.5	46.4	25.1	52.2	44.2	24.2
0400-0800	41.1	40.1	26.4	48.2	42.7	25.0
20800-1200	36.3	32.0	27.9	36.4	32.5	28.1
1200-1600	36.6	32.0	29.2	36.6	32.9	30.7
1600-2000	34.7	35.2	27.9	52.0	39.7	28.7
2000-2400	52.7	46.7	27.2	48.4	45.6	25.9

Table 4 tabulates the overall noise densities for Cape Race as a quiet rural site for a frequency of 6 MHz at which the radar was operating. In both Tables 3 and 4, the noise densities are specified as the parameter FA (noise factor) in dB above kT, where  $k = 1.38 \times 10^{-23}$  W/Hz/°K is the Boltzmann's constant and T is absolute temperature in °K. A typical value of T is 288°K giving a value of  $kT = 3.974 \times 10^{-21}$  W/Hz or -204 dBW/Hz.

These tables will be used in Section 4 to obtain the theoretical estimates of the radar performance from the HF surface-wave (HFSW) radar equation. The noise is assumed to have a white spectrum with a noise density  $N_0$  watts/Hz. Hence, the total noise power that passes through the receiver is equal to  $N_0 B$ , where B is the nominal receiver bandwidth.

Figure 16 compares a typical autumn noise spectrum measured at Cape Bonavista with that predicted by CCIR. Figure 16a plots the predicted galactic, atmospheric, man-made and the combined noise densities as a function of time (in four-hour time blocks). The scale on the left

**Table 4: Median values of the overall noise densities at Cape Race assuming a rural and a quiet rural site at 6 MHz.**

	Rural			
Time Block	Winter	Spring	Summer	Autumn
0000-0400	47.5	51.1	50.7	50.1
0400-0800	48.4	48.0	46.4	49.7
0800-1200	45.7	45.7	45.7	45.7
1200-1600	45.7	45.8	45.8	45.7
1600-2000	47.4	46.5	46.5	47.6
2000-2400	48.6	50.6	48.0	50.3
	Quiet Rural			
0000-0400	43.9	49.2	49.3	47.8
0400-0800	43.7	41.3	38.2	45.3
0800-1200	33.1	32.6	32.5	33.1
1200-1600	33.4	32.9	31.2	33.4
1600-2000	40.7	35.2	35.7	40.9
2000-2400	45.1	49.0	46.3	48.5

axis is in FA (dB above kT), and that on the right side is in dBW/Hz. Figure 16b shows the noise level measured with a Rhode and Schwartz ESH3 receiver using an RMS detector and a URV5 volt meter. Assuming that the receiver noise is much lower than the external noise, the measured noise level at mid day should correspond approximately to that of the galactic noise component since both the atmospheric and man-made noise components are lower. The measured results show good agreement with the predicted results, except at night time. A closer examination of the measured noise spectrum revealed that this apparent increase in noise floor was the result of interference and that there are gaps in the frequency band where the background level drops to the theoretical noise floor level.

### 3.1.6 Targets

Two targets can be observed in Figure 9. The first, an Air Force Challenger 601-3A, was a controlled target that appeared at a range of about 115 km. It was flying at an altitude of 200 ft at a velocity of -220 knots (away from the radar). The other was detected at a range of about 160 km with an apparent radial velocity of -198 knots. Although this seemed rather slow for a

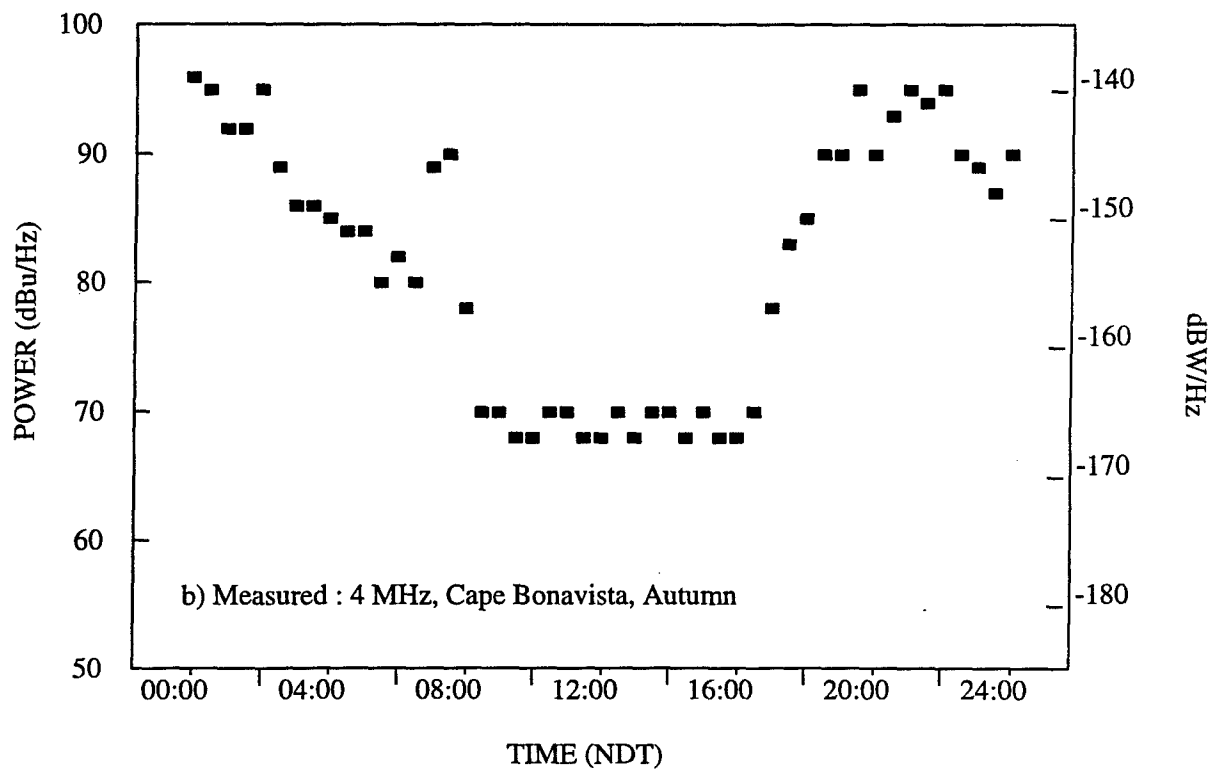
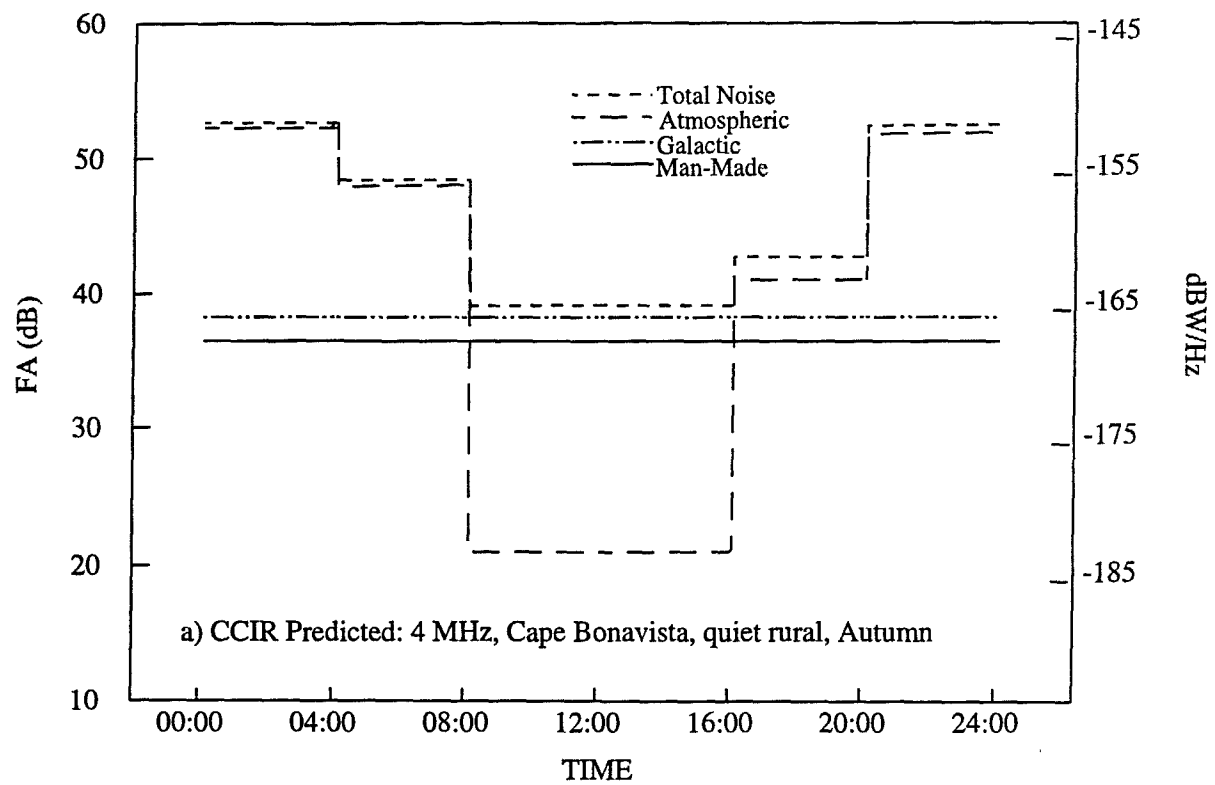


Figure 16. Comparison between CCIR predicted and measured noise level as a function of time.



jetliner, it was possible that the aircraft was travelling in a direction that was almost perpendicular to the radar beam. However, as we shall see in Section 4.4.1, this aircraft was actually approaching the radar at a much higher speed. It appeared to be moving away from the radar rather slowly because of the aliasing effect arising from the low WRF employed in the Cape Race radar.

#### (a) Constant velocity targets

For a target that travels at a constant velocity within a CIT interval, the echo is characterized by an impulse in the Doppler spectrum. Figure 17 shows the Doppler spectrum of a range cell in which a constant-velocity target was present. The radar operating frequency was 5.67 MHz with a WRF of 9.18 Hz. The target was the King-Air 200 flying at an altitude of 200 feet, travelling away from the Cape Race radar at a constant speed of about 203 knots. It can be seen that most of the target energy was confined to a few Doppler bins.

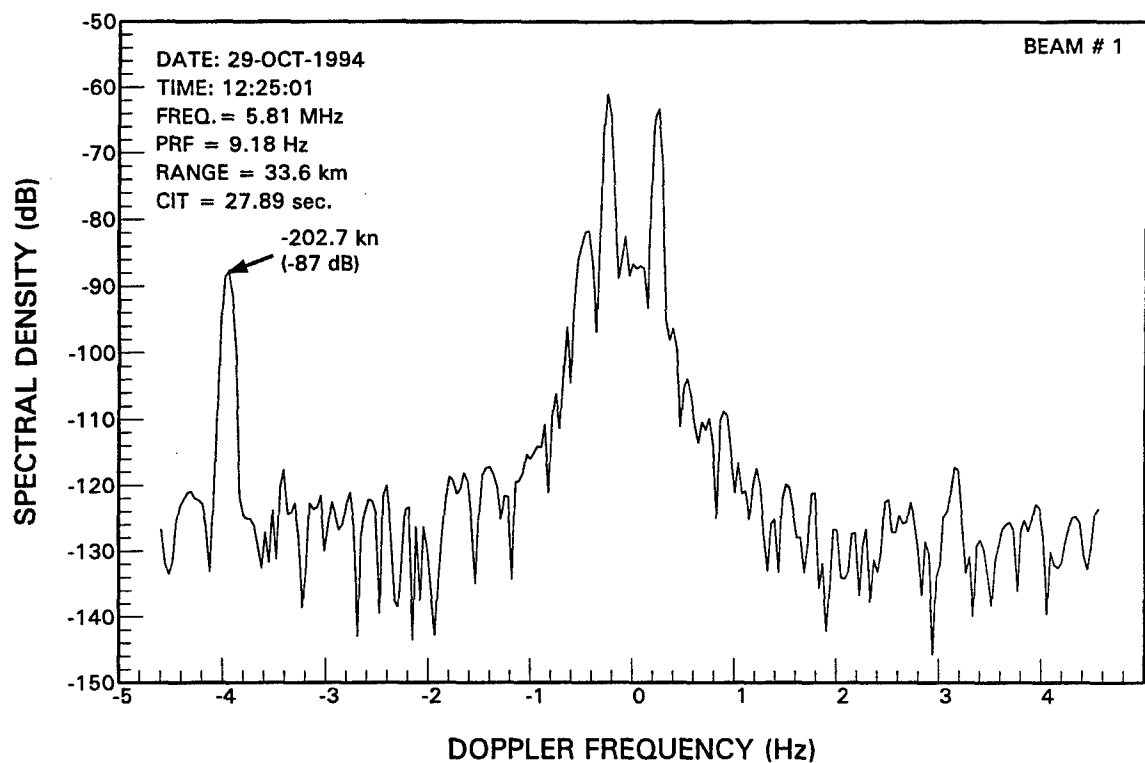


Figure 17. Typical spectrum of a range cell with constant velocity target.

#### (b) Manoeuvring targets

For a target that changes speed and/or heading within a coherent integration period, the echo is characterized by spectral components that covers a relatively wide Doppler region. This is due to the change in the target's radial velocity with respect to the radar. Figure 18 shows the resulting spectrum of the returns from a T-33 trainer at about 34 km from the Cape Race radar

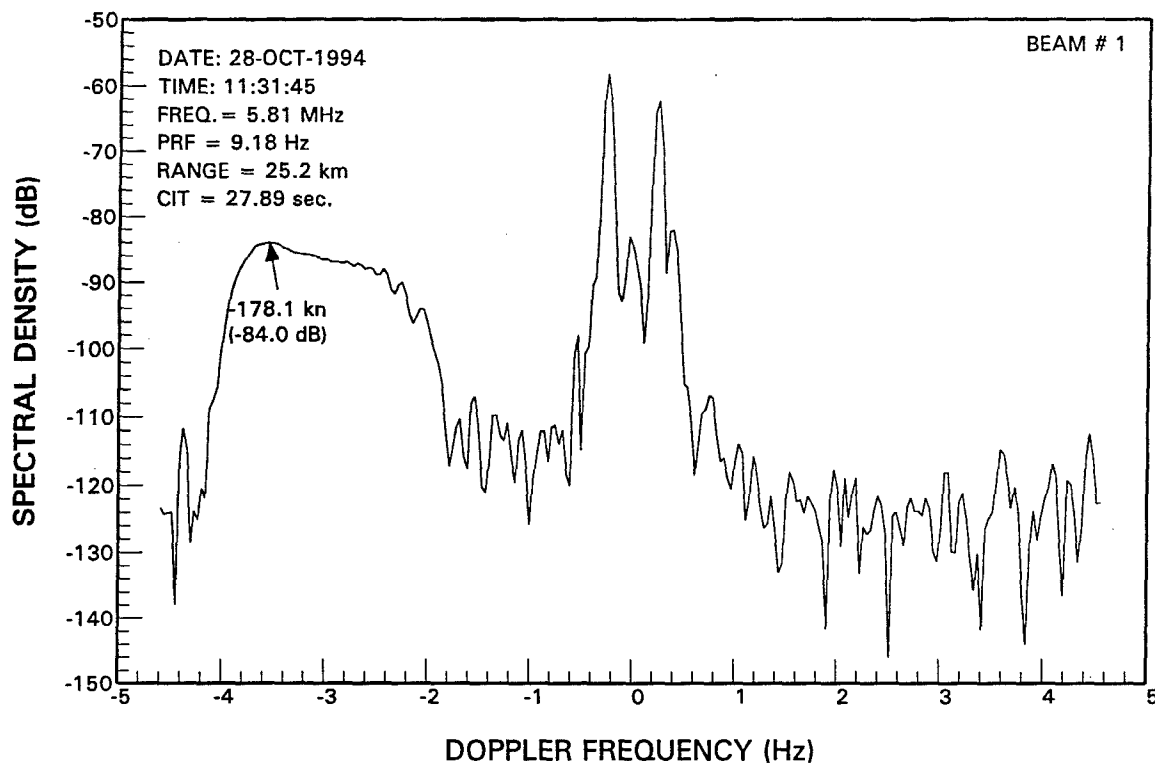


Figure 18. Spectrum of the returns from a T-33 during a banking manoeuvre.

Hz, corresponding to a radial velocity of -178.1 knots, it can be seen that the target's Doppler ranged from -4 Hz to -2 Hz. Special handling routines must be implemented in the detection undergoing a banking manoeuvre. Although a peak response was located at a Doppler of -3.55 Hz, corresponding to a radial velocity of -178.1 knots, it can be seen that the target's Doppler ranged from -4 Hz to -2 Hz. Special handling routines must be implemented in the detection algorithm to detect and track manoeuvring targets.

### 3.2 Signal processing.

For optimum target-detection performance, the radar signal must be processed to enhance the SNR. Here the term "noise" is generalized to include clutter and interference. The radar returns are first sorted into range bins by range gating. Successive returns corresponding to the same range bin form a time series. This time series is then processed to sort the signal components in terms of velocity. The azimuthal information of the returned echo is obtained by determining the angle of arrival of each Doppler component, and then comparing the result with a threshold setting that satisfies a certain probability of false alarm ( $P_{fa}$ ) criterion. The signal processing techniques used to sort the returns in terms of velocity and to determine the angle of arrival are Doppler processing and digital beamforming, respectively. These were carried out using conventional the fast Fourier transform (FFT) technique. Before discussing signal processing and beamforming, it is informative to revisit the surface-wave radar equation because it will be used to compare the experimental results with theoretical predictions.

### 3.2.1 The surface-wave radar equation

The received power from a target for a monostatic surface-wave radar is defined as

$$P_r = \frac{P_t G_t G_r \sigma A^4 \lambda^2}{(4\pi)^3 R^4 L_s} \quad (4)$$

where

$P_r$  = Receive peak power  
 $P_t$  = Transmit peak power  
 $G_t$  = Transmit antenna gain  
 $G_r$  = Receive antenna gain  
 $\sigma$  = Target radar-cross-section

$\lambda$  = Radar wavelength

$R$  = Target range

$L_s$  = System loss

$A$  = Norton surface-wave field attenuation factor [14] at Range  $R$  ( $A \leq 1$ ).

It is customary in HF radar work to write the radar equation in terms of SNR. The received echo of a transmitted pulse from a target at a given range must be processed by a matched filter (or an approximation of it) to enhance the SNR. For a simple rectangular pulse wave form, the matched filter is an integrate-and-dump (I&D) filter. The received waveform after each pulse transmission is integrated over a length of time equal to the transmit pulse length,  $\tau$ . At the end of the integration period a sample is taken from the I&D filter. The radar equation in terms of SNR is

$$\frac{S}{N} = \frac{P_t G_t G_r \sigma A^4 \lambda^2}{(4\pi)^3 R^4 L_s N_0 B} \quad (5)$$

where  $N_0$  is the noise density and  $B$  is the receiver bandwidth ( $=1/\tau$ ).

For a receiver that is matched to the transmit waveform, the bandwidth may be approximated by the reciprocal of the transmit pulse length (i.e.  $B = 1/\tau$ ). The combined unit for all the parameters in (5) excluding  $N_0$  is in joules. Hence, the SNR may be interpreted as the signal-energy to noise-density ratio for a single pulse.

$$\left(\frac{S}{N}\right)_{SP} = \frac{P_t \tau G_t G_r \sigma \lambda^2 A^4}{(4\pi)^3 R^4 L_s N_0} \quad (6)$$

where subscript "SP" denotes the single pulse case.

Since coherent integration (or Doppler processing) is always employed in HFSWRs, it is more convenient to write the HFSW radar equation in terms of the SNR after the returns from the same range bin have been coherently integrated over a number of pulses. For a coherent integration time (CIT) of  $T_i$  seconds, there are

$$N = T_i f_p \quad (7)$$

pulses, where  $f_p$  is the radar's PRF.

Assuming that the target echo is present in the returns of all  $N$  pulses, the coherent integration over  $N$  pulses will enhance the SNR by a factor of  $N$  [15]. Hence, the resulting SNR over  $N$  pulses is given by

$$\frac{S}{N} = \frac{P_t f_p \tau G_t G_r A^4 T_i \sigma \lambda^2}{(4\pi)^3 R^4 L_s N_0} \quad (8)$$

Noting that the product  $f_p \tau$  is the duty cycle of the radar, the SNR over  $N$  pulses may be expressed in terms of the average transmit power

$$\frac{S}{N} = \frac{P_{av} G_t G_r \sigma T_i A^4 \lambda^2}{(4\pi)^3 R^4 L_s N_0} \quad (9)$$

where  $P_{av} = P_t f_p \tau$  is the average transmit power.

Equation (9) is a function of the Norton surface-wave field attenuation factor,  $A$ , which had been computed by Norton for the case of a smooth conducting surface. For surface waves propagating over a rough sea, however, there are additional losses due to the increased surface roughness. Barrick [16] uses a perturbation technique, by which the additional propagation loss due to the increased sea-surface roughness is evaluated based on the concept of effective surface impedance. He further combines the surface-wave attenuation loss with the basic propagation loss due to the spherical dispersion of a signal into a single quantity, called the total (one-way) propagation loss

$$L_T = \left( \frac{4\pi R}{\lambda A'} \right)^2 \quad (10)$$

where  $\lambda$  is the radar's wavelength,  $R$  is the range and  $A'$  is the modified surface-wave attenuation that includes the sea-state loss. The quantity  $(4\pi R/\lambda)^2$  in (10) may be identified as the basic free space propagation loss due to the spherical dispersion of a signal.

Substituting (10) into (9), the radar equation now becomes

$$\frac{S}{N} = \frac{P_{av} G_t G_r \sigma T_i 4\pi}{L_T^2 L_s \lambda^2 N_o} \quad (11)$$

Since coherent integration concentrates the (constant velocity) target energy into a particular Doppler bin, the value of  $N_o$  refers to the power density of the combined (clutter + noise + interference) process at the target Doppler frequency. If the Doppler frequency of the target is far removed from the sea-clutter dominated region,  $N_o$  is the external noise density. If the Doppler frequency of the target falls within the sea-clutter region, then  $N_o$  is the density of the combined process of sea clutter and external noise (assuming no interference).

Because Barrick's surface-wave propagation loss data are widely used in the HF surface-wave radar community, one must exercise caution in specifying the gain of the antennas and radar cross section of targets in the context of HF surface-wave radar equation. There are two effects that must be taken into account in the determination of the proper values of  $G_t$ ,  $G_r$ , and  $\sigma$  used in (11). The first is the ground-plane effect, which refers to the doubling of the field intensity or quadrupling of the power flux density when an antenna is radiating over a perfectly conducting ground plane. This results in a 6 dB increase in the antenna gain. The second effect is the ground-proximity effect, which refers to the reduction in the antenna gain (or RCS) due to mutual coupling of the antenna (or target) and its image as its distance from the conducting surface decreases. A reduction of 3 dB in gain (or 6 dB in the target RCS) will result when the antenna (or the target) is situated on the conducting surface. Detailed discussions of these two effects may be found in [17,18].

Using Barrick's formulation, Rotheram [19] developed a computer program, called GRWAVE, for the computation of the surface-wave propagation loss. This program computes the one-way propagation loss between two antennas, both situated above the sea surface and separated by a distance  $R$ . The computed propagation loss is a function of the transmit and receive antenna heights, the range  $R$  and wind speed. The ground-plane effect applies to the transmit antenna only because it changes the electric field of the transmit antenna. The increase in the transmit antenna gain due to the presence of the ground-plane is accounted for by reducing the propagation loss by 6 dB. That is, the total propagation loss computed from GRWAVE approaches asymptotically that represented by

$$L_T = \left( \frac{2\pi R}{A'\lambda} \right)^2 \quad (12)$$

The ground-proximity effect applies to both the transmit and receive antennas. The GRWAVE program accounts for the ground-proximity effect by modelling the height dependent antenna gain as the ratio between the free-space gain and a quantity called the height factor [19], defined as

$$F_h = 1 + \frac{3}{(2k_0 h)^2} \left[ \frac{\sin(2k_0 h)}{2k_0 h} - \cos(2k_0 h) \right] \quad (13)$$

where  $k_0 = 2\pi/\lambda$  is the radar's wave number and  $h$  is the antenna height.

That is, the effective transmit and receive antenna gains are

$$G_t' = \frac{G_t}{F_h^t} \quad (14)$$

and

$$G_r' = \frac{G_r}{F_h^r} \quad (15)$$

respectively, where  $G_t$  and  $G_r$  are the free-space gains of the transmit and receive antennas, respectively.

As the antenna height approaches zero, the height factor approaches the value of 2. This means that when the antenna is situated on the conducting surface, its gain is reduced by 3 dB from its free-space value. This reduction in the antenna gain is accounted for in GRWAVE by increasing the propagation loss by an amount proportional to the height factors. For example, if both the transmit and receive antennas are situated on the conducting surface, the propagation loss computed from GRWAVE would be 6 dB higher than the value for the case where both antennas are at least one wavelength above the conducting surface.

A target acts as a receive antenna when it intercepts the signal radiated by the transmit antenna. It acts as a transmit antenna when it re-radiates the intercepted signal energy back to the radar. Consequently, there will be a maximum of 6 dB reduction in the target's radar cross section when the target is situated on the conducting surface compared with the value in free space.

With this background, it is easy to see that when one uses the propagation loss computed by the GRWAVE program directly, one must specify the antenna gains and radar cross section in terms of free-space values because both the ground-plane effect and the ground-proximity effect are accounted for.

Various researchers have different preferences with regard to the question of whether or not to consider the ground-plane and ground-proximity effects as propagation properties, as Barrick does. The argument against it is that sometimes it may not be practical to specify a free space value for the antenna gain and RCS. For example, it is not clear whether using the free-

space RCS of a ship would be appropriate because, in this case, the ocean surface cannot be separated from the ship.

Furthermore, from a practical point of view, confusion could arise for users of HFSWR simulation programs with the GRWAVE program embedded in the software because the user may not be aware of how the simulation program defines the antenna gain and radar cross section. It is preferable that the ground-plane and ground-proximity effects are taken out of the surface-wave propagation loss calculation, and the user enters the values of the antenna gain and RCS as they are in the actual situation. In other words, the surface-wave propagation loss should be computed as in (10), and the user must ensure that the ground-plane and ground-proximity effects are accounted for in the antenna-gain and RCS values when they use the simulation program.

The HFSWR simulation software [20] implemented at DREO uses the GRWAVE program to compute the surface-wave propagation loss. It was modified so that the ground-plane and ground-proximity effects were taken out of the GRWAVE calculation. The user, however, has the option of specifying the antenna gains either in free-space or actual values. If the input antenna gains are free-space values, the program adds 6 dB to them to account for the ground-plane effect and adjust the gain according to the height factor. If the input antenna gains are actual values, the program will use them directly.

There is an important point that is often overlooked in the application of the HF surface-wave radar equation, that is, the proper value of the receive antenna gain under the external-noise-limited conditions. Most HFSWRs employ an array of vertically polarized antenna elements. The elemental pattern is generally very broad in the azimuthal plane and the peak gain is at zero elevation. If the level of the external noise, which comprises the Galactic, atmospheric and man-made, is substantially higher than the receiver noise, then the element gain of the receive antenna would have no effect on the system's SNR, unless the gain is so low that the receiver noise becomes dominant. Consequently, for an HFSWR that is external-noise limited, only the array gain should be used in the radar equation. In addition, since the ground-proximity effect affects only the element gain, its effect should also be taken out.

### 3.2.2 Doppler processing

Doppler processing is performed using the fast Fourier transform (FFT). An important parameter to be determined is the size of the FFT used. The appropriate size of the FFT is determined nominally by the length of the time series containing the target. Since a moving target will remain in a particular resolution cell in a finite amount of time only, the size of the FFT is determined by the amount of time required for a target with an expected maximum speed to traverse a range resolution cell. Let  $v_{\max}$  be the maximum expected speed of the target. The time for this target to transit the range cell is equal to  $(c\tau/2)/v_{\max}$ ; and the number of waveforms transmitted during this time is  $(c\tau/2)/v_{\max} \times \text{WRF}$ . Hence, the size of the FFT to be used should be equal to or slightly greater than  $L$  which is given by

$$L = \frac{c\tau}{2v_{\max}} \text{WRF} \quad (16)$$

where  $c$  is the speed of light,  $\tau$  is the radar's pulse length and WRF is the radar's waveform repetition frequency. For pulse-compression waveforms,  $\tau$  is the compressed pulse length.

For the trials described in this report, the maximum radial speed of the aircraft was about 230 knots or 103 m/s. For the Cape Bonavista radar, the pulse length was  $\tau = 50 \mu\text{sec}$  and the WRF was 100 Hz. Hence,  $L = 7500 \times 100/103 \approx 7281$ , and appropriate FFT sizes would be 4096 or 8192. For the Cape Race radar, the compressed pulse length was  $\tau = 8 \mu\text{sec}$  corresponding to a range cell size of 1.2 km. The WRF for the Cape Race radar was approximately 9.01 Hz. Hence,  $L = 1200 \times 9.01/103 \approx 105$ , and an appropriate FFT size was 128.

In practice, because of the finite receiver bandwidth, the extent of the target echo is generally greater than the extent of the resolution cell. In addition, because data windows are used to suppress the Doppler sidelobes, a larger FFT size may be used without any appreciable reduction in SNR. We chose FFT sizes of 4096 and 256 for the Cape Bonavista and Cape Race data, respectively. A data window was applied to the time series before FFT to suppress the Doppler sidelobes.

For the Cape Bonavista data, the time series were supplied as fixed length files on 8 mm tape cassettes. Each time series contains the returns from one of 160 range samples of 24000 consecutive pulses (4 minutes). We divided each time series into six parts, each comprising the returns from 4000 consecutive pulses. Each of these segmented time series was processed using a 4096-pt FFT. For the Cape Race data, the time series represents the returns from 256 range samples of about 30000 consecutive FM sweeps (about 45 minutes). These time series are divided into blocks of 256 pulses and processed with a 256-Pt FFT.

The nominal Doppler resolution of the FFT of a given size is obtained by dividing the sampling frequency of the time series by the size of the FFT:

$$\Delta f = \frac{\text{WRF}}{N} \quad (17)$$

The spectra obtained from the Cape Bonavista data had a nominal Doppler resolution of 0.0244 Hz. However, since a Blackman window was used, the Doppler main lobe actually occupied slightly more than two Doppler bins. Since the eight receiver channel had already been combined in hardware, there was only one-beam. Hence, there was no need to store the complex FFT results for subsequent digital beam-forming operations, and only the magnitudes of the spectra were stored. Since the Doppler domain of the Cape Bonavista was significantly greater (100 Hz) than the maximum expected Doppler targets, the spectral components beyond the maximum expected Doppler were discarded in order to conserve storage.



The Cape Race data were processed and stored in a similar manner. However, in this case, the ten receiver channels were individually sampled, and these could be used to synthesize beams pointing at different look directions. Hence, the complex FFT results for each range were stored on disk files. These files were used in subsequent beam-forming operations.

### 3.2.3 Digital beam forming with a multi-element receive array.

To enhance the SNR of potential targets further before detection, digital beam forming is performed. This is accomplished by using a spatial FFT. The complex samples of each Doppler component from all ten receiver channels were placed in a 128-point buffer and padded with zeros. The non-zero samples in the buffer were then multiplied by a data window and an 128-point FFT was performed.

$$F_k = \sum_{i=0}^{N-1} x_i w_i e^{-j \frac{2\pi i k}{N}} \quad (18)$$

where  $\{x_i, i=1,2,,10\}$  are the complex Doppler samples from the receive channels, and  $x_i = 0$  for  $i > 10$ ;  $\{w_i, i=1,2,,10\}$  are the antenna weighting coefficients; and  $N = 128$ .

The bearing of a potential target is obtained by substituting the FFT index  $k$  at which the azimuthal response is maximum into the following formulas:

$$\theta = \sin^{-1} \left[ \frac{k\lambda}{Nd} \right] \quad (19)$$

for  $k \leq N/2$

and

$$\theta = \sin^{-1} \left[ \frac{(k-N)\lambda}{Nd} \right] \quad (20)$$

for  $k > N/2$ .

### 3.3 Detection and tracking.

Detection and tracking of aircraft in HFSWR differ considerably from those in microwave radars. For microwave radars, the Doppler information of the target cannot always be extracted from within a single dwell. For example, for non-coherent radars, Doppler information is not available. Even in some coherent microwave radars, only moving target indicator (MTI) filters are used. As a result, the Doppler information is discarded. To prevent excessive false alarms, a detection threshold must be established which is a function of the required probability of false alarm and the statistics of the background noise process. The statistical parameters are usually

the mean and variance of the background noise process when there is no target present. Microwave radars usually employ time-averaging or range-averaging schemes to obtain these estimates.

High frequency surface-wave radars, on the other hand, rely on long coherent integration to increase the SNR to a sufficiently high level for detection. The integration time for aircraft at below-the-horizon ranges is measured in terms of tens of seconds. The long integration time provides a relatively high resolution in the Doppler domain, and Doppler information can be estimated accurately within a single CIT interval. To establish a detection threshold, HFSWRs usually employ Doppler averaging, coupled with some range averaging, to obtain the required statistical parameters. Because of the long time between dwells (or coherent integration periods), time-averaging is seldom employed. In Doppler averaging, one assumes that the random processes representing the returns from a finite number of neighbouring Doppler bins are identically and independently distributed. This assumption is valid for targets with sufficiently high radial velocities, such that the target Doppler shift is well removed from the sea-clutter region.

Because of the long coherent integration time, the aircraft could undergo significant changes in velocity and heading. This means that the energy of the echo is spread both in Doppler and azimuth. In contrast, the dwell time (the time in which the target is illuminated by the radar) of a typical microwave radar for target detections is measured in terms of tens of milliseconds. The Doppler spread of a manoeuvring target within several tens of milliseconds does not occupy a significant portion of the radar's Doppler domain. In Section 3.1.6b (Figure 18) we observed the Doppler spectrum of a T-33 trainer in a banking manoeuvre captured by the Cape Race HFSWR. The target energy spread over a Doppler region that occupied over 25% of the radar's total Doppler domain.

This large Doppler spread has two consequences. The first is that it complicates the detection process. The second is that special handling is required for tracking of manoeuvring targets.

### **3.3.1 Detection algorithm.**

The detection algorithm for aircraft must be able to discriminate both constant-velocity as well as manoeuvring targets against background noise and interference, such as ionospheric echoes. In Section 3.1, the spectral characteristics of the various interference components were examined. In developing the detection algorithm we shall make use of these observations.

For ranges less than 100 km, there is relatively little ionospheric clutter. There, the sea clutter is the main concern. After Doppler processing and digital beamforming, the time series of the returned echoes are transformed into a surface in range, Doppler and azimuth. The necessary condition for a target is that the returns must be a local maximum on this surface and that the magnitude of the target exceeds a threshold setting.

To determine the detection threshold, we made the following assumptions:

- (a) detection of aircraft targets with a radial velocity within the sea-clutter dominated region will not be performed.
- (b) the Doppler samples outside the sea-clutter dominated regions have exponential statistics, and effects of external interference on the threshold setting were not considered.
- (c) false alarms arising from the presence of external interference within a dwell can be handled by the tracker.
- (d) no more than one aircraft target can be present in range-azimuth cell.

The exponential density function describes the statistics of the squared magnitude of a complex random variable, where both the real and imaginary parts are characterized by the same zero-mean Gaussian process. The detection process is divided into two stages. The first handles constant velocity targets, and the second handles probable manoeuvring targets.

**(i) Constant-velocity targets.**

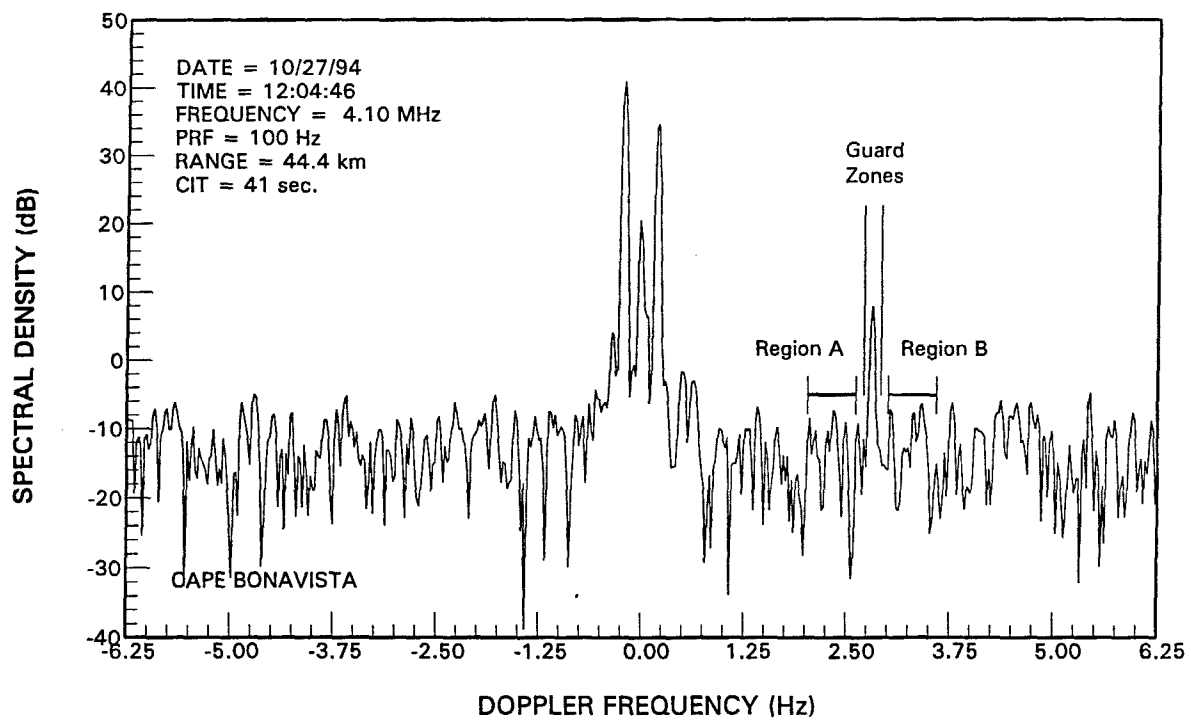
For constant velocity targets, the received target energy is concentrated in one or two Doppler bins, corresponding to the target's radial velocity. Regions A and B are defined on each side of the Doppler bin, as illustrated in Figure 19a. Assuming that the index of the Doppler bin of interest is  $k$ , region A is defined as the group of  $L$  Doppler bins, starting from the  $(k-M)$ th bin and ends at the  $(k-M-L+1)$ th bin. Similarly, region B is defined as the group of  $L$  Doppler bins starting from the  $(k+M)$ th bin and ending at the  $(k+M+L-1)$ th bin. A sample mean estimate for Doppler bin  $k$  when there is no target present is obtained by:

$$\langle y \rangle = \frac{1}{2L} \left[ \sum_{i=L_1}^{L_2} y^i + \sum_{i=L_3}^{L_4} y^i \right] \quad (21)$$

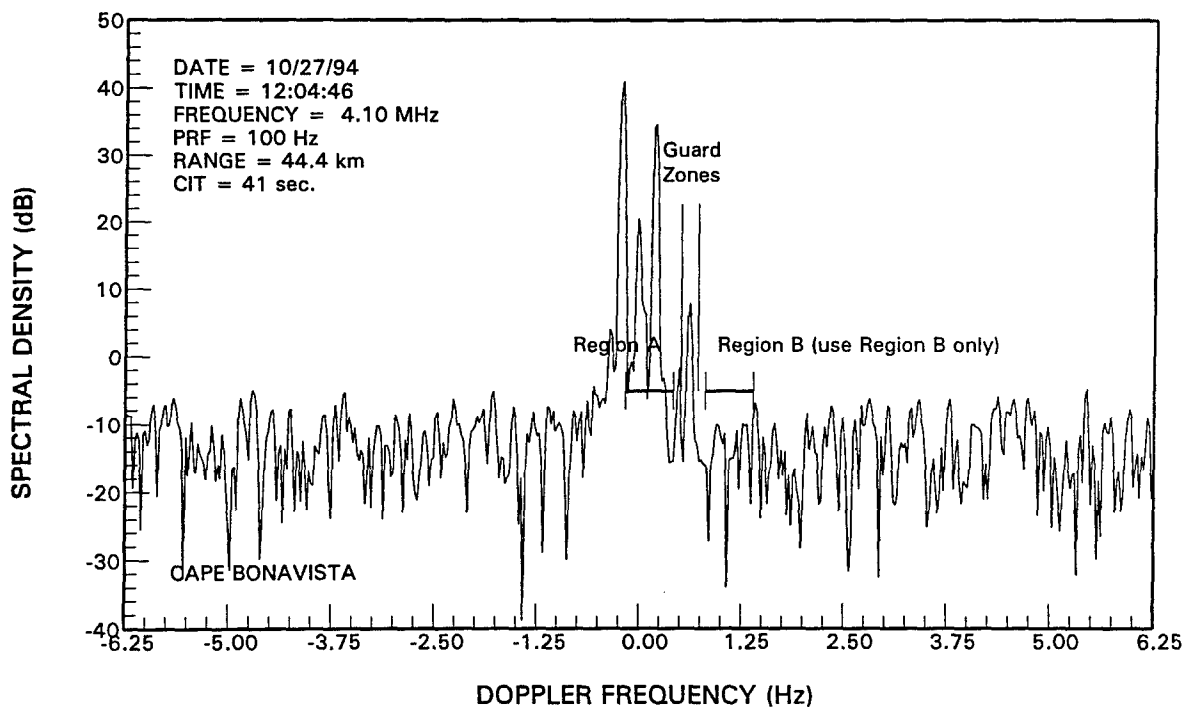
where  $L_1 = k-M$ ,  $L_2 = k-M-L+1$ ,  $L_3 = k+M$  and  $L_4 = k+M+L-1$ .

The  $M$  Doppler bins separating bin  $k$  from regions A or B are called the guard zones, the purpose of which is to prevent a potential target in bin  $k$  from corrupting the sample mean estimate.

For Doppler bins that are close to the sea-clutter dominated region, the sample mean is computed using Doppler samples in either region A or B, depending on which region is inside the sea-clutter region. For illustration purposes, the Doppler samples of Figure 19a in the region between 0.5 Hz and 0.75 Hz were interchanged with those between 2.6 Hz and 2.85 Hz, so that the target's Doppler would be close to the sea-clutter dominated region. This was necessary since no actual target data fitting the above description were available from this trial. This is shown in Figure 19b. If this were the actual target, then the sample mean would be computed from samples in Region B only.



(a) Case where target Doppler is far removed from sea clutter.



(b) Case where target Doppler is close to sea clutter.

Figure 19. Regions for determining the threshold in a Doppler-averaging CFAR.

Having computed the sample mean estimate, the next step is to determine the detection threshold. The threshold is computed by:

$$V_T = \Delta V + \langle y \rangle_{dB} \quad (22)$$

where  $\langle y \rangle_{dB}$  is the sample mean expressed in dB, and  $\Delta V$  is a quantity in dB to be added to the sample mean estimate. The value of  $\Delta V$  is determined nominally by the required  $P_{fa}$ :

$$\Delta V \approx 10 \log_{10} [-\ln(P_{fa})] \quad (23)$$

The purpose of  $\Delta V$  is to control the false alarm rate. To reduce the additional false alarms that might result from the inaccuracy of the sample mean estimate, the exact value of  $\Delta V$  is determined empirically for each set of data.

## (ii) Manoeuvring targets

Figure 20 shows the response of the Cape Race HFSWR to a manoeuvring aircraft.

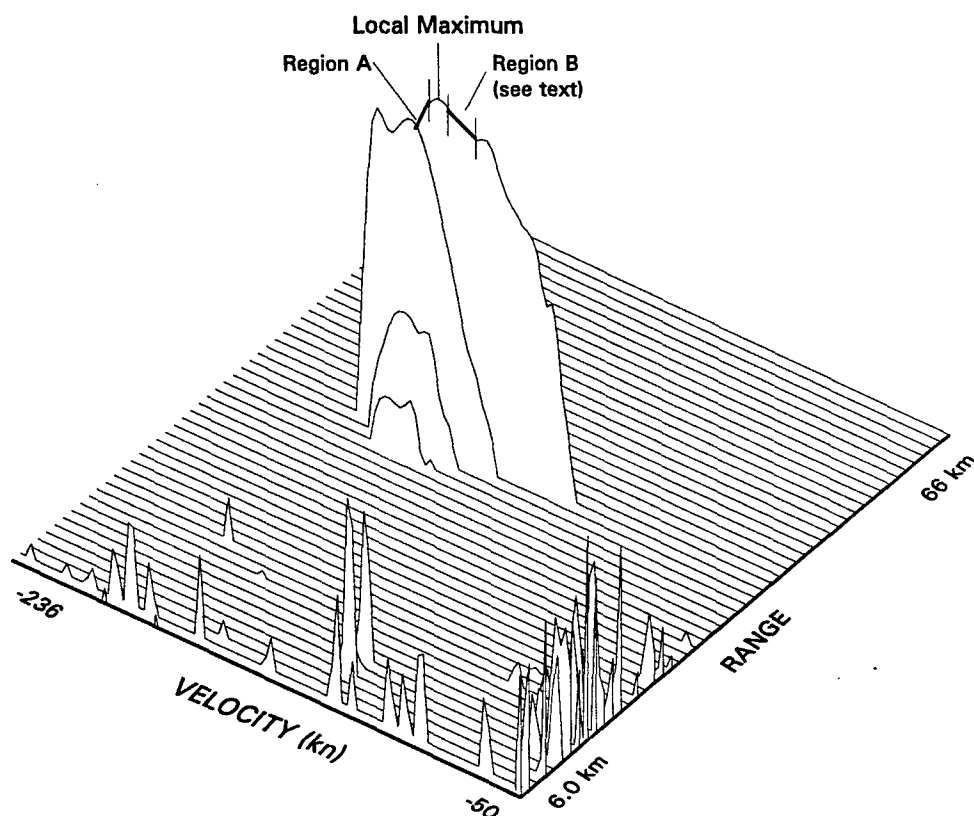


Figure 20. Range-Doppler profile of a manoeuvring aircraft.

The local maximum was found at the range of 40.8 km, a Doppler of -3.3 Hz (-169.6 knots) and a bearing of  $-6.14^\circ$  off boresight. Superimposed on the figure are regions A and B as described in Section 3.3.1 (i). It is clear that, in this case, the sample mean would be corrupted by the Doppler samples of the target. Consequently, this target would not be detected using the algorithm in Section 3.3.1(i).

Manoeuvring targets can be detected by adding a second stage in the detection process. Figure 21 shows the range profile of the Doppler component corresponding to the target observed in Figure 20. It can be seen that the target energy was concentrated in 1 or 2 range bins. Consequently a second threshold computed by range-averaging around the test bin would permit detection.

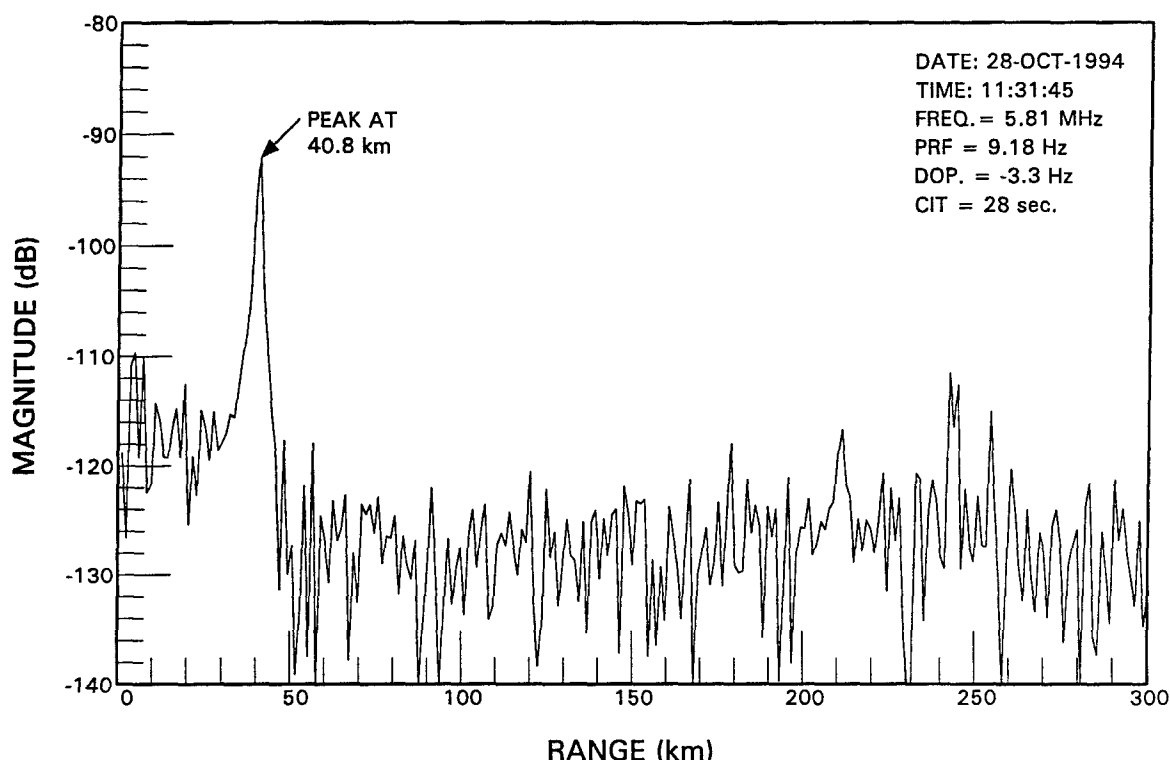


Figure 21. Range profile of the manoeuvring aircraft of Figure 19.

### 3.3.2 Tracking Algorithm.

A track is a sequence of detections of the same target over a time interval. When a target is detected, there are two courses of action for a tracker to follow: (i) associate the detection with one of the existing tracks if the target satisfies the criteria for track association; and (ii) initiate a new track if the detection cannot be associated with any existing tracks. The information associated with a target includes most or all of the following parameters: range, Doppler (velocity), heading, rate of change in heading, and acceleration. These parameters are the state variables and, collectively, referred to as the state vector of the target.

For constant velocity targets, tracking is relatively simple. Since, in HFSWR, the Doppler information of a target can be directly measured, the prediction of the range of the target at the next detection interval is fairly accurate. Although the rate of change of the target azimuth is not available from a single detection interval, this information may be derived from measurements obtained in two successive detection intervals. The association of the appropriate detections with existing tracks can be obtained easily.

The tracking of manoeuvring targets is a bigger challenge for HFSWR than for microwave radars. For microwave radars, both the update rate and the azimuthal resolution are relatively high. For a surveillance radar with a scanning antenna, the typical refresh rate is a few seconds. The azimuthal beamwidth is  $0.5^\circ$  to a couple of degrees. For microwave radars, sophisticated dynamic models and Kalman filtering techniques [21,22] are often used to enable the tracker to follow fast manoeuvring targets. For HFSWRs, the typical detection interval could be several tens of seconds, and the azimuthal beamwidth could be 5 or 6 degrees. It is possible to perform the Doppler processing more frequently by employing overlapping time series, thereby yielding a higher update rate. However this would increase the real-time computation load of the radar. Consequently, for HF radars, sophisticated dynamic models of targets are often not used because the required accuracy of state-variable estimates is not achievable. For example, because of the relative coarse azimuthal resolution and the long coherent integration time, the estimates of the bearing and its rate of change are usually not very accurate.

A simple closest-neighbour criterion was used for track association. The state variables comprise range, Doppler (range rate) and azimuth only. For each detection, estimates of the range, azimuth and Doppler of the target are obtained. The radial velocity of the target is calculated from the Doppler frequency, from which an estimate of the target range in the next detection interval is obtained. Since we have information on range rate only, movement of the target in the azimuthal dimension cannot be measured directly. This information can be obtained indirectly over several detection intervals. However, because of the long coherent integration period employed, the estimation of the target bearing at the next detection interval will not be very accurate, particularly if the tangential velocity of the target is high.

#### 4. TRIAL RESULTS.

This section presents the results of the analysis of the HFSWR data collected in October 1994. Two separate trials were carried out at Cape Bonavista. The first was on 5-6 October, and the second was on 26-27 October. Several frequencies were used: 4 MHz, 7 MHz and 16 MHz. Only one aircraft detection trial was conducted at Cape Race on 26-29 November, 1994. Three aircraft were used in the trials: (i) a Lockheed T-33 trainer jet, (ii) a Beechcraft King-Air 200 and (iii) a Canadair Challenger 601-3A. Pictures of these aircraft are shown in Figures 22, 23 and 24, respectively.

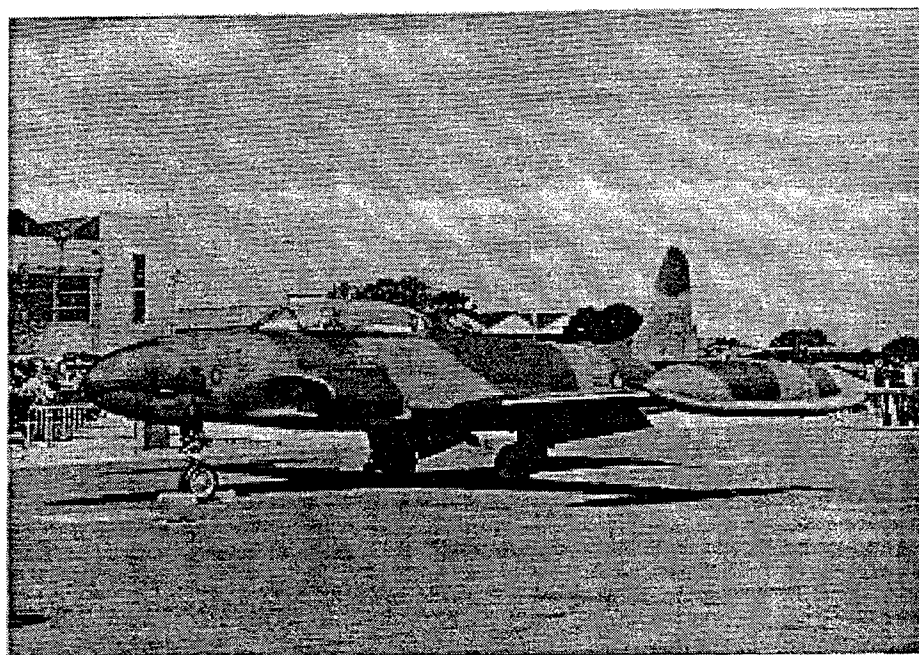


Figure 22. A Lockheed T-33 trainer jet aircraft.

It should be pointed out from the outset that the results included in this section are not presented in terms of absolutely calibrated quantities. For example, the target energy estimated from the data will not be presented in terms of joules and the noise density will not be presented in terms of watts/Hz. The reasons follow.

First, the radar at Cape Race was not owned by DND and at the time of the trial had not been properly calibrated. The calibration requires that system parameters in the radar equation such as transmit power, transmit and receive antenna gains, losses in the electronics and the scaling factors appropriate for the analog-to-digital converter (ADC) be measured for each operating frequency. To carry out such a calibration exercise would have entailed considerable cost and time. Some calibration was done on the Cape Bonavista radar, however, it was not done for all operating frequencies.



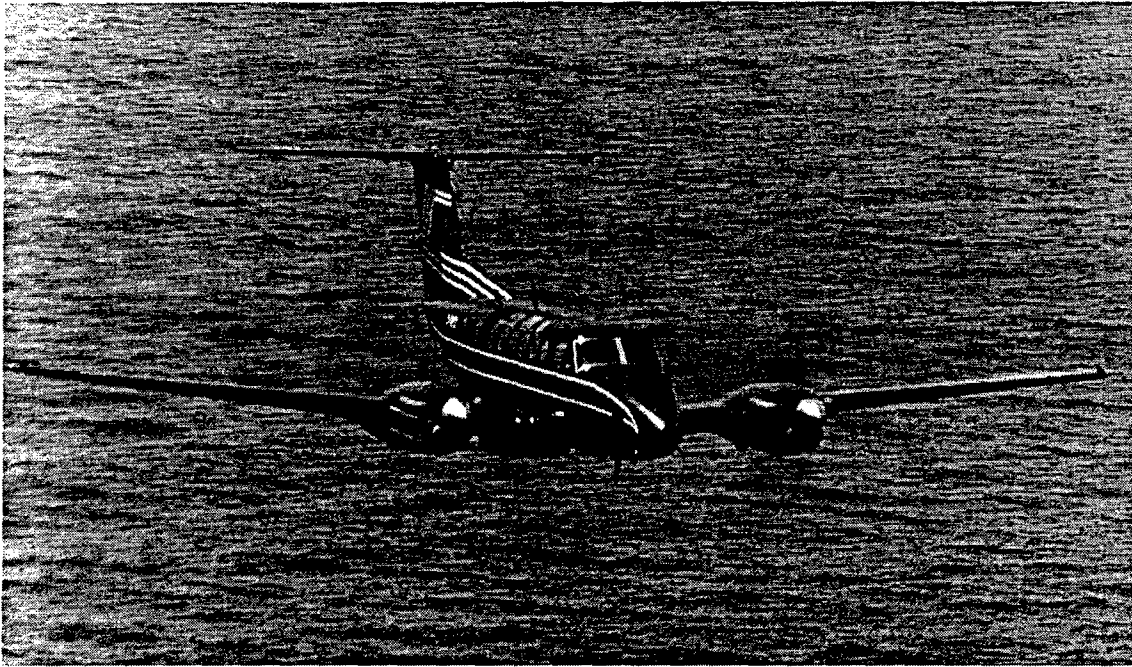


Figure 23. A Beechcraft King-Air 200 aircraft.



Figure 24. A Canadair Challenger 601-3A Aircraft.

Second, the HF surface-wave radar equation, (11), is given in terms SNR. If the noise levels at the trial sites were not drastically different from those predicted by CCIR, then a reasonable measure of the radar performance may be obtained by comparing the experimental SNR to the theoretical SNR using the CCIR noise level as a reference.

Third, the radar-cross-section (RCS) of the controlled targets had not been measured experimentally at various operating frequencies and orientations. This introduced a considerable amount of uncertainty in the estimated physical quantities such as target energy.

The results in this section will be presented on a relative basis. The trial data were processed without any conversion to physical quantities and expressed in dB with respect to unity. This, however, will not affect the experimental SNR.

The RCS of one of the controlled targets, the King-Air 200, has been computed [23] for frequencies from 3 to 35 MHz using the Numerical Electromagnetic Codes (NEC). A portion of those results is included in Appendix A.

#### 4.1 Data quality.

##### 4.1.1 Cape Bonavista Data.

Table 5 presents a brief summary of the experiments carried out at Cape Bonavista. The complete data log is contained in Appendix B.

**Table 5: Summary of Cape Bonavista Aircraft-Trial data.**

File	Date	Time	Frequency	Flight plan	Aircraft
AIR4	05-OCT-94	10:04	4.1 MHz	150 ft on Boresight	King-Air 200
AIR16	06-OCT-94	17:34	15.77 MHz	250 ft on Boresight	King-Air 200
AIRF4	27-OCT-94	11:59	4.1 MHz	1000 ft on Boresight	King-Air 200
AIRF6	27-OCT-94	12:40 13:42	6.9 MHz	1000 ft on Boresight 250 ft on Boresight	King-Air 200

The flight plan for the Cape Bonavista trial was simply to fly along the boresight ( $110^\circ$  from true North) of the radar at a fixed altitude (between 150 and 1000 feet). There were some minor problems in the data collected on 5-6 October, as will be discussed in Section 4.2.1. Data collected on 27 October were of good quality. There were two experiments performed on the 27th of October. The first one used a radar frequency of 4.1 MHz (file AIRF4), and the other used 6.9 MHz (file AIRF6). As mentioned in Section 2.3.1, these were single-beam experiments and the results did not allow digital beamforming.

#### 4.1.2 Cape Race Data.

There were 9 data files from the Cape Race trial, each of which contains the data for approximately 45 minutes. These are summarized in Table 6. A more detailed data log is contained in Appendix C.

**Table 6: Summary of Cape Race Aircraft-Trial data.**

File	Date	Time	Frequency (MHz)	Flight Plan	Aircraft
AIR_TWO	26-OCT-94	12:19 to 13:18	5.81	along boresight	King-Air
AIR_THREE	26-OCT-94	13:15 to 14:01	5.81	along boresight	King-Air
AIR_FOUR	27-OCT-94	11:09 to 11:54	5.81	along boresight	King-Air
AIR_FIVE	27-OCT-94	11:57 to 12:42	5.81	along boresight	King-Air
AIR_SIX	28-OCT-94	11:31 to 12:06	5.81	zag-zag banking	T-33
AIR_SEVEN	28-OCT-94	18:06 to 18:52	5.81	along boresight	Challenger
AIR_EIGHT	28-OCT-94	18:55 to 19:50	5.81	along boresight	Challenger
AIR_NINE	29-OCT-94	11:51 to 12:13	5.672	Figure-eight	King-Air
AIR_TEN	29-OCT-94	12:24 to 13:15	5.672	along boresight	King-Air

A preliminary examination of the data indicated that the data quality was good, except for some minor problems in ambiguous-range response, as previously discussed in Section 2.3.3 and 2.3.4. However, this ambiguous-range response does not appear very often. Hence, it did not pose a serious problem in the data analysis. The Cape Race data permitted digital beamforming since the data were sampled from the ten-element receiver array. As described in Section 2.3.4, these were composite elements formed by four antennas.

## 4.2 Maximum detection range

All of the experiments carried out at Cape Bonavista and most of those at Cape Race were designed to observe the aircraft flying at a fixed altitude along the boresight of the radar. The maximum detection range obtained from the experimental data may be used to verify the theoretical performance prediction provided by models. It may also be used to estimate the required transmit power to achieve a given detection range under normal noise environment.

### 4.2.1 Cape Bonavista results

#### (a) 16 MHz trial.

A Beechcraft King-Air 200 aircraft was used in the 5-6 October, 1994 trial at Cape Bonavista. According to the data log (see Appendix B), the flight plan called for the aircraft to fly along the boresight (110° reference to true north). Initially, however, the pilot was flying 110° referenced to magnetic north. The 15.77 MHz experiment happened to be carried out under this condition. Consequently, the signal level of the data collected on 5 October and part of 6 October were significantly lower than subsequent data.

At Cape Bonavista, the difference between magnetic north and true north is about 25°. Hence, the aircraft was actually flying at 25° off boresight. Figure 25 shows the array pattern of the receive antenna at the 15.77 MHz. It can be seen that at 25° from boresight, the array gain is about -17 dB down from the boresight gain, and the gain varies strongly with angle. Because the 15.77 MHz experiment was not repeated in the 27 October trial, these data were included in the analysis. The interpretation of the 15.77 MHz results takes into account the signal loss due to antenna beam being off boresight.

Figure 26 shows the Doppler spectrum at a range of 31 km, at which the last detection of the aircraft was made. The SNR at this range was about 10 dB.

Figure 27 shows the magnitude of the returns from the King-Air as a function of range at a frequency of 15.77 MHz. The theoretical prediction from (9) is superimposed as the solid curve in the figure, using the following parameter values

$$\begin{array}{ll} P_{av} = 40 \text{ W (16 dB)} & \\ G_t = 10 \text{ dB} & G_r = 9 \text{ dB} \\ \sigma = 11 \text{ dB} & T_i = 81.92 \text{ sec} \\ N_o = 29 \text{ dB} > kT & L_s = 3 \text{ dB.} \end{array}$$

It can be seen that the SNR obtained from the experiment was about 10-15 dB lower than the theoretical prediction. However, if the loss of signal due to the aircraft being off boresight is taken into account, the experimental result is close to and even slightly better than the theoretical prediction. Of course, the theoretical prediction is accurate only if the observed noise level is exactly what CCIR predicted. Since the CCIR-model prediction represents the median value only, the experimental result may be considered as reasonably close to theoretical prediction.

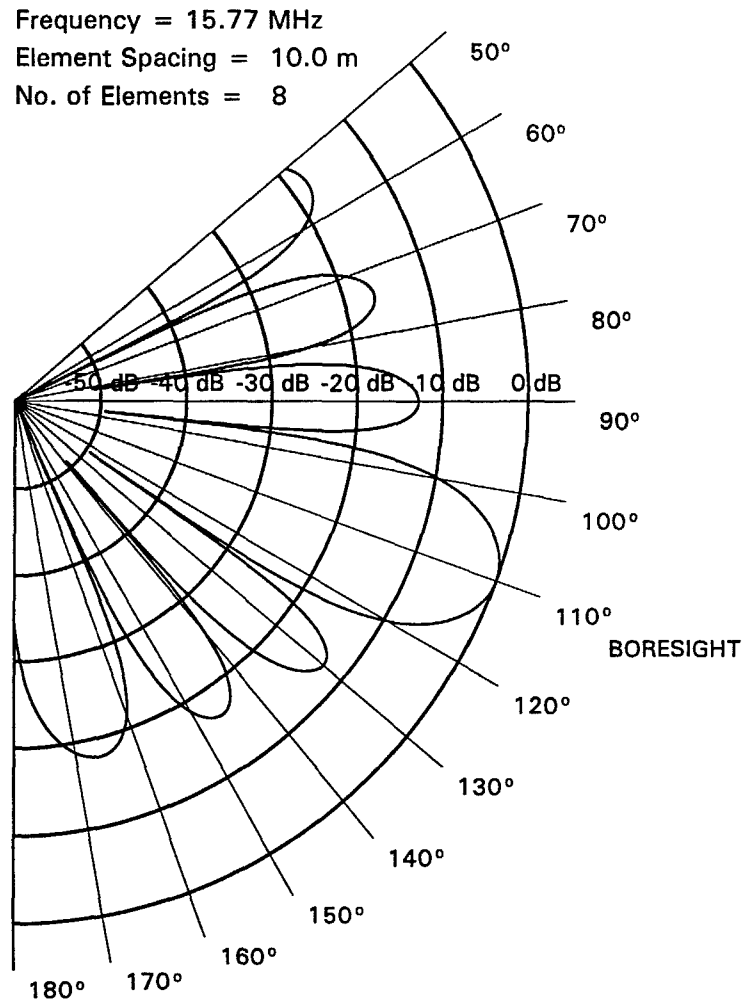


Figure 25. Array pattern of the Cape Bonavista receive antenna at 15.77 MHz.

(b) 4 MHz trial.

In the 5-6 October trial, the 4.1 MHz data were collected with the aircraft flying relative to magnetic north. This experiment was repeated on 27 October. Figure 28 shows the target energy of the King-Air 200 as a function of range as observed by the Cape Bonavista radar operating at 4.1 MHz. For this experiment, the King-Air 200 flew at a constant altitude of 1000 feet along boresight. The theoretical prediction from (9) is superimposed as the solid curve in this figure, using the following set of parameter values

$P_{av} = 25 \text{ W (14 dB)}$	$G_r = 9 \text{ dB}$
$G_t = 10 \text{ dB}$	$T_i = 41 \text{ sec}$
$\sigma = -8 \text{ dB}$	$L_s = 3 \text{ dB}$
$N_o = 29 \text{ dB>kT}$	

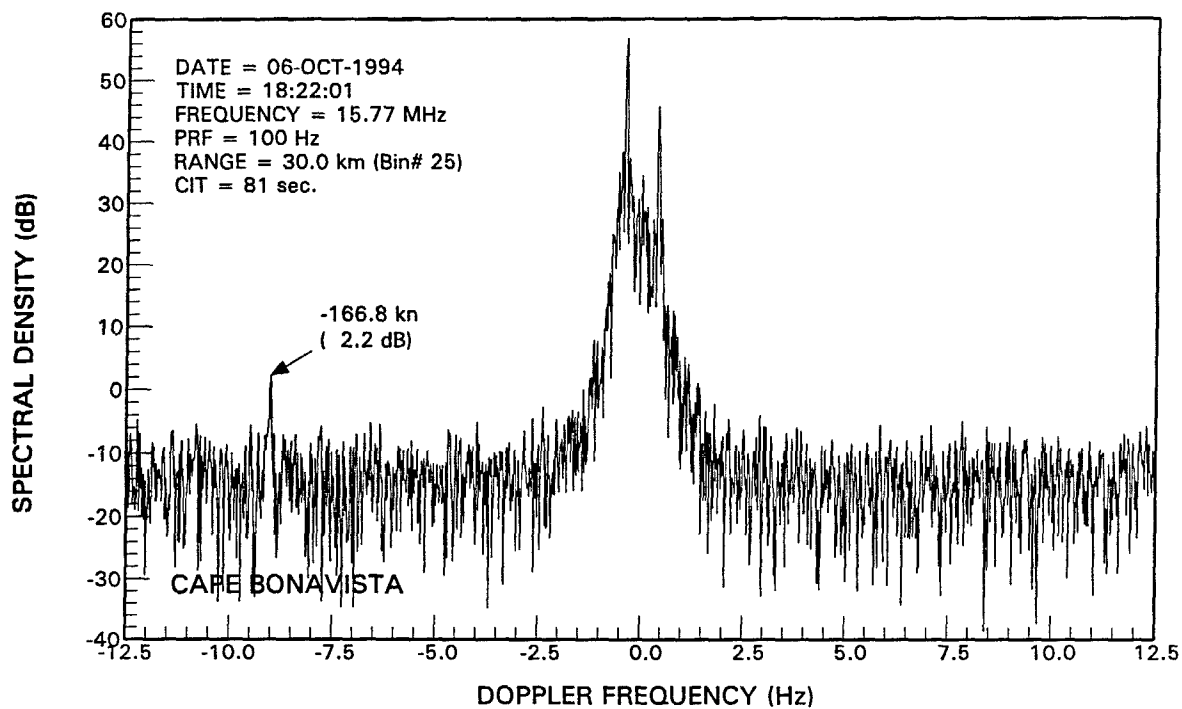


Figure 26. Doppler spectrum for a range bin where the King-Air was detected.

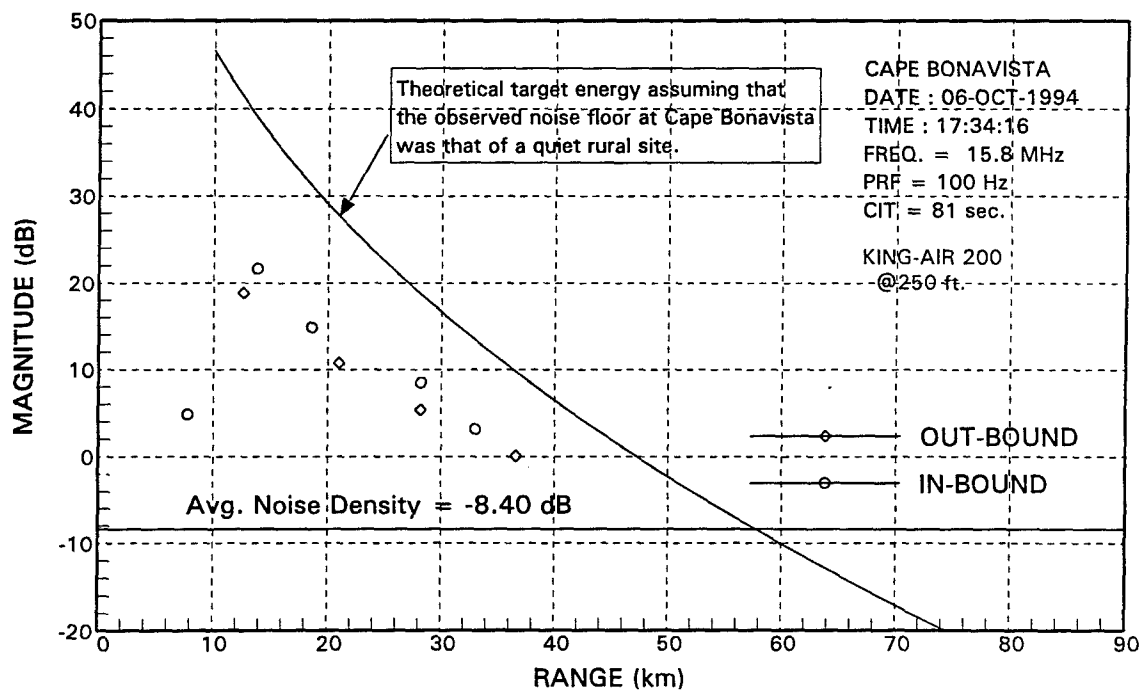


Figure 27. Target energy of the King-Air as a function of range at 15.77 Hz.

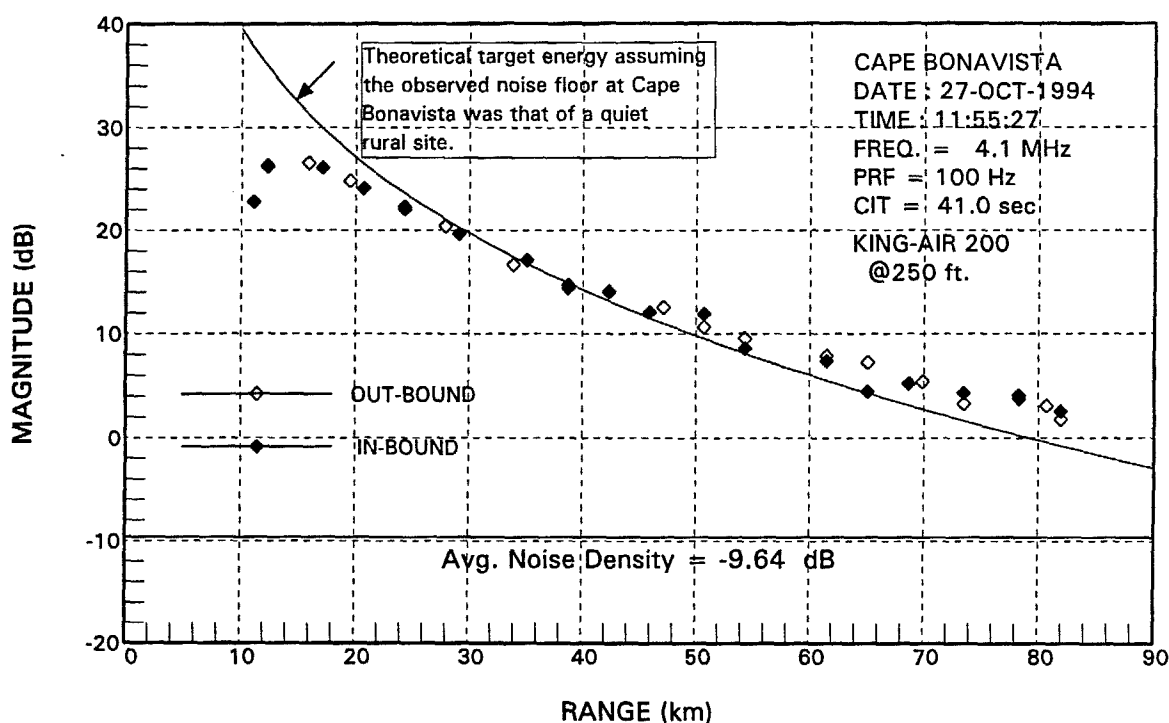


Figure 28. Target energy of the King-Air as a function of range at 4.1 MHz.

The performance was very close to the theoretical prediction or actually better. However, it must be kept in mind that the CCIR estimate of the noise level is only a median value. There is a significant amount of variation from site to site and within a time block.

(c) 7 MHz trial.

The modelling of the radar cross section of the King-Air 200 aircraft using the Numerical Electromagnetic Codes (NEC) indicated that the RCS is near a local maximum at around 7 MHz. A trial run with the radar operating at 6.9 MHz was conducted on 27 October, 1994. There were two consecutive runs in the 6.9 MHz trial. Figure 29 shows the relative magnitude of the returns from the King-Air 200 as a function of range for both runs. In the first run, the aircraft was flying at a constant altitude of 1000 feet along boresight. It then turned around at about 130 km and flew towards the radar along boresight at the same altitude. The flight plan for the second runs was similar, except that the altitude was 250 ft on both the outbound and inbound legs. The theoretical prediction from (9) is superimposed as the solid curve in this figure, using the following set of parameter values

$$P_{av} = 40 \text{ W (16 dB)}$$

$$G_t = 10 \text{ dB}$$

$$\sigma = 4 \text{ dB}$$

$$N_o = 29 \text{ dB} > kT$$

$$G_r = 12 \text{ dB}$$

$$T_i = 41 \text{ sec}$$

$$L_s = 3 \text{ dB.}$$

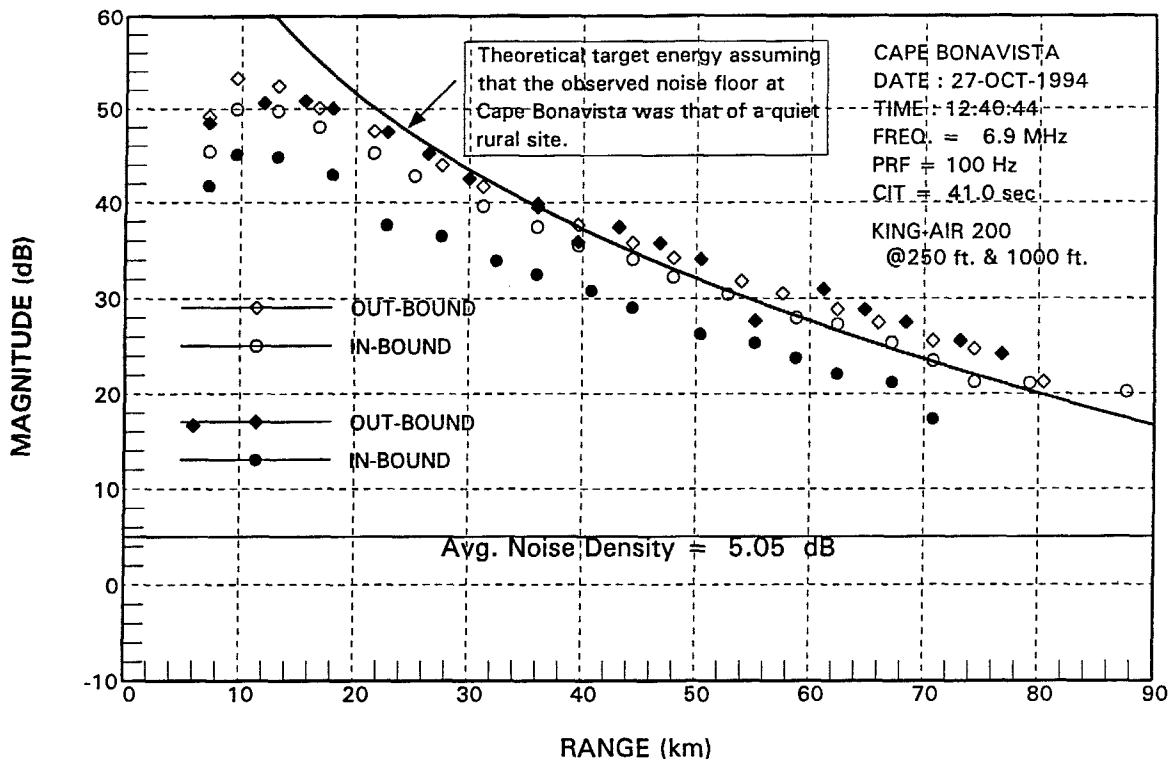


Figure 29. Target energy of the King-Air as a function of range at 6.9 MHz.

It can be seen that for most of the experiment, the performance was very close to the theoretical prediction, except during the inbound leg of the second run. The target magnitudes observed during this leg were about 6 or 7 dB lower than those observed in the other legs. Since all the system and environment parameters were identical, the most plausible contributor to this reduction in target echo magnitude would be the aircraft's RCS. Since the RCS of this aircraft is near resonance at around 7 MHz, a small change in its orientation could make a substantial difference in the observed RCS.

On the out-bound leg in both runs, the observed target magnitudes were comparable. This indicated that there was not much difference in the RCS at 250 ft compared with that at 1000 ft.

#### (d) Summary of Cape Bonavista results.

Based on the experimental results obtained at nominal frequencies of 4, 7 and 16 MHz, it may be concluded that the performance of the Cape Bonavista HFSWR, in terms of detection range, is very close to theoretical prediction. The noise environment of Cape Bonavista may be classified as a very quiet rural site.



#### 4.2.2 Cape Race results.

Files AIR\_TWO, AIR\_THREE, AIR\_FOUR, AIR\_FIVE, AIR\_NINE and AIR\_TEN listed in Table 6 were collected with the King-Air 200 as a controlled target. Files AIR\_SEVEN and AIR\_EIGHT were collected with the Challenger.

Figures 30 to 34 show the target energy of the King-Air as a function of range derived from data files AIR\_TWO, AIR\_THREE, AIR\_FOUR, AIR\_FIVE and AIR\_TEN, respectively. Most of these experiments were carried out between 1000 and 1300 hours. The minimum observed noise density was about -125 dB. At 6 MHz, the median noise density predicted by CCIR for Cape Race is about 33.5 dB above kT. The theoretical target energy, as a function of range, is superimposed in these figures as the solid curve, assuming the following set of parameters

$P_{av} = 40 \text{ W (16 dB)}$   
 $G_t = 10 \text{ dB}$        $G_r = 26 \text{ dB}$   
 $\text{PRF} = 330 \text{ Hz}$        $\tau = 240 \text{ } \mu\text{sec}$   
 $\sigma = -1 \text{ dB}$        $T_i = 28 \text{ sec}$   
 $N_o = 41 \text{ dB} > kT$        $L_s = 3 \text{ dB}.$

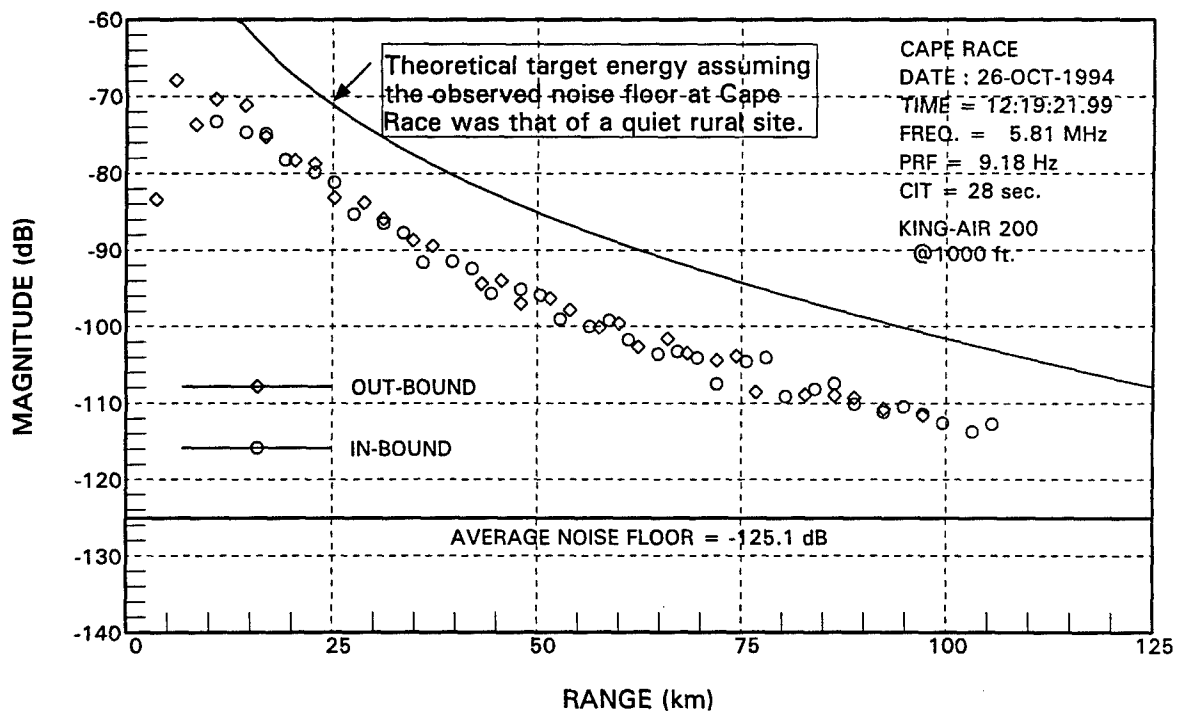


Figure 30. Target Energy of the King-Air as a function of range at 5.81 MHz.

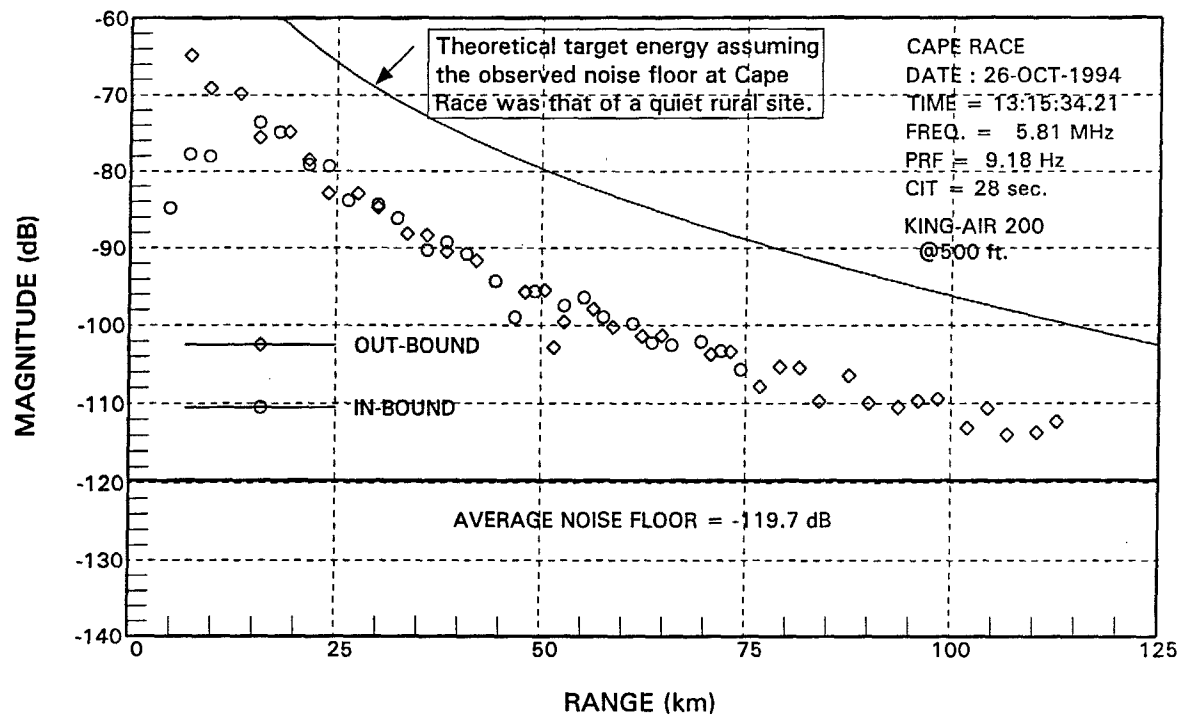


Figure 31. Target Energy of the King-Air as a function of range at 5.81 MHz.

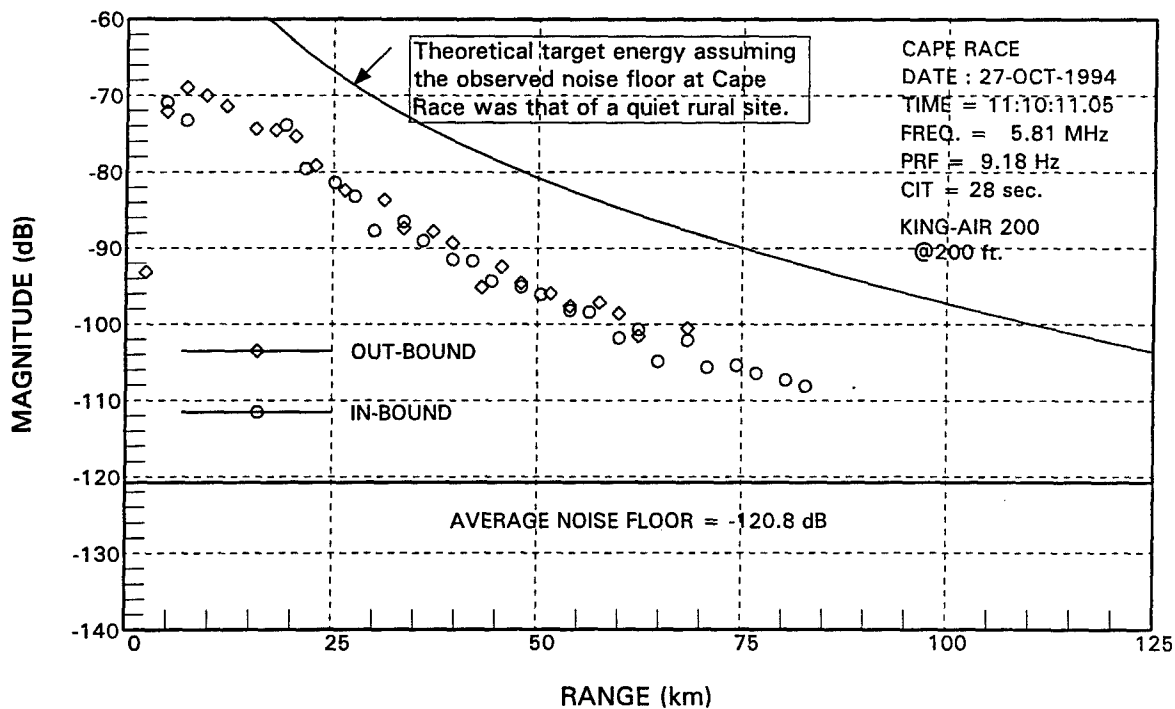


Figure 32. Target Energy of the King-Air as a function of range at 5.81 MHz.

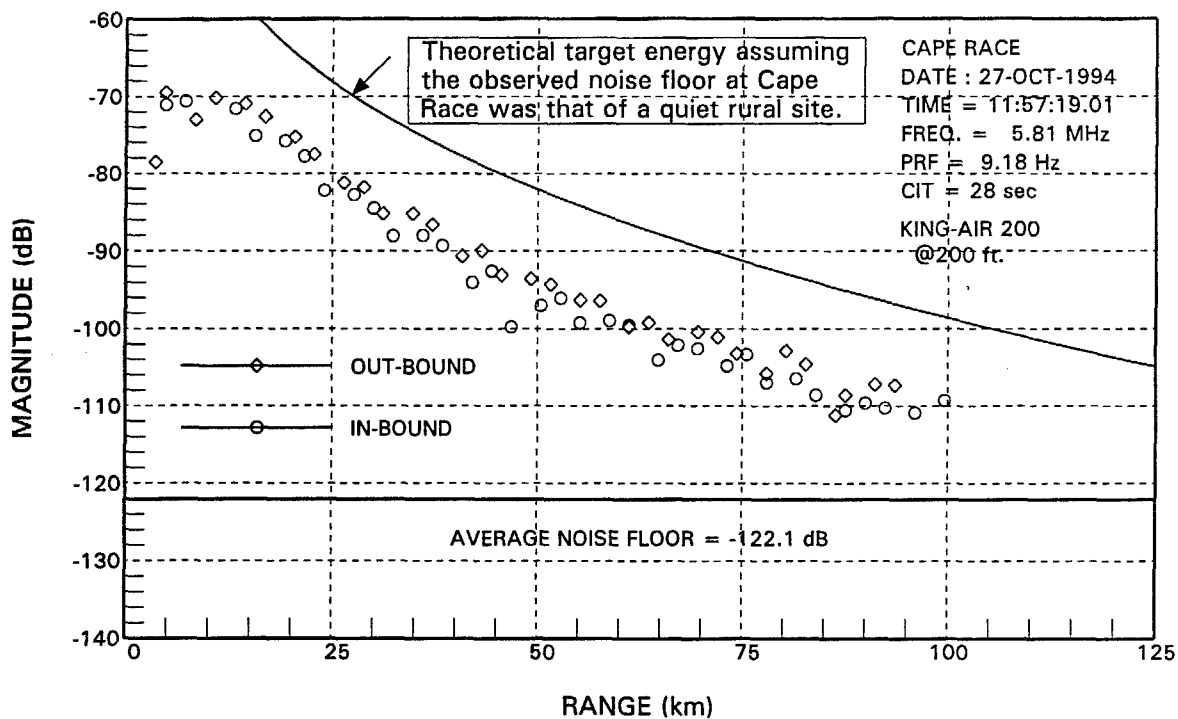


Figure 33. Target Energy of the King-Air as a function of range at 5.81 MHz.

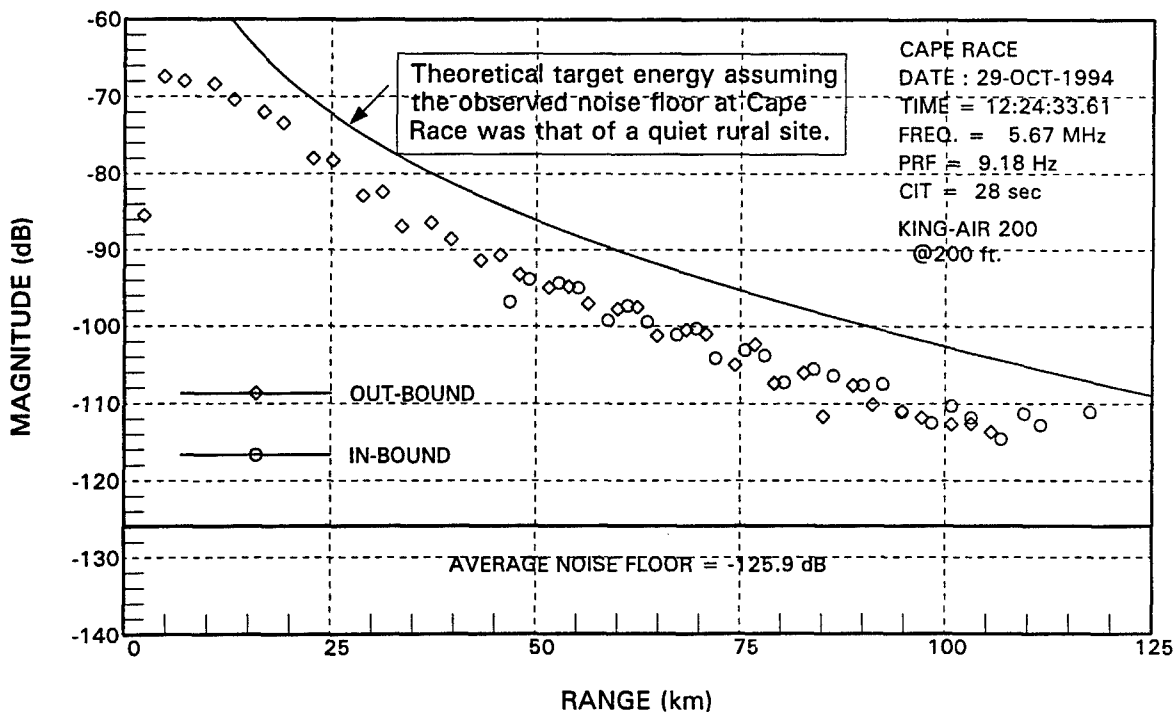


Figure 34. Target Energy of the King-Air as a function of range at 5.81 MHz.

The maximum range at which the King-Air was detected was about 120 km. In all cases, there was no significant difference in the observed target energy between the in-bound and out-bound legs. It appeared that the SNR achieved with the Cape Race radar was about 10 dB below the expected value. Possible causes for this deficiency will be presented in Section 4.6.

Figures 35 and 36 show the target energy of a Challenger 601-3A, as a function of range, derived from files AIR\_SEVEN and AIR\_EIGHT, respectively. These two experiments were carried out between 1800 and 1900 hours. The minimum observed noise density was about -117 dB. During this time the CCIR predicted median noise density is about 40.9 dB above kT. To obtain an estimate of the theoretical performance of the radar, an estimate of the RCS of the Challenger was needed. However, the Challenger was not one of the aircraft for which the RCS has been computed in [20]. In Section 4.5 an estimation of the RCS of the Challenger in level flight is estimated relative to that for the King-Air.

The maximum range at which the Challenger was detected was about 115 km. It can be observed that the target energy was about 10 dB higher on the out-bound leg, compared with that for the in-bound leg. It is not certain what causes this reduction.

A possible explanation is that the orientation of the aircraft relative to the radar was different for the in-bound and out-bound legs. Figures 37 and 38 plot the radial velocity of the Challenger during experiment AIR\_SEVEN and AIR\_EIGHT, respectively. It can be observed that on the out-bound leg (white diamond symbol), the average aircraft radial speed was about 215 knots, whereas on the in-bound leg, it was only about 175 knots. It is possible that the aircraft was experiencing a strong head wind on the in-bound leg and had to change its orientation slightly to maintain a constant altitude.

On the in-bound leg, the aircraft was not detected until it was within 40 km. The reason was that during data collection for AIR\_SEVEN and AIR\_EIGHT, there was a persistent co-channel interference component which coincided with the target Doppler, and the resulting SNR was not high enough for detection until the aircraft echo was sufficiently above the interference component. This is evident by examining the 3D Doppler-range profile in Figure 39.

### **4.3 Tracking of manoeuvring targets**

Files AIR\_SIX and AIR\_NINE contain data collected from the Cape Race radar with the controlled aircraft flying certain prescribed patterns.

#### **4.3.1 King-Air 200 in figure-eight manoeuvre**

For File AIR\_NINE the King-Air flew two figure-eight patterns at 200 ft and 500 ft altitude. Each figure-eight pattern comprised two circles, with a diameter of about 10 km. The aircraft flew from St. John's, Newfoundland to a location approximately 42 km from Cape Race and commenced the first figure-eight manoeuvre at an altitude of 200 ft. Upon the completion of the first figure-eight pattern, it then increased the altitude to 500 ft and executed the second figure-eight manoeuvre. The data in this file was processed as outlined in Section 3.2. The resulting track for this experiment is shown in Figure 40.

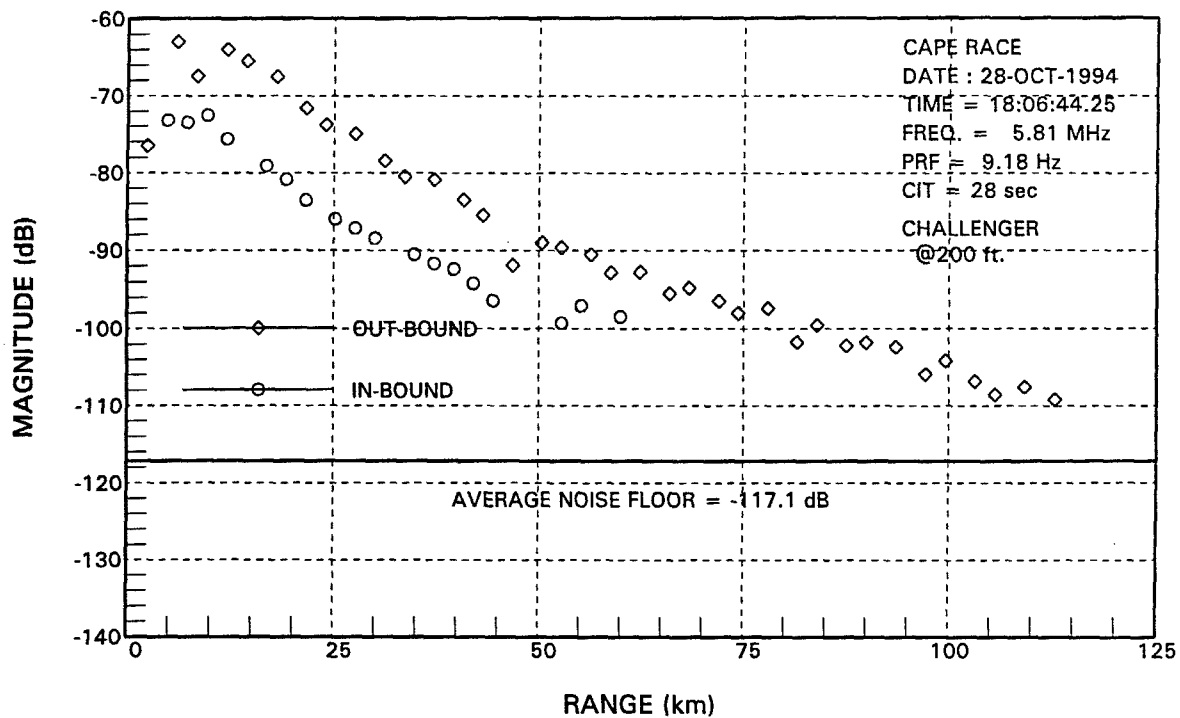


Figure 35. Target Energy of the Challenger as a function of range at 5.81 MHz.

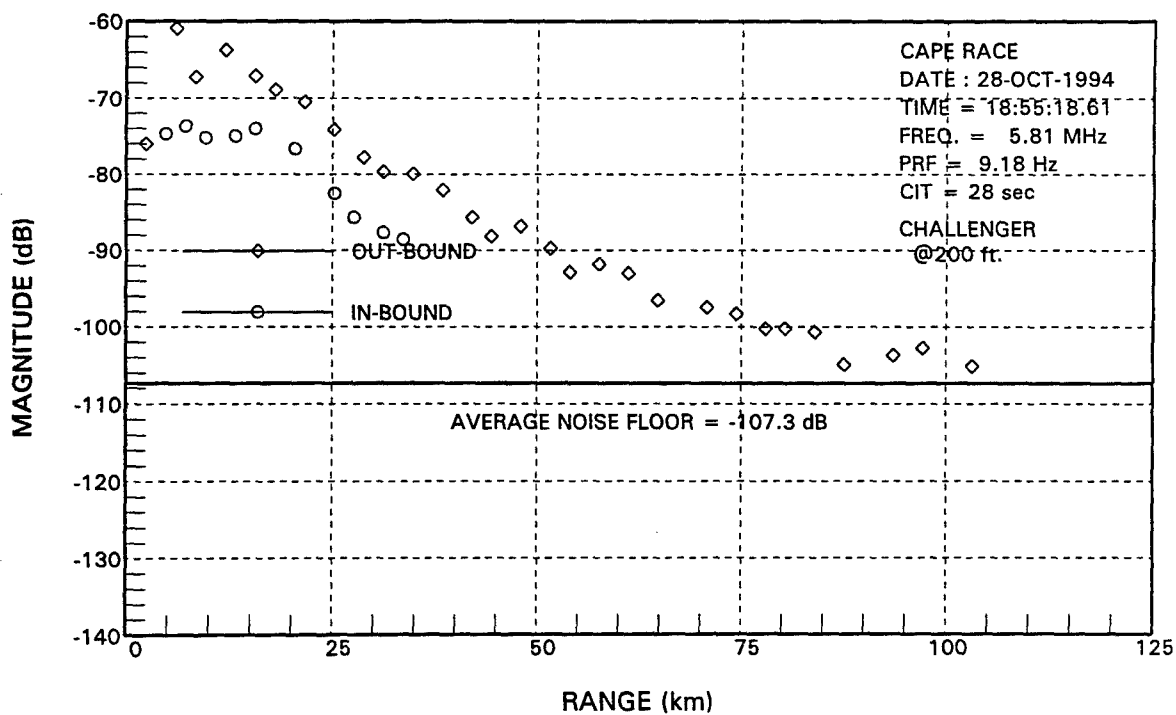


Figure 36. Target Energy of the Challenger as a function of range at 5.81 MHz.

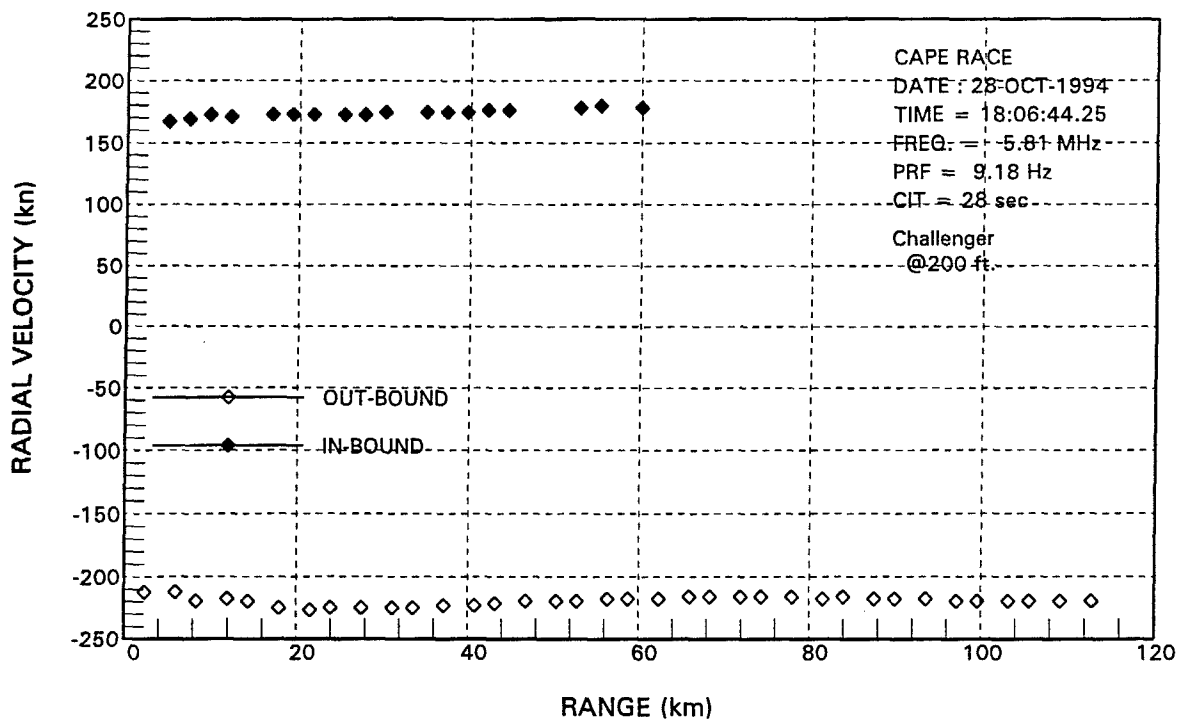


Figure 37. Radial velocity of the Challenger as a function of range.

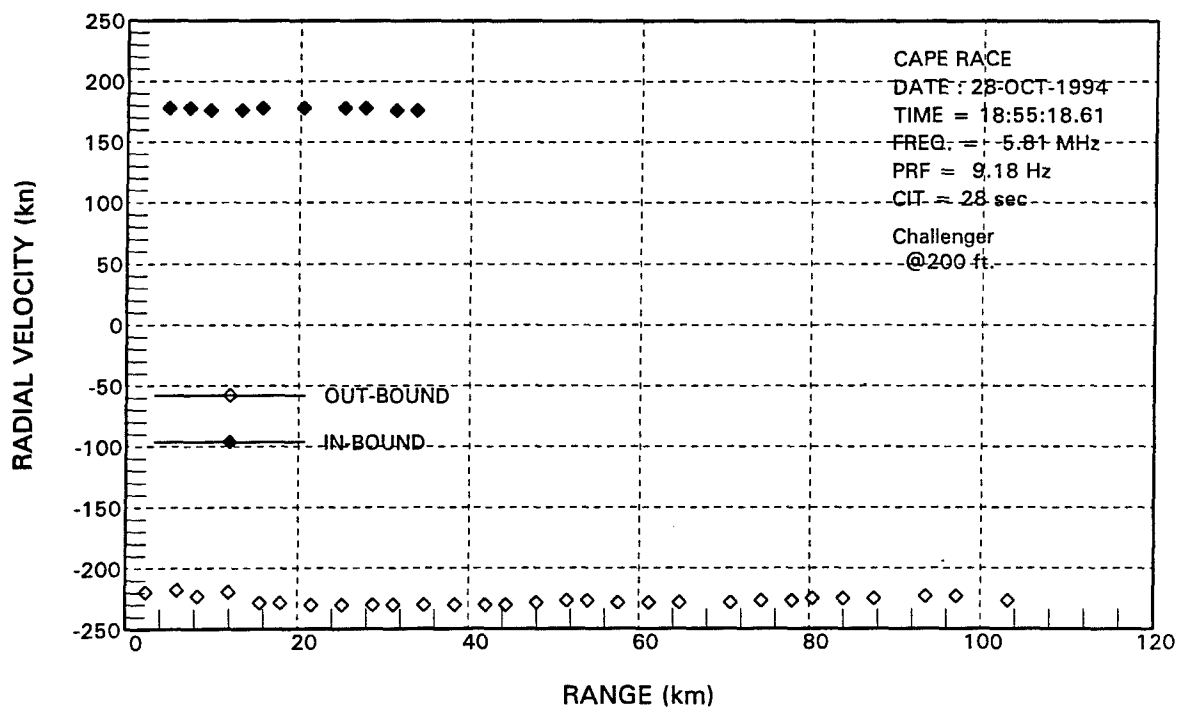


Figure 38. Radial velocity of the Challenger as a function of range.

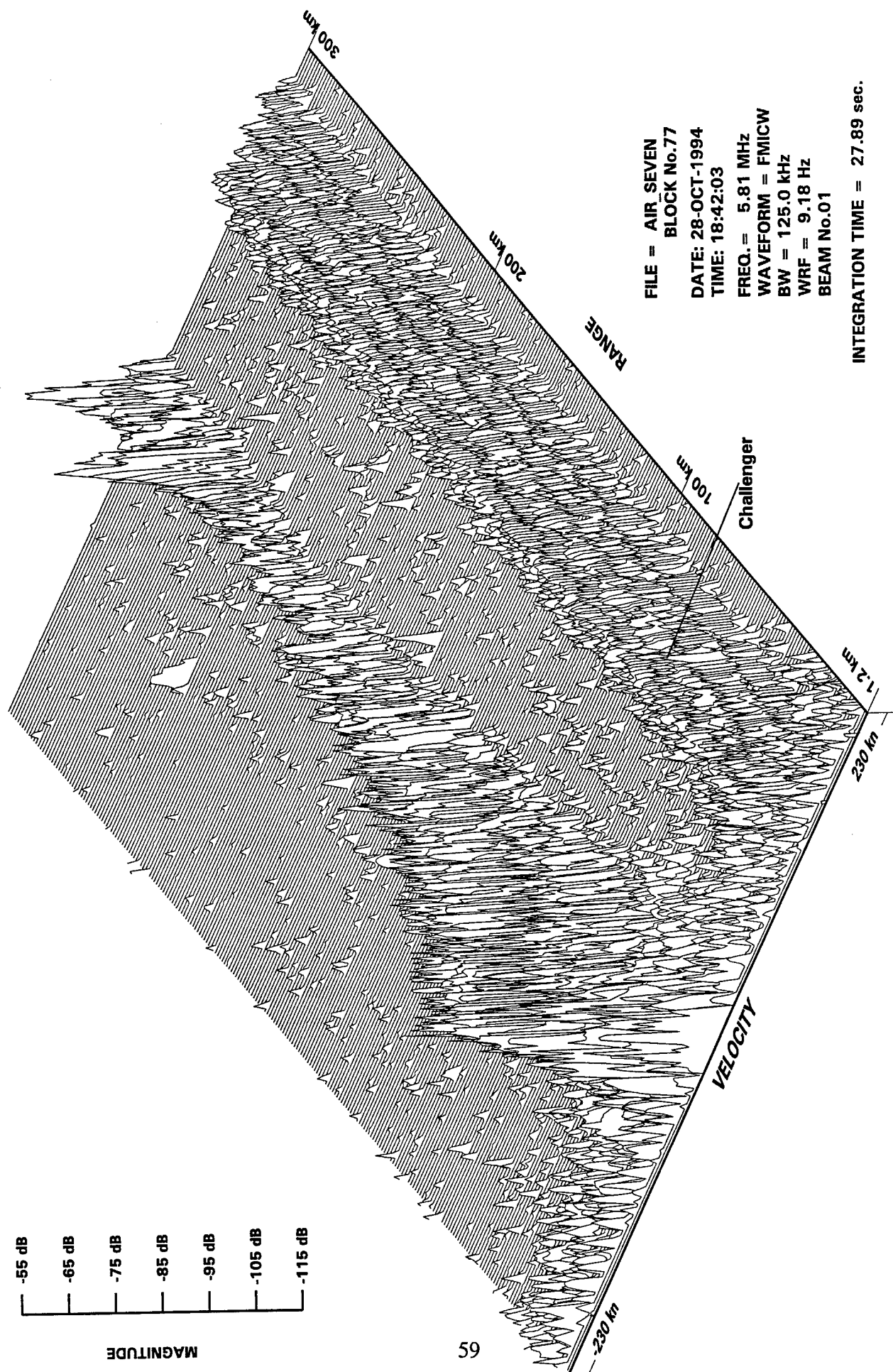


Figure 39. Degradation of detection performance due to co-channel interference.

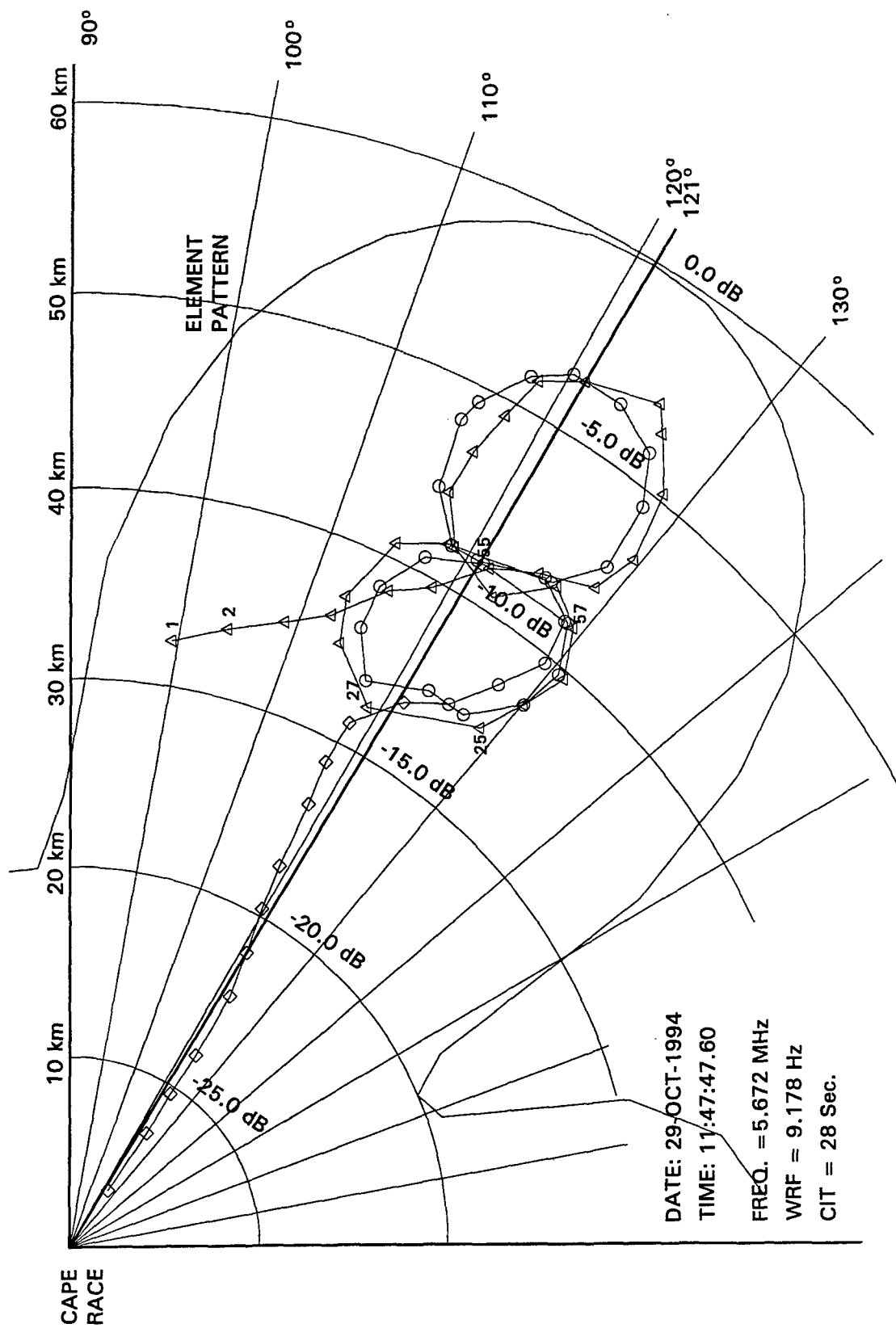


Figure 40. Track of the King-Air 200 during a figure-eight manoeuvre.



The length of time for the data in file AIR\_NINE was about 2000 seconds. Since each CIT interval was about 27.89 seconds, there were 72 CIT intervals. The numerical values appearing beside the track denotes the CIT number of the detection. The elemental pattern of the composite antenna element is superimposed on the figure. The target was first detected in CIT No.1 at an azimuth of  $99.5^\circ$  true. Although, at this azimuth, the receive element gain was -14 dB down from the peak, the SNR of the initial detection was about 30 dB. The first two detections were actually detected at an ambiguous azimuth, and these were corrected.

Several detections were missed due to the flight path of the aircraft, at those time intervals, being almost tangential with respect to the radar beam. This occurred during CIT Nos. 26, 32 and 56. Figures 41a, 41b and 41c show the spectra in which the aircraft appeared in CIT No.25, 26 and 27, respectively. In CIT No. 25, the aircraft was at a range of 34.8 km and an azimuth of  $127.48^\circ$  true, and the radial velocity was 145.6 knots. It can be seen that the Doppler spread of the target was from about 2.2 Hz to about 3.5 Hz, which indicated that the aircraft was slowing down from a velocity of 175.6 knots to a low of 110 knots. In CIT No.27 (Figure 41c) the aircraft was at a range of 32.4 km and an azimuth of  $118.87^\circ$  true. The nominal radial velocity was -77 knots. Figure 41b shows the spectrum at 32.4 km in CIT No.25 where the aircraft was expected to be. Although visually, one could discern that there could be a target; however, the detection algorithm did not pick it up because the target's Doppler was too close to the sea-clutter dominated region. Similar behaviour may be observed in Figures 41d, 41e and 41f for CIT No. 55, 56 and 57, respectively.

The RCS of a manoeuvring aircraft could vary over a very wide range in magnitude because of changes in aspect angle and orientations. Figure 42 compares the peak target-echo energy and the total target-echo energy of the King-Air as a function of CIT number. The peak-target energy is that contained in the Doppler bin that is the local maximum. The total echo energy is the sum all of the Doppler components. The number of Doppler bins to be summed was determined by visually examining the spectra that contain the target. Up to 15 dB increase in the target-echo energy was observed.

#### **4.3.2 T-33 in banking manoeuvre**

File AIR\_SIX contains the data collected with a T-33 trainer flying out of Cape Race at 200 ft altitude to about 50 km. It then turned around and headed straight towards Cape Race. On the way out on the second leg, it executed several banking manoeuvres. Figure 43 shows the accumulated tracks of the T-33 during this experiment. Figure 44 plots the peak echo energy and the total echo energy of the T-33 aircraft as a function of CIT interval number. The first outbound leg started from integration period No.1 and the first in-bound leg began at about integration period No.22. It can be seen that the target-echo energy varied directly with range. The second outbound leg began approximately at integration period No. 47, and the second in-bound leg began approximately at integration-period No. 59. The banking manoeuvre could be observed from the large swing in the target echo. These occurred approximately at CIT No.s 49, 53, 62 and 67. The RCS of the T-33 was observed to increase by as much as 20 dB during manoeuvring.

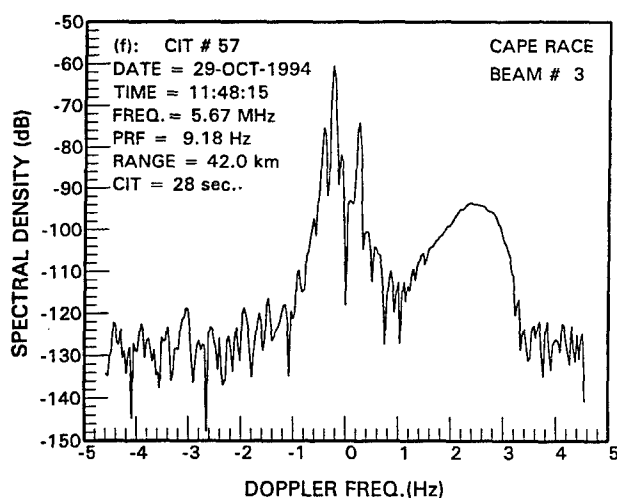
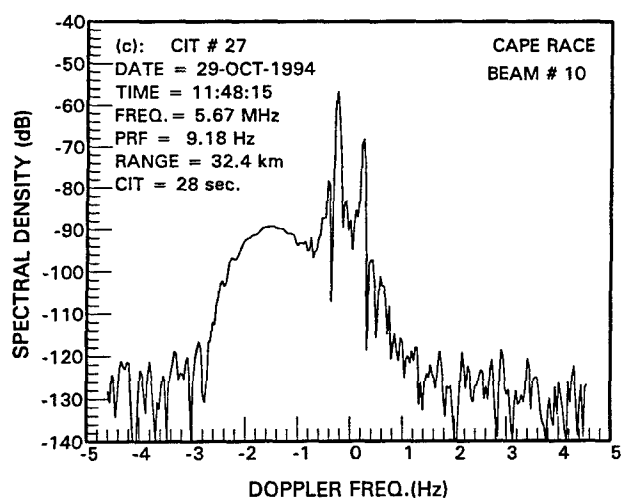
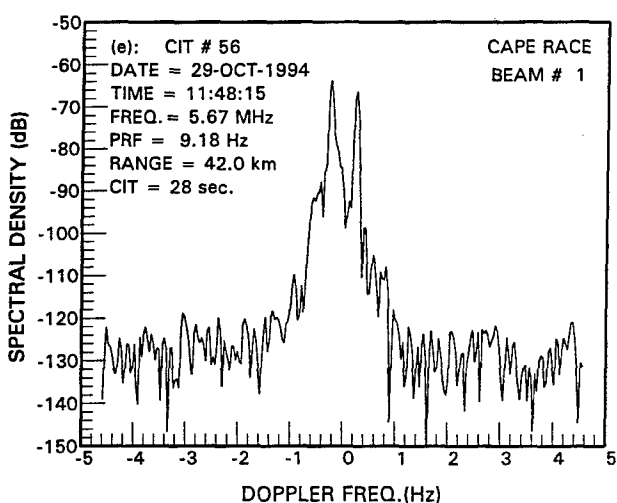
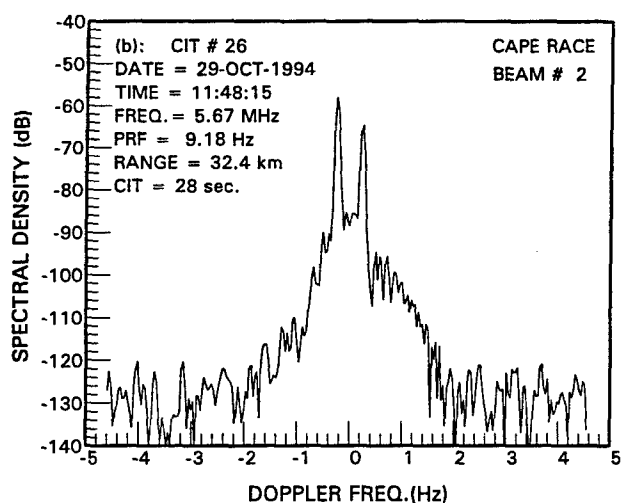
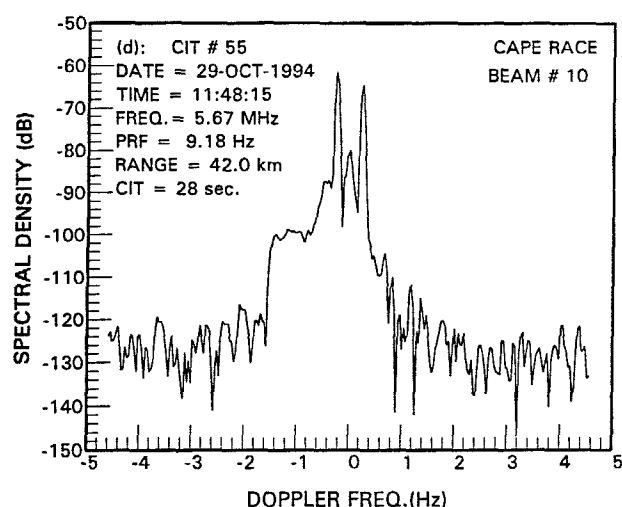
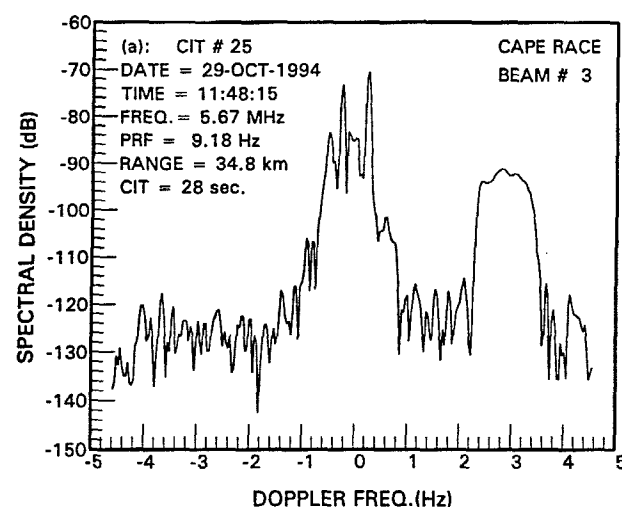


Figure 41. Spectra of a manoeuvring aircraft near tangential heading.

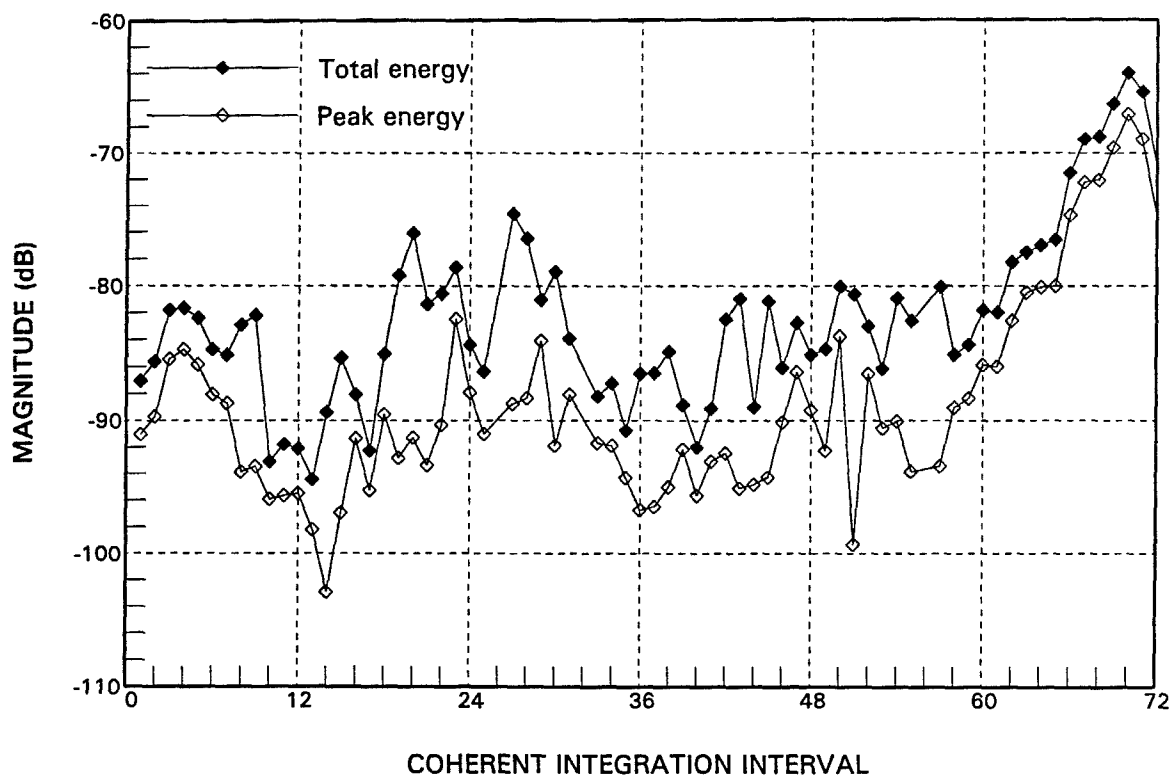


Figure 42. Comparison of peak energy and total energy of the King-Air in figure-eight manoeuvre.

#### 4.4 Targets of opportunity

##### 4.4.1 Commercial airliners and military aircraft

Figure 45 shows the tracks obtained from Cape Race data set AIR\_SIX. In addition to the track of the controlled target, a T-33, a straight line track of a target was observed at ranges between 150 km and 250 km. This track, in all probability, corresponded to that of an aircraft at a high altitude. Also shown in Figure 45 is the antenna pattern of the composite element which was centred about the boresight ( $121^\circ$  true). The scale for the antenna pattern was 5 dB per division as shown at the intersection between the concentric arcs and the  $121^\circ$  radial. The airliner was first detected at a range of 170.4 km and an azimuth of  $147.4^\circ$  true and was travelling away from the radar where it entered the mainlobe of the receive antenna. At this point the antenna gain was about 12 dB down from that of the boresight. Before that, the bearing of this target was in the vicinity of the first null of the antenna pattern, and consequently the SNR was too low for detection.

This target was last detected at a range of 240 km and an azimuth of  $107.5^\circ$ . The time interval for this target to traverse the entire track, which spanned a distance of about 152 km, was 530 seconds. This translated to a speed of 287 m/sec or 558 knots. This speed is slightly higher than that of an airliner.

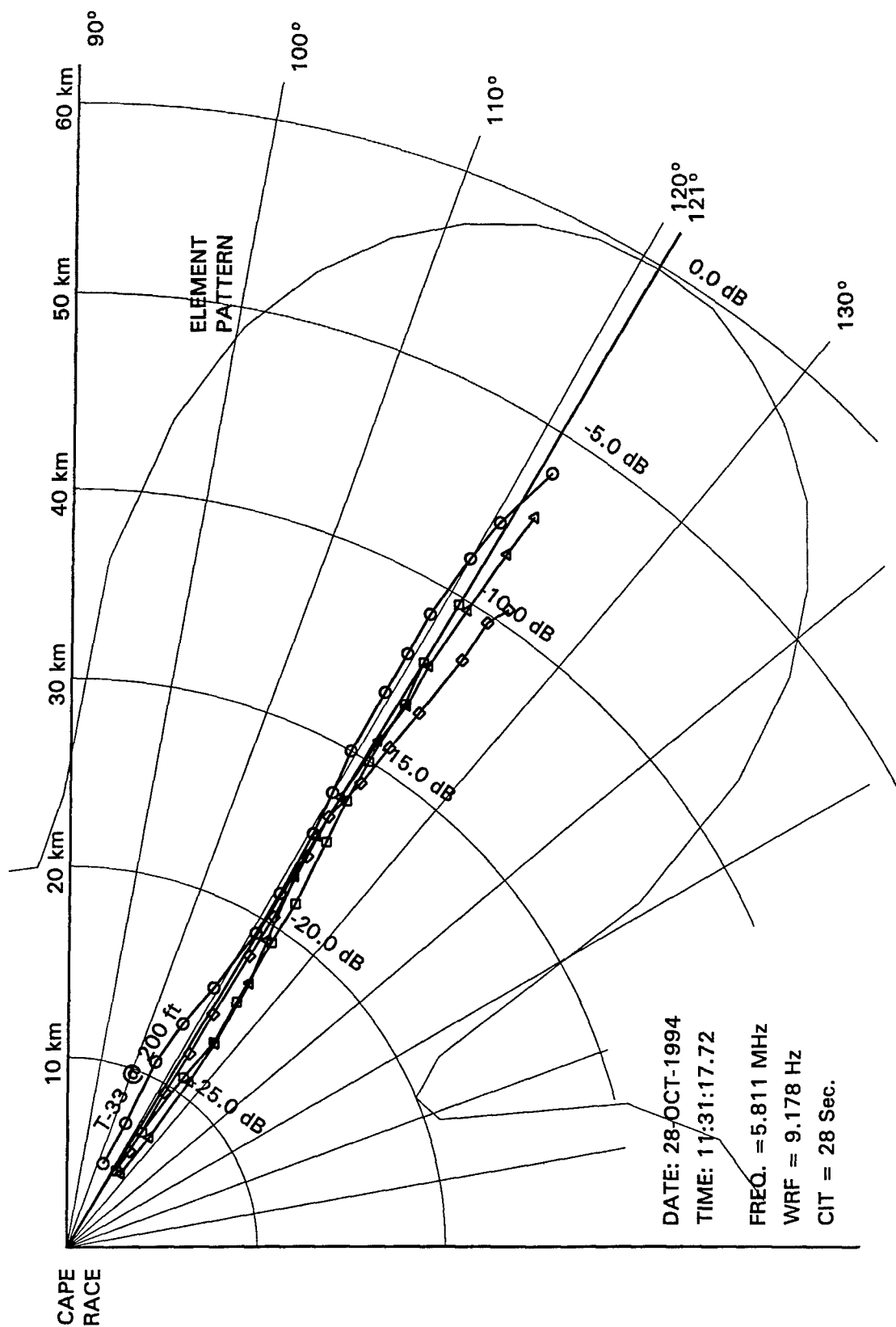


Figure 43. Track of the T-33 in an experiment with banking manoeuvre.

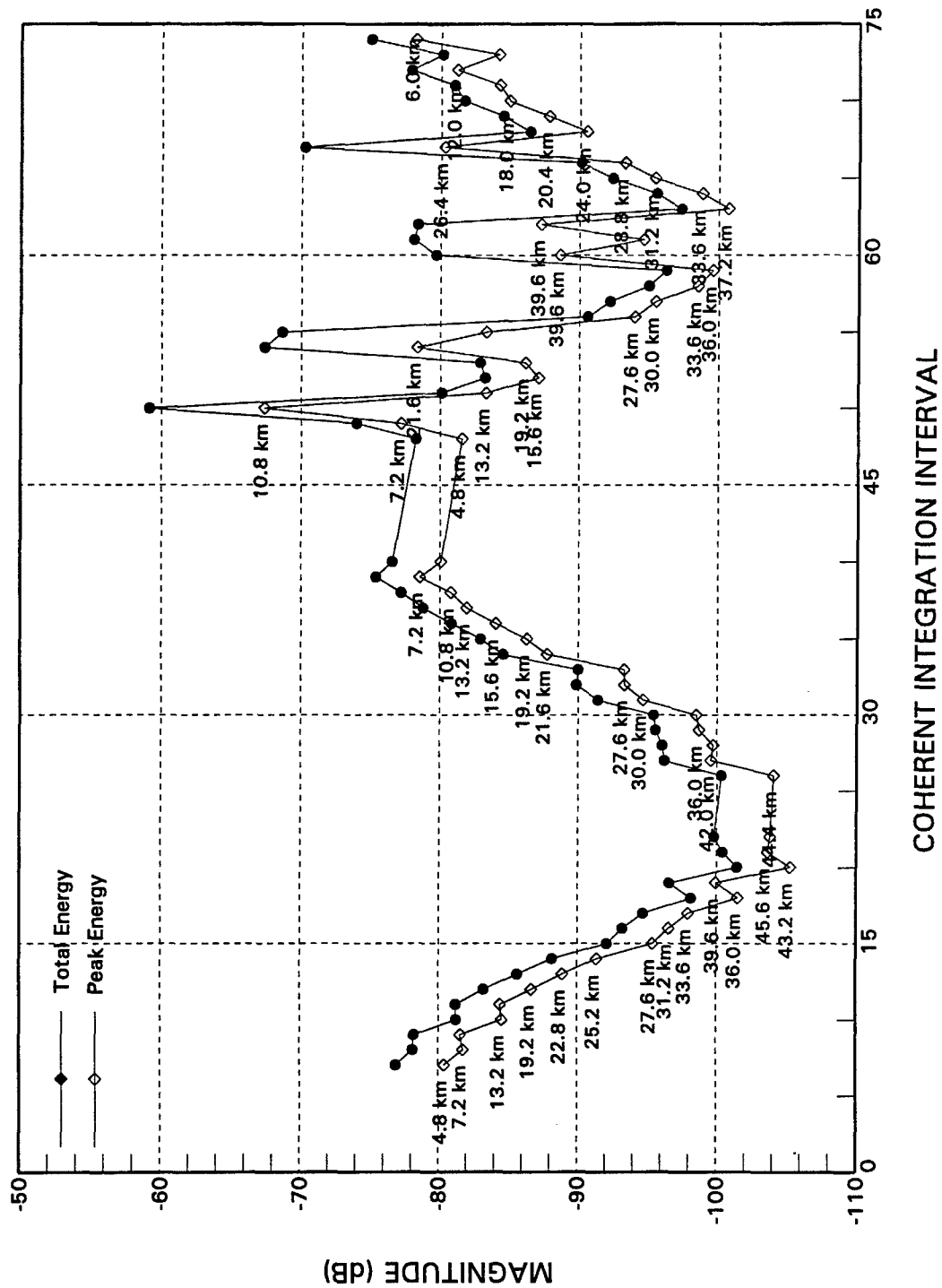


Figure 44. Comparison of peak and total target energy for a T-33 in banking manoeuvre.

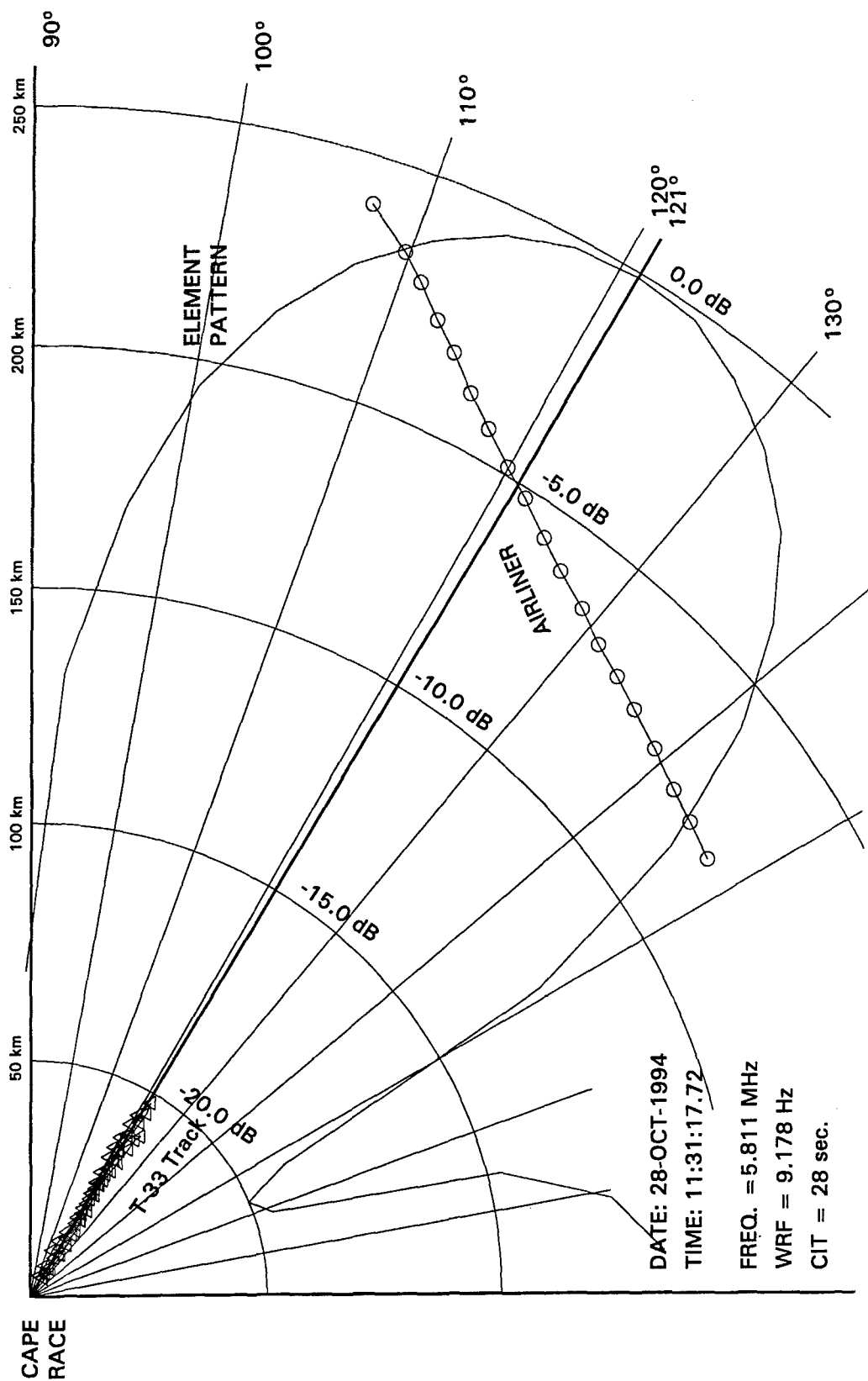


Figure 45. Accumulated tracks derived from data file AIR\_SIX.

Figure 46 plots the radial velocity of the aircraft as a function of range. It ranged from about -50 knots to over -400 knots. Since the target appeared to have maintained a constant heading and speed, the variation in radial velocity was due entirely to the change in the target bearing as the aircraft crossed the antenna beam.

Figure 47 plots the target magnitude as a function of bearing relative to boresight. The ranges at which the target was detected were labelled. The magnitude of targets off boresight was subjected to an attenuation due to the antenna pattern. For example, the detection at 170.4 km would have a magnitude almost 9 dB higher if the elemental pattern were pointing at  $(121+26)^\circ$ .

Adding the loss due to the antenna pattern to the magnitudes of each detection, the actual target magnitude (i.e., without the effects of the antenna pattern) is plotted against range in Figure 48. Assuming that this aircraft was flying at a relatively high altitude ( $> 25,000$  ft), it would be within the line-of-sight of the radar. Furthermore, it is assumed that the change in the radar cross section is small for small changes in aspect angles, which is a reasonable assumption at HF. For example in Figure A1 of Appendix A, the difference in RCS between the cases of nose-on and broad-side incidence for a King-Air 200 at level, as predicted by NEC, was only a few dB. The two-way propagation loss would be proportional to  $1/R^4$ , or a decrease of 12 dB per doubling of the range. By fitting a straight line through the triangular symbols (only those within the 3-dB beamwidth) and examining the slope, it can be seen that the magnitude decreased approximately at a rate of 12 dB per doubling of the range.

Figure 49 shows the tracks obtained from data set AIR\_SEVEN. Again it shows that, in addition to the track of the controlled target (an Air Force Challenger), a straight-line track was also obtained. This target was first detected at a range of 294 km and an azimuth of  $104^\circ$  true. The radar indicated receding target with a radial velocity of -59.36 knots. Subsequent detections, however, indicated that the target was approaching the radar. This discrepancy was attributed to the low WRF of the Cape Race radar which gave rise to ambiguous velocity. The maximum unambiguous radial-velocity domain of a radar is given by

$$(v_{\max}, v_{\min}) = \pm \frac{1}{2} \left[ \frac{(\text{WRF}) \lambda}{2} \right]. \quad (24)$$

At 5.81 MHz and a WRF of 9.18 Hz, a target with a true radial velocity of about 391 knots would produce an aliased radial velocity of -59.36 knots.

The target could not be detected after CIT No.46, at which time the target range was 136.8 km and the azimuth was  $143.4^\circ$  true. From the elemental pattern superimposed on Figure 49, detection was lost because the target was exiting the main lobe. Several more detections were obtained, beginning at CIT No.58, at which time the target range was 124.8 km and the azimuth was  $177.1^\circ$  true. From the accumulated track plot, it is clear that these detections were associated with the lost track and these were detections via the first sidelobe of the elemental pattern. Dividing the length of the track with the elapsed time, the speed of this target was estimated to be about 219 m/sec or 426 knots. This is compatible with that of a commercial airliner.

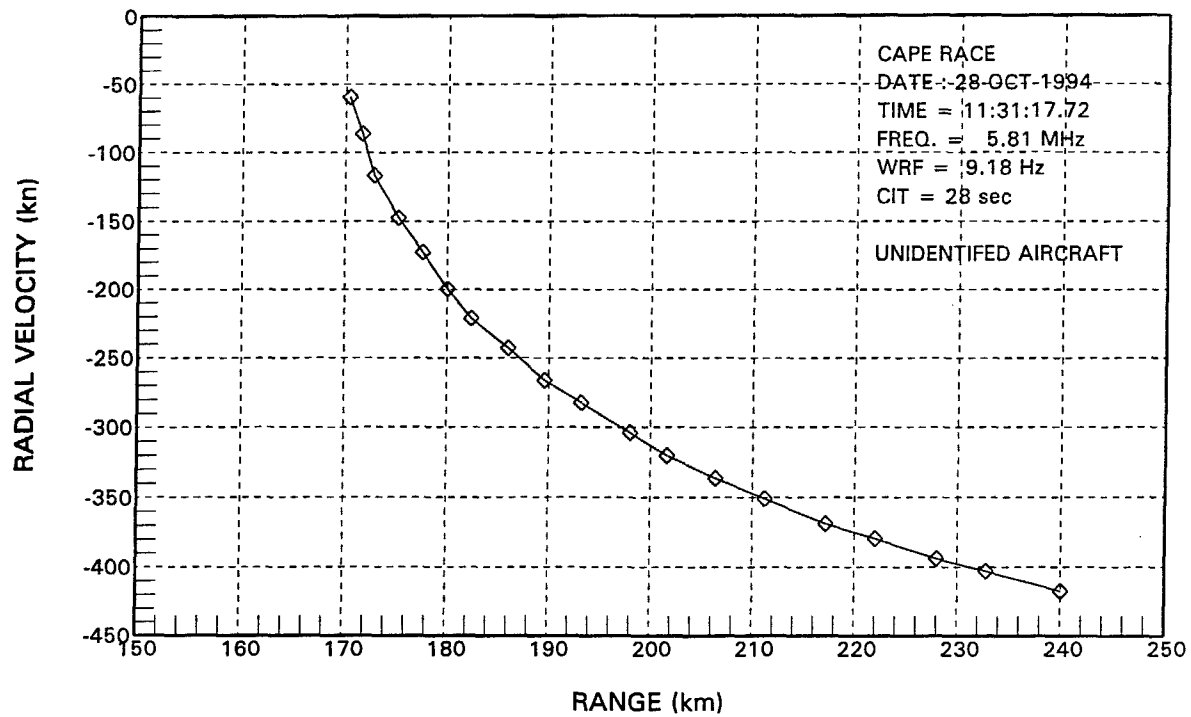


Figure 46. Radial velocity of an unidentified aircraft as a function of range.

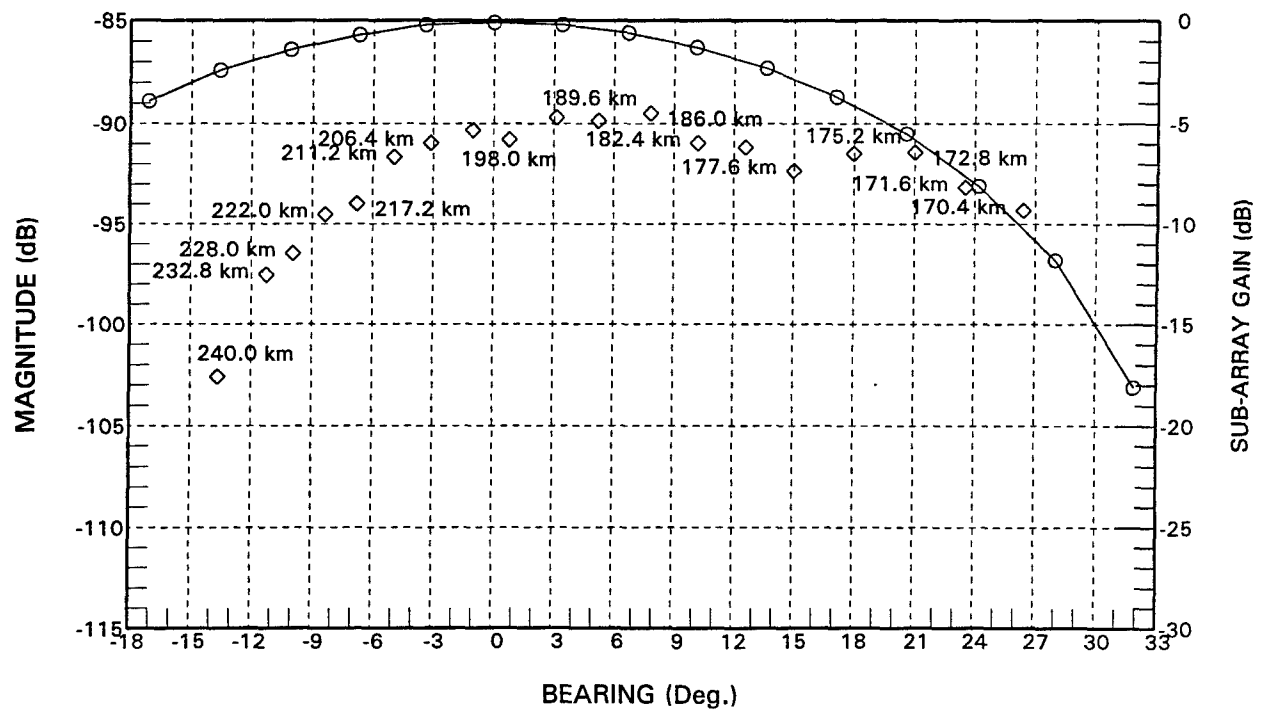


Figure 47. Target energy as a function of bearing for for an unidentified aircraft.



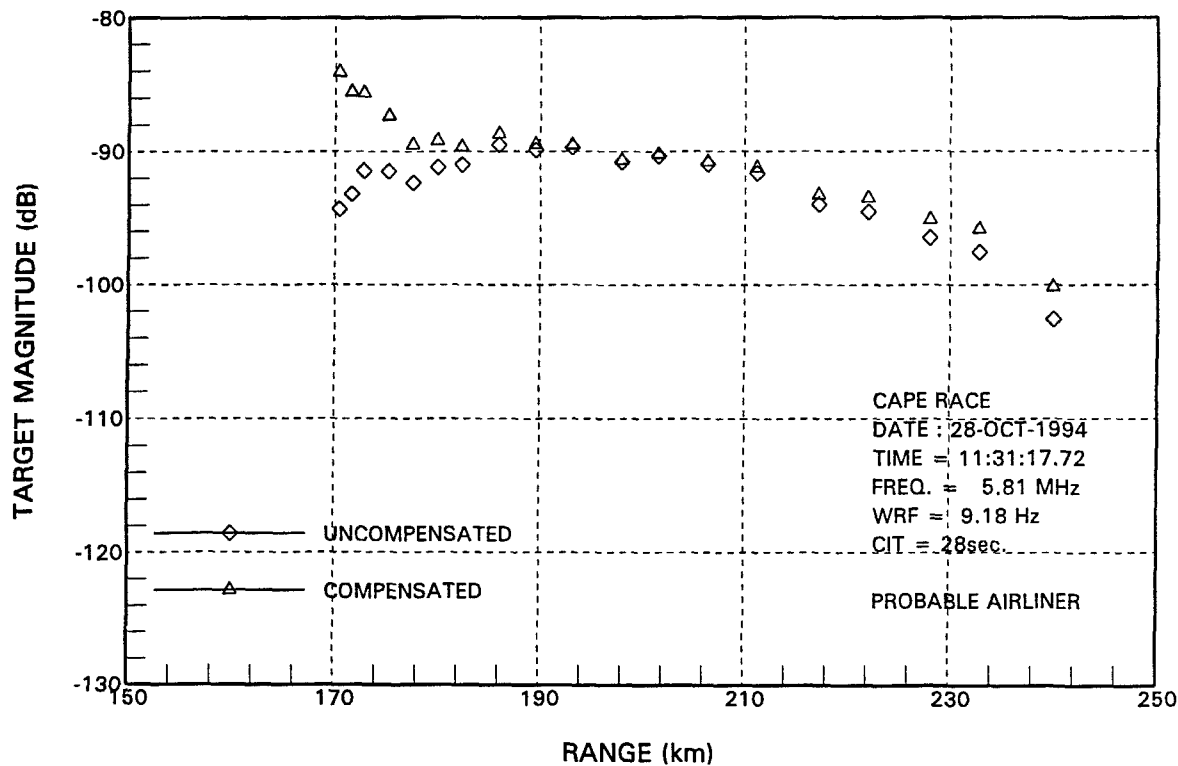


Figure 48. Target energy as a function of range for for a probable airliner.

Figure 50 plots the radial velocity of this aircraft as a function of range. It ranged from about -50 knots to over 375 knots. The aircraft's speed changed abruptly at the range of about 250 km. This change is due to a change in heading, as can be seen in Figure 49.

Figure 51 shows the resulting tracks obtained from data set AIR\_TEN. Three tracks are shown: (i) that of the controlled target King-Air 200, (ii) a commercial airliner and (iii) an unknown target. The unknown target will be examined in more detail in Section 4.4.2. The airliner was first detected at a range of 295.2 km and an azimuth of  $103.7^\circ$  true. The track was momentarily lost as the aircraft approached the first null of the receive array pattern at the range of 134.4 km and an azimuth of  $152.4^\circ$ . The aircraft was detected again as it crossed the antenna sidelobe. It can be seen that this aircraft followed a flight path that was very similar to that of data file AIR\_SEVEN (see Figure 49). Hence, it may be concluded that this aircraft and the one in Figure 49 were regularly scheduled airliners.

#### 4.4.2 Unknown target

In Figure 51, an unknown target was tracked from the range of 275 km at an azimuth of  $115.7^\circ$  true to 240 km at  $110.3^\circ$  true. The apparent speed of this target was relatively low. The track spanned approximately 42 km over a time interval of about 865 seconds. This translated into a speed of 48.6 m/sec or 94.4 knots. The fact that this target was detected and tracked at a relatively long distance suggests that its radar cross section must be fairly large. If it were an

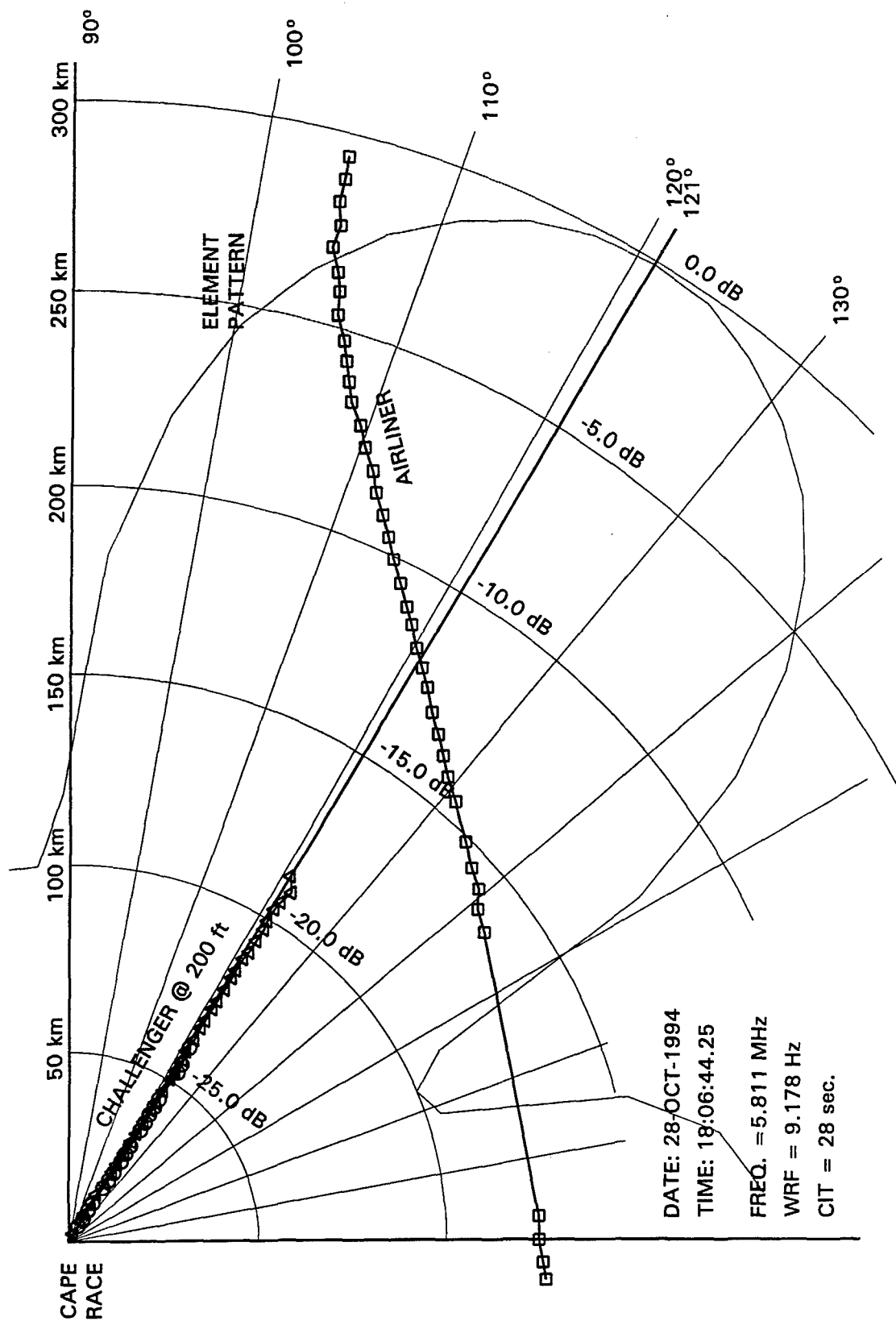


Figure 49. Accumulated tracks derived from data file AIR\_SEVEN.

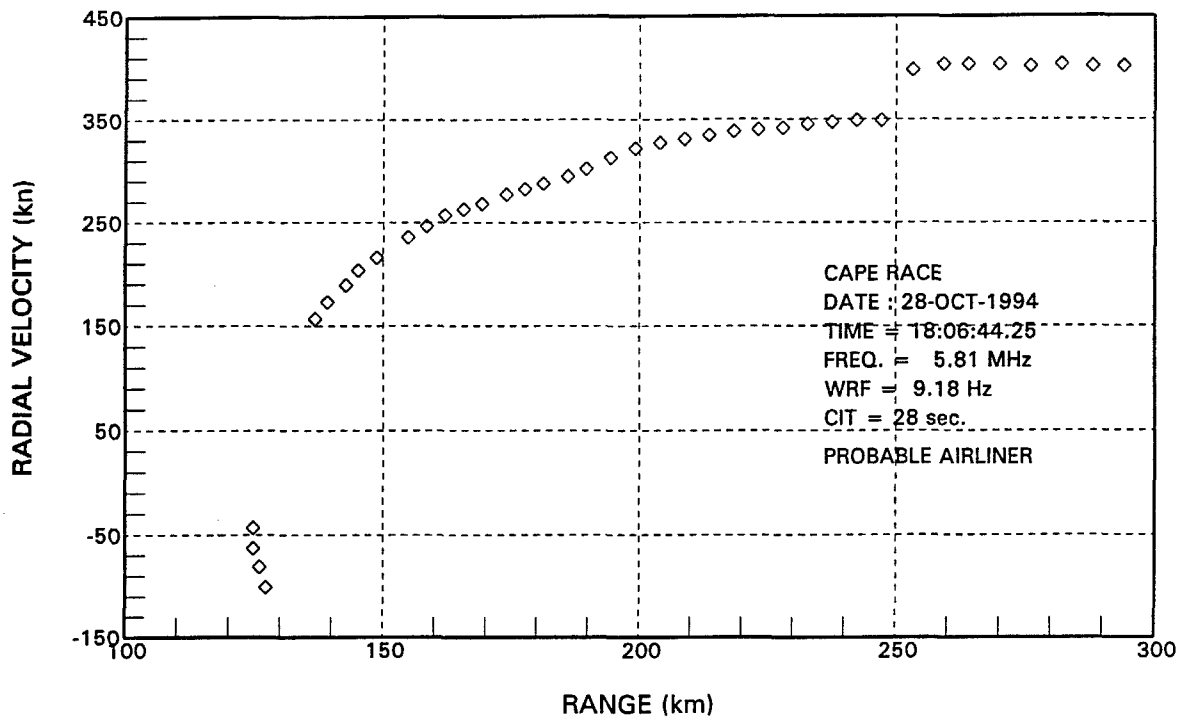


Figure 50. Radial velocity of an unidentified aircraft as a function of range.

airliner, its air speed should exceed several hundred knots. To investigate this unknown target further, the target magnitude is plotted against bearing in Figure 52. It can be seen that, over the time interval the target was tracked, the magnitude fluctuated over a range of 25 dB. Since the RCS for real targets such as aircraft do not vary significantly over a limited range and azimuth, it can be concluded that this was not a man-made target.

Figure 53 shows the waveforms of a number of contiguous range bins in order of decreasing range over a time interval of about 500 seconds. The unidentified target is seen to migrate into neighbouring range bins at a rate of approximately one range bin every 23 seconds.

One can only speculate about the origin of this target. One possible explanation is that the detection was the result of scattering from a small region of ionized gas. The apparent movement of the target could be the result of the ionized gas being driven by the wind. In any event, the characteristics of this target were sufficiently different from those for a man-made target in both Doppler and spatial domains so that special tracking algorithms may be designed to reject these detections.

#### 4.5 Estimation of target radar cross section

Theoretically, the radar cross section of a target may be estimated from the received echo power through the radar equation. However, because the radar data are in the form of digital samples, precise calibration is required to translate the numerical values into physical quantities,

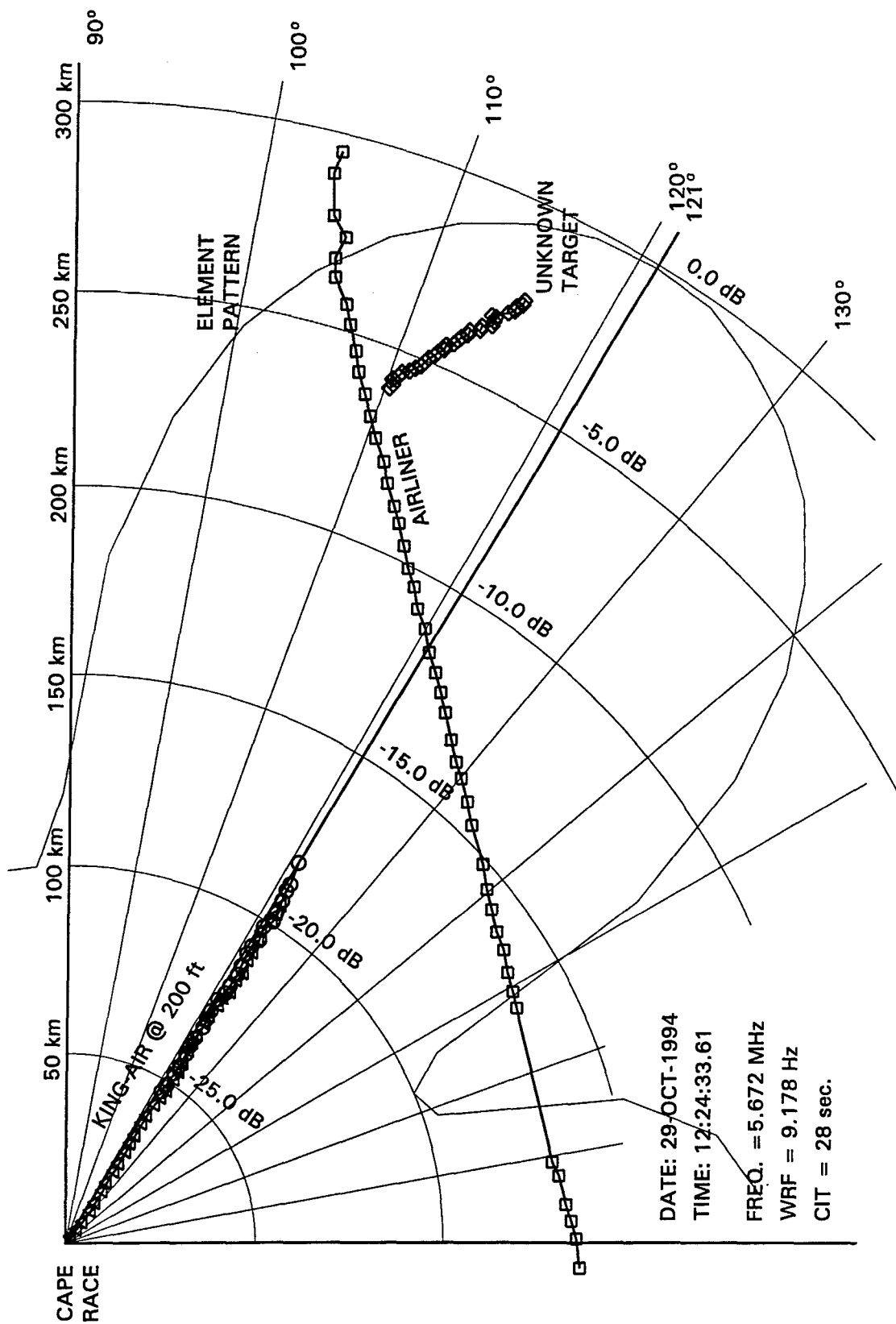


Figure 51. Accumulated tracks derived from data file AIR\_TEN.

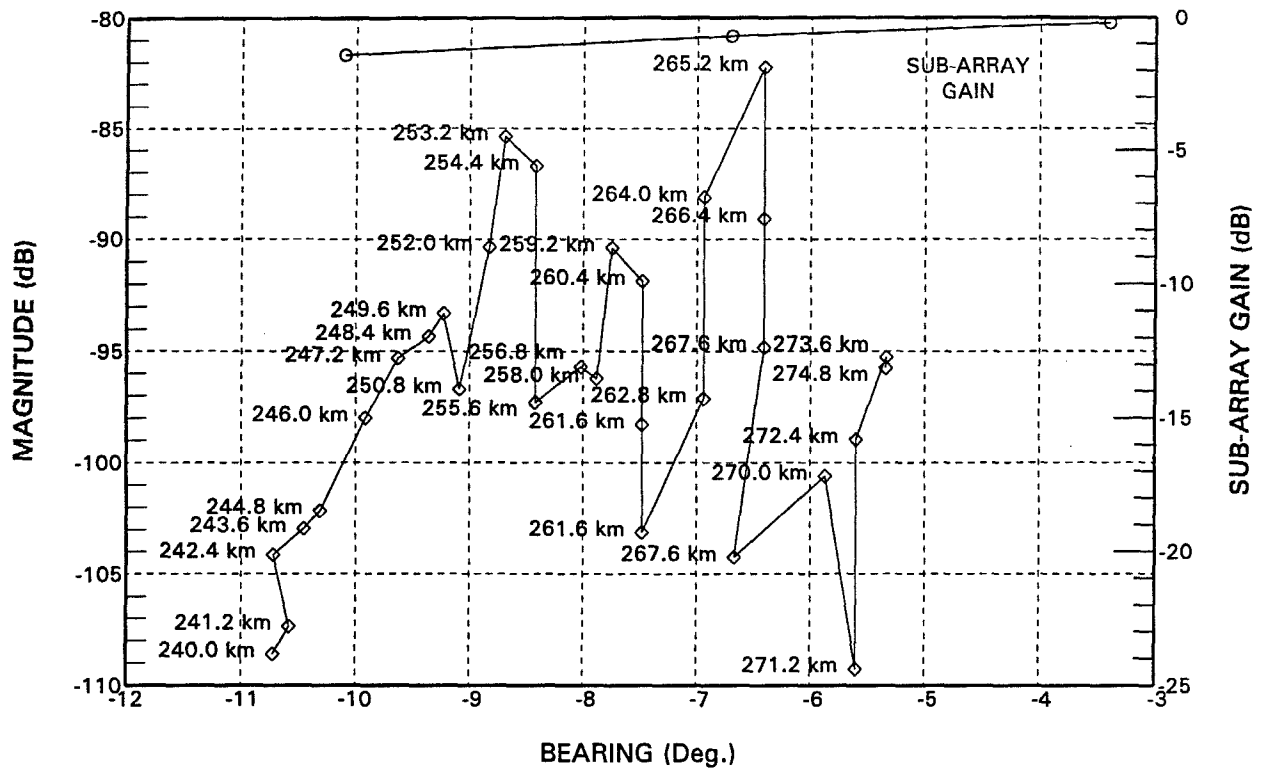


Figure 52. Echo energy as a function of bearing for an unidentified target.

such as the gains and losses of the radar components and sub-systems, from which the radar cross section can be estimated. This is generally a tedious process because of the frequency dependence of the parameter values of the electronics and antenna gains. The radar equation, however, can be used to obtain an estimate the RCS of a target from another target with a known RCS.

The HFSW radar equation given in the form of (12) may be interpreted as the signal-energy to noise-density ratio. Hence, the signal energy of a target with a known RCS,  $\sigma_1$ , is

$$E_1 = \frac{P_{av} G_t G_r \sigma_1 T_i 4\pi}{L_T^2 L_S \lambda^2} \quad (25)$$

Similarly, the signal energy of a target with an unknown RCS  $\sigma_2$  is given by

$$E_2 = \frac{P_{av} G_t G_r \sigma_2 T_i 4\pi}{L_T^2 L_S \lambda^2} \quad (26)$$

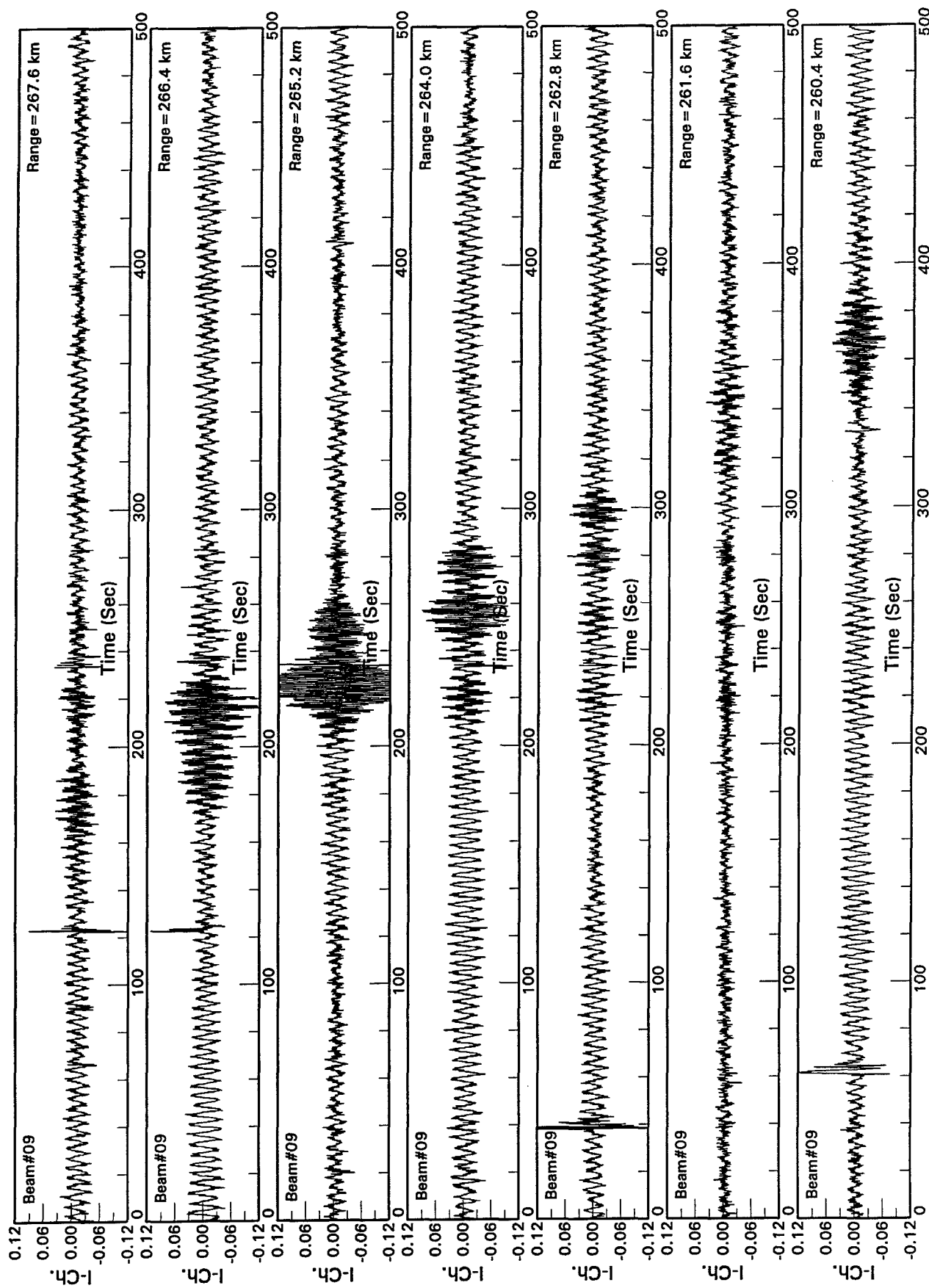


Figure 53. I-Channel waveforms for a number of range bins containing an unidentified target.

Consequently, the RCS of the unknown target may be obtained from another with a known RCS by taking the ratio between (26) and (25).

$$\sigma_2 = \sigma_1 \frac{E_2}{E_1} \quad (27)$$

Since coherent integration concentrates the target energy into the Doppler bin corresponding to the target's radial velocity (assuming a constant-velocity target),  $E_1$  and  $E_2$  may be obtained by summing the energies in a small number of Doppler bins around the respective Doppler bins for the two targets.

Several conditions must be satisfied for the estimate to be valid. The first is that the SNRs of both targets must be sufficiently high to minimize the effects of noise on the estimate. A value of 20 dB should be adequate. The second is that the altitude of both targets should be more than one wavelength above the sea surface to minimize the ground proximity effect. The third is that the sea state should be about the same to minimize the variation of the propagation loss due to the variation in sea state. And finally, the coherent integration time should be the same for both targets.

The RCS of the King-Air 200 has been calculated using the NEC program. At 5.81 MHz, the RCS of a King-Air in level flight was estimated to be about -1 dBm<sup>2</sup>. Figure 54 compares the target energies of the Challenger 601-A and the King-Air 200 as a function of range. Both curves were taken on the out-bound leg. That is, the radar was viewing the aircraft from the rear. It shows that, on the average, the energy of the echoes from the Challenger was about 5 dB higher than the King-Air. Hence, the RCS of the Challenger at level flight is estimated to be about +4 dBm<sup>2</sup> at 5.8 MHz.

Figure 55 compares the target energies of the King-Air and the T-33 as a function of range. The echo energy of the King-Air was about 12 dB higher than that of the T-33. An estimate of the RCS for the T-33 at 5.8 MHz would be about -13 dBm<sup>2</sup>.

The HFSW radar equation can also be used to provide some degree of verification to the RCS of a target estimated by other means. The dominant components of sea clutter at HF are the Bragg lines. The equivalent scattering coefficient ( $\sigma^0$ ) for a fully developed sea has been calculated by Barrick [24] to be -17 dBm<sup>2</sup>/m<sup>2</sup>. A value of -20 dBm<sup>2</sup>/m<sup>2</sup> is now [25] considered to be more appropriate. In subsequent results, the revised value of  $\sigma^0 = -20$  dBm<sup>2</sup>/m<sup>2</sup> was used.

A sea is considered fully developed for an HF radar operating at a given frequency if the gravity waves that give rise to the Bragg lines at that radar frequency reach steady state. The minimum speed of the wind that sustains the gravity waves for a given radar frequency  $f_c = c/\lambda$  is determined by

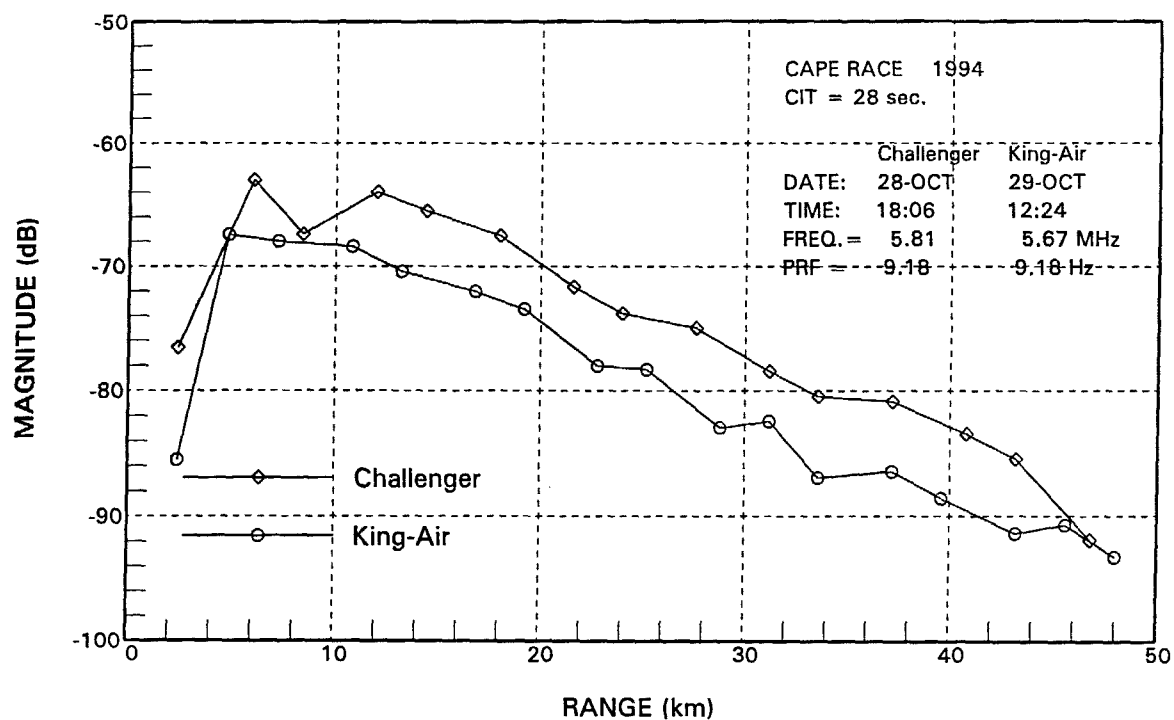


Figure 54. Comparison of the target energy between a King-Air and a Challenger.

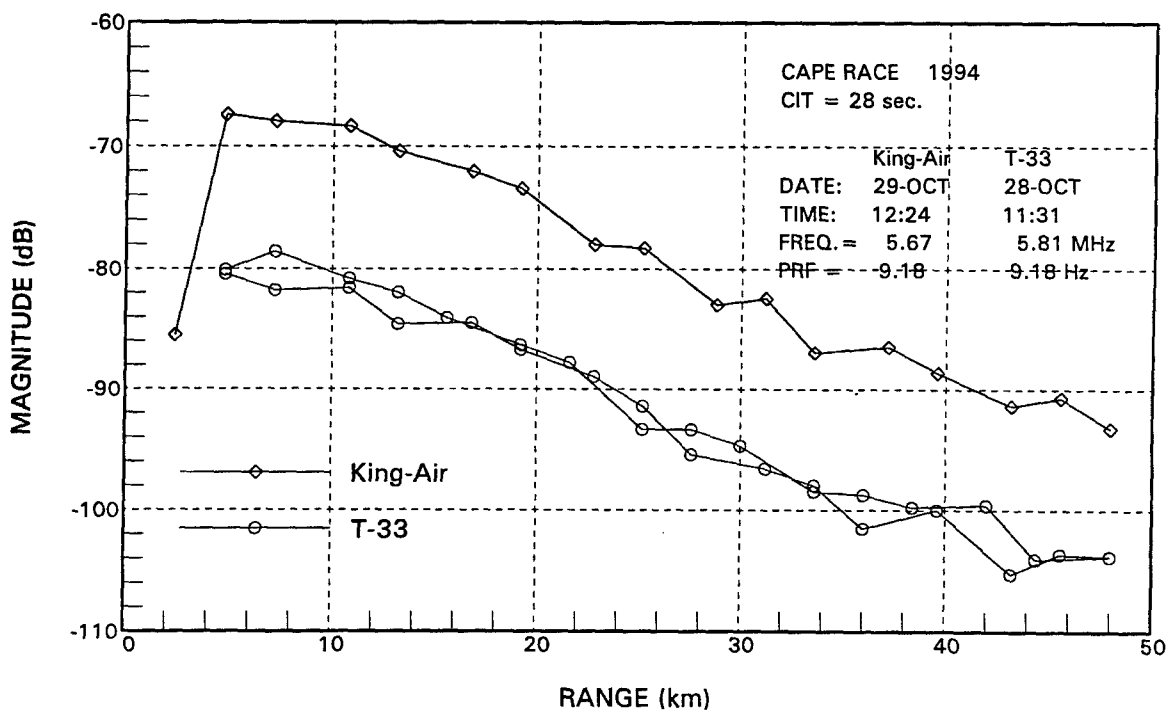


Figure 55. Comparison of the target energy between a King-Air and a T-33.



$$v = \pm \left[ \frac{g\lambda}{4\pi} \right]^{\frac{1}{2}} \quad (28)$$

The equivalent RCS of the Bragg components for the resolution cell is given by the product of the scattering coefficient and the resolution cell area:

$$\sigma = \sigma^0 A \quad (29)$$

and

$$A = R \frac{c\tau}{2} \theta \quad (30)$$

where  $R$  is the range,  $\tau$  is the pulse length and  $\theta$  is the antenna azimuthal beamwidth.

The validity of the above estimate is subjected to the following conditions. First, the energy in the Bragg lines fluctuates over time. Therefore the value of the Bragg energy should be averaged over a number of spectra to ensure that temporal fluctuation is minimized. Second, the sea must be fully developed in the area of interest. Finally, the SNR must be sufficiently high so as to minimize the effect of noise on the estimate.

The energies of the Bragg lines and the King-Air as a function of range are shown in Figure 56. The data for Bragg line and the target were from files AIR-4 and AIR-F4 in Table 5, respectively. The data from file AIR-4 was used for the Bragg lines because on 27 October, when the data in File AIR-F4 was taken, the wind speed was only about 5 knots, whereas the wind speed on 5 October was 15 knots, just high enough to ensure a fully developed sea at 4 MHz.

The experimental data were fitted to the theoretical attenuation of the sea clutter as a function of range as follows. The echo magnitude of a target with a given RCS decreases with range according to (10). For sea clutter, however, the equivalent RCS increases directly with range. Consequently, the sea-clutter magnitude attenuates with respect to range at a rate proportional to

$$\propto L_T^2(R) \frac{1}{R} \quad (31)$$

where  $R$  is the range and  $L_T$  is as defined in (10).

Hence, the sea-clutter magnitude at an arbitrary range  $R$  may be obtained from that at another range  $R_1$  by

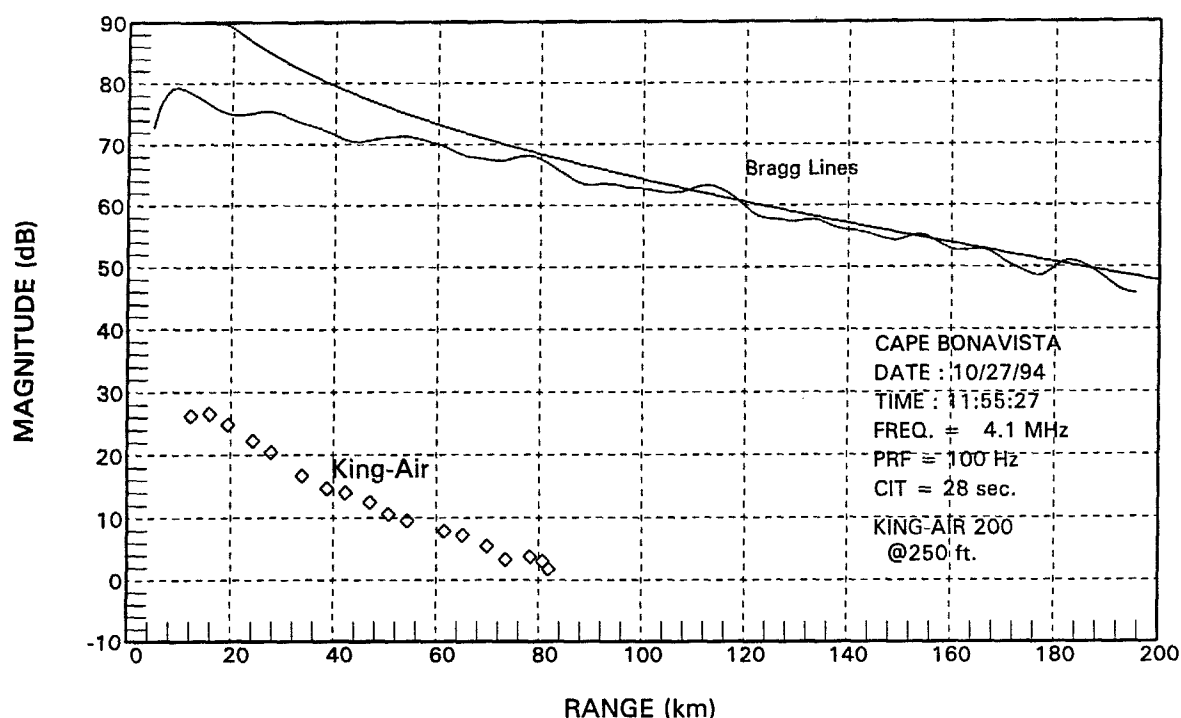


Figure 56. Comparison of Bragg energy with target energy of the King-Air at 4 MHz.

$$E = E_1 \frac{L_T^2(R_1)}{L_T^2(R)} \frac{R}{R_1} \quad (32)$$

The fitted results are superimposed in Figure 56. At a range of 80 km (a range that ensures the aircraft was below the radar horizon), the target energy was about 66 dB below the Bragg energy. The equivalent RCS of the Bragg line is computed from (29) to be 61.17 dBm<sup>2</sup>, assuming a range extent of 7.5 km, an azimuthal beamwidth of 12.5°. Hence, the RCS of the King-Air at 4.1 MHz would be approximately -4.83 dBm<sup>2</sup>.

Figure 57 compares the energies of the Bragg lines and the King-Air as a function of range at 5.81 MHz. The Bragg-line results were derived from files AIR-SEVEN (because the wind speed on 28 October was high enough to ensure a fully developed sea at 5.81 MHz), and the aircraft results were derived from file AIR\_TEN. The Bragg-energy data were fitted to the theoretical model and superimposed in the Figure 57. As can be seen, the experimental data follow the theoretical data very closely. At a range of 80 km, the target energy was about 48.6 dB below the Bragg energy. The equivalent RCS of the Bragg lines is computed from (29) to be 46.2 dBm<sup>2</sup>, assuming a range extent of 1.2 km and an azimuthal beamwidth of 2.5°. Hence, the RCS of the King-Air at 5.81 MHz would be approximately -2.4 dBm<sup>2</sup>.

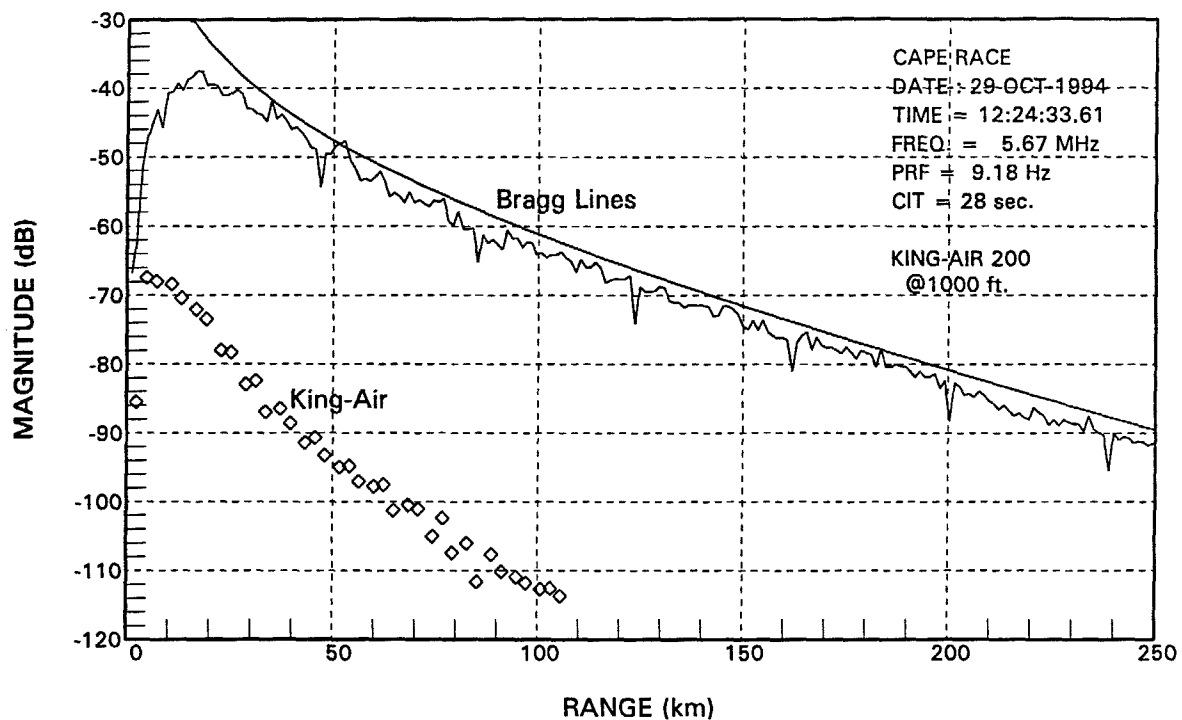


Figure 57. Comparison of Bragg energy with target energy of the King-Air at 5.8 MHz.

The energies of the Bragg lines and the King-Air at 15.77 MHz, as a function of range, are shown in Figure 58. The data for both Bragg-lines results and the aircraft results were derived from files AIR-16 because the wind speed on that day was sufficient to ensure a fully developed sea for 15.77 MHz. At a range of 36 km the target energy was about 60 dB below the Bragg-line energy. The equivalent RCS of the Bragg line is estimated from (29) to be  $57.7 \text{ dBm}^2$ , assuming a range extent of 7.5 km, an azimuthal beamwidth of  $12.5^\circ$ . Hence, the RCS of the King-Air at 16 MHz would be approximately  $-2.3 \text{ dB dBm}^2$ . However, if the signal loss of 16 dB due to the aircraft being  $25^\circ$  off boresight is taken into account, the RCS would be about  $13.7 \text{ dBm}^2$ .

Table 7 summarizes the RCS estimates of the King-Air at nominal frequencies of 4, 6 and 16 MHz and compares them with those obtained from NEC modelling. It can be seen that the estimates from the experimental data were within a few dB of the values estimated by the NEC software.

Table 7. Comparison of RCS estimates between NEC modelling and experiment.

Frequency	4 MHz	6 MHz	16 MHz
NEC estimate	-8 $\text{dBm}^2$	-1 $\text{dBm}^2$	10 $\text{dBm}^2$
Experiment	-4.83 $\text{dBm}^2$	-2.4 $\text{dBm}^2$	13.7 $\text{dBm}^2$
Difference	3.17 dB	-1.4 dB	3.7 dB

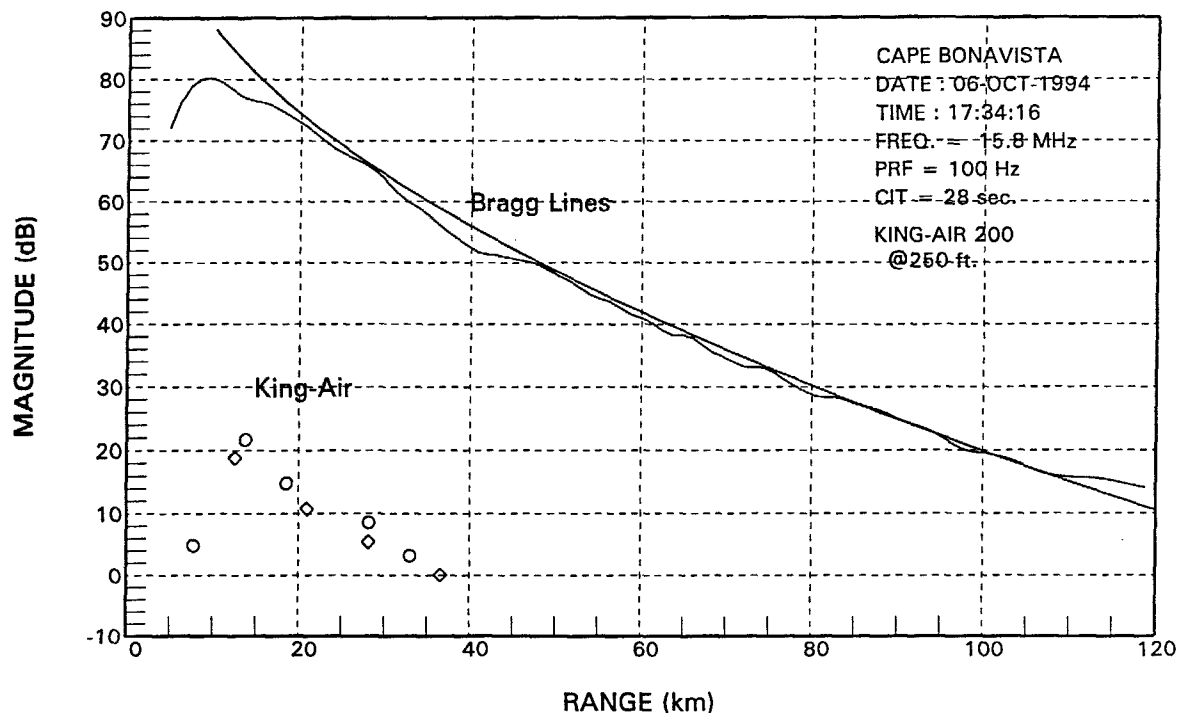


Figure 58. Comparison of Bragg energy with target energy of the King-Air at 15.8 MHz.

#### 4.6 Probable causes for the Cape Race radar's performance deficiency.

Because the radar at Cape Race had not been properly calibrated, the origin of the performance deficiency could not be determined precisely. There were both system and environmental factors that could have contributed to a degraded detection performance.

The first was that the cables connecting the receive antennas to the receivers all had equal lengths. The end element of the receive array was approximately 500 m from the receiver. This meant that there was a significant amount of cable-loss in each channel. From the Cape Bonavista data, it was estimated that the external noise level at mid-day there was lower than the CCIR-predicted median value. The Cape Race site should be at least as quiet as Cape Bonavista because it is more remote from any urban or rural centres. Consequently, it was possible that the system was receiver-noise limited.

The second factor was that the FMICW waveform used in the Cape Race radar requires a contiguous bandwidth of about 125 kHz. The probability of encountering some co-channel interference was therefore greater than with a more narrow-band waveform. From noise measurements taken at the site, it was observed that the frequency band where the Cape Race HFSWR was operating was rather congested.

A third factor was the sub-optimal implementation of the pulse-compression processing algorithm in the Cape Race radar. Northern Radar's engineer suggested that the ambiguous-range response observed in that radar was caused by the sub-optimal matched-filter processing. It could also have resulted in additional noise in the processed data.

Another possible contributing factor was that there could be some loss in the surface wave associated with the land path between the transmit antenna and the sea. The transmit antenna was situated approximately 200 metres from the shore. All of these could have contributed to the degradation in performance. Further investigation will be carried out to determine the precise causes.

## 5. CONCLUSIONS.

Detection and tracking trials of low-altitude aircraft using experimental HFSWR facilities in Newfoundland have been carried out. Two HFSWRs were employed in the trials. The Cape Bonavista HFSWR was a relatively low-power and low-resolution radar, while the Cape Race HFSWR was a relatively high-power and high-resolution radar. A number of experiments designed to assess different aspects of the aircraft-detection performance of the HFSWR was performed and the data analyzed. These include (i) detection range, (ii) tracking of low-altitude manoeuvring aircraft, (iii) variation of radar cross section with range and (iv) the degree of agreement between theoretical and experimental results.

Results obtained from the Cape Bonavista radar indicated that the experimental performance of the radar was very close to the theoretical prediction. The experimental data indicated the noise level at mid-day at Cape Bonavista was probably lower than the CCIR-predicted median value. Hence, Cape Bonavista may be classified as a very quiet rural site. With an average power of about 25 watts (at 4 MHz), an aircraft such as the King-Air 200 can be detected and tracked out to 80 km during day-light hours. At 6.9 MHz, with a slightly higher average power of 40 watts, the King-Air was tracked to beyond 90 km. At about 16 MHz, where the RCS of the King-Air is near a local maximum, the aircraft was tracked to about 36 km. However, the received echo was not at full strength because the aircraft's bearing was off the mainbeam. If the aircraft was flying along the boresight of the receive antenna, it was expected that the detection range would be around 47 km.

Results obtained from the Cape Race radar indicated that the performance of that radar had not matched the theoretical prediction. With the radar operating at a nominal frequency of 5.8 MHz and with an average power of about 600 watts, an aircraft such as the King-Air 200 flying at an altitude of 200 ft was detected and tracked to a maximum of 120 km. A slightly larger aircraft, the Challenger 601-3A was also tracked to about the same distance, although at a slightly higher noise level. Probable causes for this performance deficiency was discussed in Section 4.6.

The ability of the HFSWR to track low-altitude manoeuvring aircraft was demonstrated. A King-Air 200 flying at 200 ft in a figure-eight pattern centred at 40 km was detected and tracked throughout the course. Only a few detections were missed because of the target Doppler being too close to the sea-clutter dominated region. The ability of the HFSWR to track high-altitude aircraft at very long range was also demonstrated by detecting and tracking commercial airliners out to ranges beyond 275 km.

The magnitude of the target echo is a useful parameter that can be exploited to distinguish a man-made target from echoes from ionospheric discontinuities and meteor trails. For this type of ionospheric reflection, the magnitude of the echoes fluctuates over a wide range over a short distance, whereas the magnitude of the echo from an aircraft remain fairly steady.

The RCS of aircraft in the HF region depend to a large extent the vertical dimension of the aircraft. During banking manoeuvres, the RCS of an aircraft could increase up to 20 dB from that observed by the radar with the aircraft at level flight.

The determination of the optimum operating frequency for an HFSWR against low-altitude aircraft requires a trade-off among three parameters: propagation loss, RCS and the background noise level. For Cape Bonavista, the results indicate that the performance at frequencies of 4 and 7 MHz was very similar; however, at a higher frequency of 16 MHz, the detection performance was significantly poorer. This suggests that it is more advantageous to select a frequency that minimize the propagation loss while attaining a reasonable value of the RCS than to select one that maximizes the RCS without regard to propagation loss.

The performance of HFSWR at night time would be degraded because of the generally increased noise level. According to CCIR data, the noise level at the Canadian east coast is 15 to 20 dB higher at night time compared with the level at mid day. Theoretically, the night-time performance can be estimated from the models. In reality, however, the night time noise level is much higher than CCIR predicted. The reason is that the radar does not discriminate between noise and interference, and much of the increased noise level is actually interference. Since interference has certain characteristics that can be exploited for its suppression, a meaningful evaluation of the night time performance of HFSWR should be carried out with the interference-suppression techniques incorporated. This will be subject of the next phase of the work.

## 6. REFERENCES.

- [1] Ponsford, A.M., "HFSWR trial for aircraft detection and interference suppression," Contract Report for DSS No. W7714-5-9883/01 SV, Raytheon Canada Report ASD-270 May 1996.
- [2] Leong, W.H., "An analysis of the experimental data measured with the modified HF surface-wave radar at Cape Bonavista," DREO Report No.1312, Defence Research Establishment Ottawa, July 1997.
- [3] Ponsford, A.M., "The study of interference suppression for surface-wave radar," Contract Report for DSS No. W7714-4-9805/01 SV, March 1995.
- [4] Ponsford, A.M. and S.K. Srivastava, "Ground-wave radar development at Nordco Limited: Phase 1," Contract Report 095-89G, Nordco Limited, January, 1991.
- [5] Ponsford, A.M., "Design and development of a prototype instrumentation for HF surface-wave radar application," Contract Report for DSS No.W7714-0-9446/01-ST, Raytheon Canada Report ASD-148, 1991.
- [6] Chan, H.C., "Evaluation of the FMICW waveform in HF surface-wave radar applications," DREO Report No.1219, Defence Research Establishment Ottawa, January 1994.
- [7] Lipa, B.J. and D.E. Barrick, "Analysis Methods for Narrow-beam High Frequency Radar Sea Echo," NOAA Tech. Report ERL 420-WPL 56, 1982.
- [8] Shearman, E.D.R., "Radio science and oceanography," Radio Science, Vol.18, No.3, May-June, 1983, pp.299-230.
- [9] Madden, J.M., "The adaptive suppression of interference in HF ground-wave radar," Int. Radar Conf. 1987, pp.98-102.
- [10] Compton, R.T., "Adaptive antennas - Concepts and Performance," Prentice Hall, Englewood Cliffs, New Jersey, 1988.
- [11] Applebaum, S.P., "Adaptive arrays," IEEE Trans. on Antenna and Propagation, AP-24, No.5, September 1976, p 585.
- [12] Lucas, D.L. and D.J. Harper, "A numerical representation of CCIR report 322 high frequency (3-30 MC/S) atmospheric radio noise data," National Bureau of Standards, Technical Note No. 318, U.S. Department of Commerce, Boulder, Co, p.95.)
- [13] Spaulding, A.D. and J.S. Washbu, "Atmospheric radio noise: Worldwide levels and other characteristics," National Telecommunications and Information Administration Report No. 85-173, 1985, pp 192.



- [14] Norton, K.A., "The calculation of ground-wave field intensity over a finitely conducting spherical earth," Proceedings of the I.R.E., 1941, pp.623-639.
- [15] Skolnik, M.L., Ed., "Radar Handbook - Array Antennas," McGraw-Hill Book Company, New York, 1970, p.11-10.
- [16] Barrick D.E., "Theory of HF and VHF propagation across a rough sea," Radio Science Vol. 6, No.5, May 1971, pp.517-533.
- [17] Shearman, E.D.R., "Propagation and scattering in MF/HF ground wave radar," IEE Proceedings, Vol. 130, Part F, No.7, December 1983, pp.579-590.
- [18] Milson, J.D., "HF ground-wave radar equation." Proc. IEE Radar'97, Scotland, October, 1997, pp.285-290.
- [19] Rotheram, S., "Ground-wave propagation, Part 2: theory for medium and long distances and reference propagation curves," IEE Proc. Vol.128, pt F, No.5, October 1981, pp.285-295.
- [20] Friend, D., "The HF radar look-up table program user's manual - Version 3.0," Contract Report for DSS No.W7714-0-9898, Atlantis Scientific Systems Inc., March 1995.
- [21] Cantrell, B.H., "Adaptive tracking algorithm for tracking air targets with search radars," NRL Report 7805, Naval Research Laboratory, Washington, DC, September, 1974.
- [22] Singer, R.A., R.G. Sea and K.B. Housewright, "Derivation and evaluation of improved tracking filters for use in dense multi-target environments," IEEE Trans. on IT, Vol.IT-20, No.4, July, 1974, pp.423-432.
- [23] Trueman, C.W. and S.J. Kubina, "HF ground wave radar studies," Contract Report for DSS No.W7714-3-9707/01-SV, Concordia University, August, 1994.
- [24] Barrick, D.E., "Remote sensing of sea state by radar, Ch.12 in Remote sensing of the Troposphere, V.E. Derr, Ed.," NOAA Environmental Research Laboratories, Boulder, Colo., 1972.
- [25] Howell, R.K. and D.E. Barrick, "A note on the Barrick sea-clutter cross section," IEEE Journal of Antennas and Propagation, 1997.

## 7. ACKNOWLEDGEMENT.

The author wishes to thank the personnel of Raytheon Canada Limited and Northern radars for carrying out the experiments on behalf of DND. In particular, thanks are due to Dr. A.M. Ponsford of Raytheon Canada and Mr. B. Dawe of Northern Radars. This work was supported by the Canadian Department of National Defence.

## 8. APPENDICES.

### Appendix A. NEC modelling of the RCS of the Beechcraft King-Air 200.

The RCS of the King-Air 200 aircraft has been calculated using the Numerical Electromagnetic Codes (NEC) program. The figures in this appendix was extracted from reference [20] of which the work was done under a contract to DND. Figure A.1 compares the theoretical RCS of the Beechcraft King-Air-200 at level flight between the cases of nose-on and broad-side incidence. Figure A2. compares the RCS at nose-on incidence between the case of level flight and the case with the aircraft pitched 10° nose down. Figure A.3 compares the theoretical RCS of the King-Air between the cases of nose-on and broad-side incidence with the aircraft rolled 45 °.

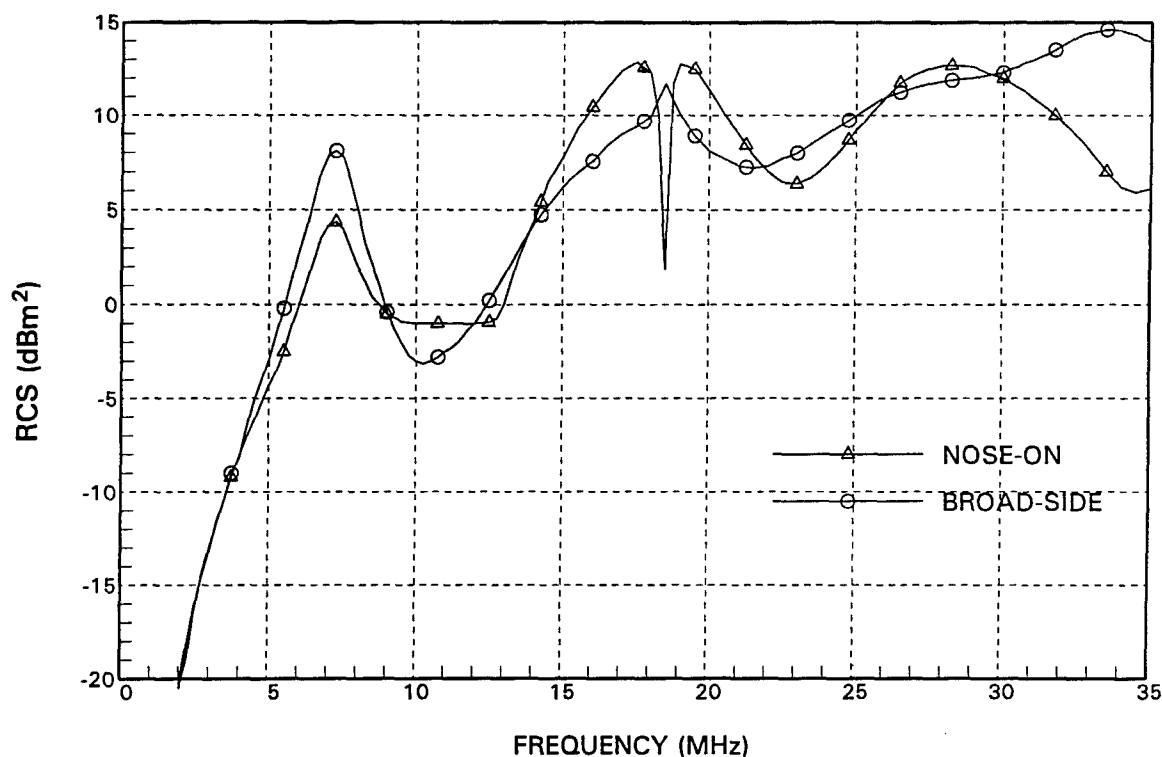


Figure A1. NEC RCS estimates for a King-Air 200 at level flight.

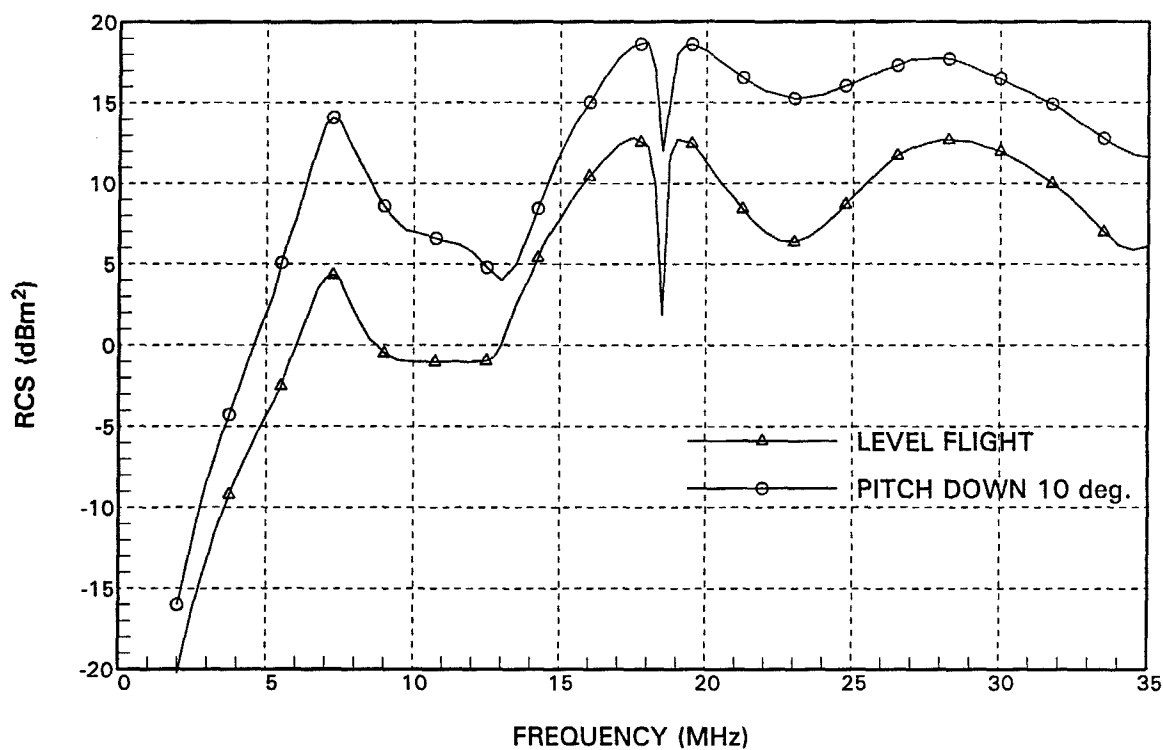


Figure A2. NEC RCS estimates of a King-Air at nose-on incidence.

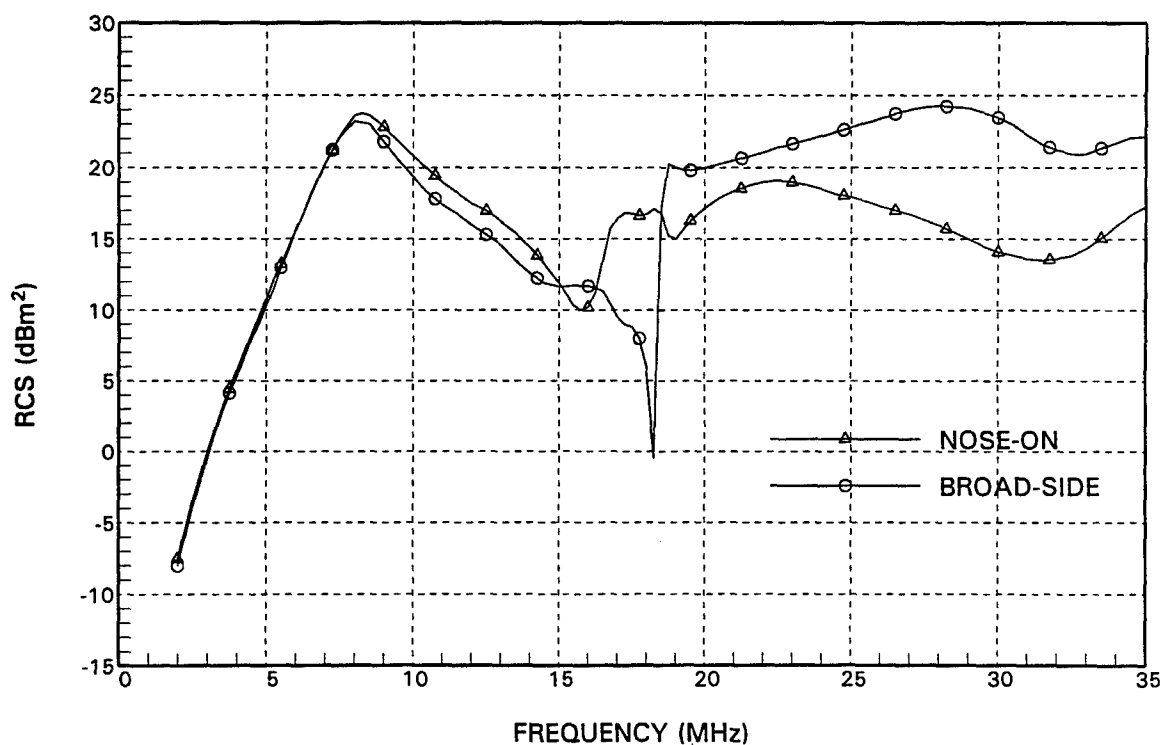


Figure A3. NEC RCS estimates for a King-Air 200 rolled 45° to port.

## Appendix B. Cape Bonavista Radar Log

Radar Log     King-Air Trials: Note following trials it was discovered that the aircraft was flying 110° magnetic and not True.

5 October, 1994     4.1 MHz, 240 seconds, 100 Hz PRF, BP2 LP1 RS85 offset 160 range samples: 8 element array summed, single channel data.

### Tape

2	AIR4-T1	Test data
2	NO4-T1	Transmitter off, Noise data
2	TE4-T1	50Ω termination at input to pre-amp filter
2	AIR4-T2	Test data
3	AIR4-1	1004 Aircraft trial commence
3	AIR4-2	1008
3	AIR4-3	1013 Aircraft on station 75 n.mi @ boresight, @150 ft (aircraft actually at 110° magnetic.
3	AIR4-4	1017
3	AIR4-5	1021
3	AIR4-6	1025
3	AIR4-7	1030
3	AIR4-8	1034
3	AIR4-9	1038 Aircraft overhead radar station @ 1041 inward and 1044 outward.
3	AIR4-10	1042
3	AIR4-11	1046
3	AIR4-12	1051
3	AIR4-13	1055
3	AIR4-14	1059
3	AIR4-15	1103

---

Radar Log     King-Air Trials: Note following trials it was discovered that the aircraft was flying 110° magnetic and not True.

5 October, 1994     7 MHz, 240 seconds, 100 Hz PRF, BP2 LP1 RS85 offset 160 range samples: 8 element array summed, single channel data. Filter plus preamp and 8 dB attenuation

### Tape

4	AIR7-1	1131 Trials start King-Air inbound from 75 n.mi. LP2 BP2.
4	AIR7-2	1136 LP1 BP2
4	AIR7-3	1140
4	AIR7-4	1144
4	AIR7-5	1149
4	AIR7-6	1153 1155 Aircraft overhead
4	AIR7-7	1158 1157 Aircraft outbound
4	AIR7-8	1202
4	AIR7-9	1206
4	NO7-1	

# Radar Log    Noise data Trials

5 October, 1994      4 MHz, 200 seconds, 50 Hz PRF, BP2 LP1 RS85 offset 160 range samples: 4 MHz filter plus preamps

## Tape

	TEST-1 to TEST-6	Aborted
5	TEST-7      1615	ANT5 (Valcom Doublet) split into four and sent to four receivers via filters and preamplifiers. Calibration Tone at 4.1 MHz Plus 10 Hz.
5	TEST-8      1619	As TEST-7
5	TEST-9      1628	As TEST-7
5	TEST-10     1638	ANT3 to RX1, ANT4 to RX2, ANT5 to RX3, ANT6 to RX4
5	TEST-11     1644	ANT1 to RX1, ANT3 to RX2, ANT5 to RX4, ANT7 to RX4
5	TEST-12     1651	As TEST-11
5	TEST-13     1656	As TEST-10
5	TEST-14     1719	Dipole RX1, ANT4 RX2, ANT5 RX3, ANT6 RX4.
5	TEST-15	As TEST-14
5	TEST-16	As TEST-14
5	TEST-17	as TEST-14, but digital filters bypassed, 85 offset.
5	TEST-18	As TEST-17
5	TEST-19	As TEST-17, but 5 offset 100 samples.
5	TEST-20	as TEST-19
5	TEST-21	As ANT3 to RX1, ANT4 to RX2, ANT5 to RX3, ANT6 to RX4.
5	TEST-22	ANT1 to RX1, ANT3 to RX2, ANT5 to RX3, ANT7 to RX4.
5	TEST-23	53 ft monitor (+2dB atten) RX1, Doublet 3 RX2, Quadlet (plus 3 dB) RX3, Jim Lundy's doublets RX4, LP1 BP2 85 offset 100 samples.
5	TEST-24	As TEST-23 but 185 samples offset
5	TEST-25	MUX data (MUX unit repaired and tested OK). ANT1 - RX1, ANT2 - RX2, ANT3 - RX3, ANT4 - RX4, with CAL. tone. ANT5 - RX1, ANT6 - RX2, ANT7 - RX3, ANT8 - RX4; 85 offset 100 samples.
5	TEST-26	As above
5	TEST-27	As above but 185 offset

6 October, 1994

6 MHz, 240 seconds, 100 Hz PRF, BP2 LP1 RS85 offset 160 range samples: 8 element array summed, single channel data, filter plus 10 dB preamp and 3 dB attenuation

Aircraft overhead at 1844

AIR6-1	1845	6.7 MHz
AIR6-2	1850	

AIR6-3	1854	LP2 BP2
AIR6-4	1858	
AIR6-5	1902	
AIR6-6	1906	LP2 BP2
AIR6-7	1911	LP2 BP2
AIR6-8	1915	LP1 BP2
AIR6-9	1919	1920:30 Aircraft overhead
NO6-1		

27 October 1994      King-Air Trials

200 seconds, 100 Hz PRF, BP2 LP1 RS85 offset, 160 range samples: filters plus preamps. Summed array on receive. PDOS clock 45 seconds ahead of logged times.

#### Tape

No. 1            F4.2    12:00:40

4 MHz log periodic. Aircraft overhead at 11:58:10, at 1214 aircraft was on station "A", return leg starts, overhead 12:33. Altitude 1000 ft.

No. 2            F6.2    12:45:40

Aircraft overhead at 12:44, Overhead inbound F6.9, altitude 1000 ft @ 13:17:00. Overhead outbound @ 13:25:00 F6.11 - altitude 250 ft. 13:42:30 on station "A" - note lost GPS on outbound, restored by end of flight - inbound OK. Overhead inbound @ 14:00.

### Appendix C: Cape Race experimental data log.

Time	Comments
Wednesday, 26 October, 1994	
Notes: Started first aircraft run with King Air. Communicated with aircraft "Speed Air 977" on Marine Channel 71. Radar TX frequency = 5.811 MHz.	
12:19	Start first run @ 1000 ft altitude
12:38	End outward leg
13:15	Passed over Cape Race @ 2000 ft (B) altitude
13:18	@ 500 ft altitude, 5 mi range from Cape Race; outward bound second run
14:01	finished second run data collection

Time (GMT)	Comments
Thursday, 27 October, 1994	
Notes: Experiment with King Air.	
10:10	Communicated with Atlantic Airways; King Air ready to take off at approx. 10:25
	Trial with T-33 was rescheduled for Friday due to poor weather.
11:09	King Air passed over Cape Race @ 200 ft level; Wind at 10 kn ENE.
11:54	Completed first run with King Air at 200' altitude
11:57	Started second run with King Air at 200' altitude; speed 200 kn.
12:42	Completed second run; inbound leg was at 500 ft altitude.
12:50	Started backup of data to disk.

Time (GMT)	Comments
Friday 27 October, 1994	
Notes: T-33 Trainer; Length = 40 ft; wingspan = 41 ft. Flight plan: Outbound 10 min.; turn and inbound to Cape Race 10 min.; then outbound 20 to 25 min; execute zig zag and banking; Time in last outbound leg may be limited by fuel.	
11:31	Start trial with T-33 Trainer.
11:52	Started second outbound leg.
12:06	End of T-33 trail; Stopped data collection and started downloading to disk.
18:06	First run outbound at boresight of radar (121°) from true north; speed @ 200 knots; altitude @ 200 ft; inbound leg: same speed and altitude.
18:52	End of first run.
18:55	Started second run: heading 121° true; Speed: 200 knots; Altitude: 500 ft.
19:39	Completed second run; Winds at Cape Race approx. 20-25 knots NW.

Time (GMT)	Comments
Saturday 29 October, 1994	
Notes: Changed transmit frequency to 5.672 MHz due to strong interference near 5.811 MHz; Aircraft: King Air.	
11:51	Start figure-eight centred at 40 km; Altitude: 200 ft.
12:02	Completed first figure eight.
12:03	Started second figure eight at 500 ft. altitude.
12:13	Completed second figure eight.
12:21	Passed over Cape Race before turning around.
12:24	Started data collection for outbound leg to > 160 km;
12:52	Aircraft turned inbound as reported by Atlantic Airlines dispatcher.
13:15	Completed data collection; Aircraft broke off to return to St. John's at 21 nm.



**DOCUMENT CONTROL DATA**

(Security classification of title, body of abstract and indexing annotation must be entered when the overall document is classified)

1. **ORIGINATOR** (the name and address of the organization preparing the document. Organizations for whom the document was prepared, e.g. Establishment sponsoring a contractor's report, or tasking agency, are entered in section 8.)

DEFENCE RESEARCH ESTABLISHMENT OTTAWA

2. **SECURITY CLASSIFICATION**  
(overall security classification of the document including special warning terms if applicable)

UNCLASSIFIED

3. **TITLE** (the complete document title as indicated on the title page. Its classification should be indicated by the appropriate abbreviation (S,C or U) in parentheses after the title.)

DETECTION AND TRACKING OF LOW-ALTITUDE AIRCRAFT USING HF SURFACE WAVE RADAR (U)

4. **AUTHORS** (Last name, first name, middle initial)

CHAN, HING C.

5. **DATE OF PUBLICATION** (month and year of publication of document)

DECEMBER 1998

- 6a. **NO. OF PAGES** (total containing information. Include Annexes, Appendices, etc.)

92

- 6b. **NO. OF REFS** (total cited in document)

25

7. **DESCRIPTIVE NOTES** (the category of the document, e.g. technical report, technical note or memorandum. If appropriate, enter the type of report, e.g. interim, progress, summary, annual, or final. Give the inclusive dates when a specific reporting period is covered.)

DREO TECHNICAL REPORT

8. **SPONSORING ACTIVITY** (the name of the department project office or laboratory sponsoring the research and development. Include the address.)

Defence Research Establishment Ottawa  
3701 Carling Avenue  
Ottawa, Ontario, K1A 0Z4

- 9a. **PROJECT OR GRANT NO.** (if appropriate, the applicable research and development project or grant number under which the document was written. Please specify whether project or grant)

05AB11

- 9b. **CONTRACT NO.** (if appropriate, the applicable number under which the document was written)

- 10a. **ORIGINATOR'S DOCUMENT NUMBER** (the official document number by which the document is identified by the originating activity. This number must be unique to this document.)

DREO REPORT 1334

- 10b. **OTHER DOCUMENT NOS.** (Any other numbers which may be assigned this document either by the originator or by the sponsor.)

11. **DOCUMENT AVAILABILITY** (any limitations on further dissemination of the document, other than those imposed by security classification)

- (X) Unlimited distribution  
( ) Distribution limited to defence departments and defence contractors; further distribution only as approved  
( ) Distribution limited to defence departments and Canadian defence contractors; further distribution only as approved  
( ) Distribution limited to government departments and agencies; further distribution only as approved  
( ) Distribution limited to defence departments; further distribution only as approved  
( ) Other (please specify):

12. **DOCUMENT ANNOUNCEMENT** (any limitation to the bibliographic announcement of this document. This will normally correspond to the Document Availability (11). However, where further distribution (beyond the audience specified in 11) is possible, a wider announcement audience may be selected.)

UNLIMITED

UNCLASSIFIED

SECURITY CLASSIFICATION OF FORM  
(highest classification of Title, Abstract, Keywords)

13. ABSTRACT ( a brief and factual summary of the document. It may also appear elsewhere in the body of the document itself. It is highly desirable that the abstract of classified documents be unclassified. Each paragraph of the abstract shall begin with an indication of the security classification of the information in the paragraph (unless the document itself is unclassified) represented as (S), (C), or (U). It is not necessary to include here abstracts in both official languages unless the text is bilingual.)

A series of aircraft-detection trials was conducted using experimental high frequency surface wave radar (HFSWR) facilities located on the east coast of Canada. These trials were part of a research and development project undertaken by DND to demonstrate the HFSWR technology in a wide-area coastal surveillance role. Several aircraft were used in these trials, including a Beechcraft King-Air 200, a Lockheed T-33 and a Canadair Challenger 601 aircraft. Experimental results were in excellent agreement with theoretical predictions. With relatively low averaged power, the King-Air and the Challenger were tracked to beyond 120 km. The ability of the HFSWR to track manoeuvring targets was demonstrated. In addition the radar was shown to be capable of long-range tracking of high-altitude aircraft. Signal processing algorithms for the HFSWR can be improved by exploiting the characteristics of the signal environment measured in these trials.

14. KEYWORDS, DESCRIPTORS or IDENTIFIERS (technically meaningful terms or short phrases that characterize a document and could be helpful in cataloguing the document. They should be selected so that no security classification is required. Identifiers, such as equipment model designation, trade name, military project code name, geographic location may also be included. If possible keywords should be selected from a published thesaurus, e.g. Thesaurus of Engineering and Scientific Terms (TEST) and that thesaurus-identified. If it is not possible to select indexing terms which are unclassified, the classification of each should be indicated as with the title.)

RADAR  
HIGH FREQUENCY  
HF  
AIRCRAFT  
TRACKING  
DETECTION  
SURFACE WAVE  
OVER-THE-HORIZON  
OTH RADARS  
SURVEILLANCE  
MANOEUVRING  
IONOSPHERE  
INTERFERENCE  
NOISE

UNCLASSIFIED

SECURITY CLASSIFICATION OF FORM